Università degli Studi di Ferrara

DOTTORATO DI RICERCA IN
"SCIENZE DELL'INGEGNERIA"

CICLO XXVIII

COORDINATORE Prof. Stefano Trillo

Functional characterization of thermally activated shape memory alloys for innovative adaptive structures

Settore Scientifico Disciplinare ING-IND/21

Dottorando
Dott. Fortini Annalisa

Tutore
Ing. Merlin Mattia

Anni 2013/2015

There is only one way to learn. It's through action.
Everything you need to know you have learned through your journey.

(Paolo Coelho)

Preface

The present thesis has been written on the basis of the experimental activities conducted at the Engineering Department (ENDIF), University of Ferrara (Italy) from January 2013 to December 2015. The research activity described herein was conducted under the supervision of Eng. Mattia Merlin as main supervisor.

The aim of this work is the investigation of the recovery behaviour of NiTi shape memory alloys employed as active elements in adaptive composite structures. Particular attention was given to the development and testing of a SMA-based morphing blade for an automotive cooling fan whose development was made through the financial and technical support provided by Fratelli Rosati s.r.l of Leinì (Torino, Italy). The initial idea to develop an innovative method to vary the blade geometry of fan for cooling internal combustion engines was provided by Patent, whose ownership is of Fratelli Rosati s.r.l. and of which Eng. Guido Rosati and Eng. Mattia Merlin are the inventors. The present thesis origins both as a technology transfer activity and project of industrial interest.

The results presented in the thesis are part of the papers published during the three years' period which are:

1. A. FORTINI, M. MERLIN, R. RIZZONI, S. MARFIA, "TWSME of a NiTi strips in free bending conditions: experimental and theoretical approach", *Frattura ed Integrità strutturale*, **8**(29), 74–84, (2014)

2. A. FORTINI, M. MERLIN, C. SOFFRITTI, A. SUMAN, G. L. GARAGNANI, "Study of an active deformable structure with embedded NiTi shape memory alloy strips", *La Metallurgia Italiana*, **2**, 23–30, (2015)

3. A. SUMAN, A. FORTINI, N. ALDI, M. PINELLI, M. MERLIN, "Using shape memory alloys for improving automotive fan blade performance: experimental and computational fluid dynamics analysis"*, Proceeding of the Institution of Mechanical Engineers. Part A, Journal of Power and Energy*, **229**(5), 477–486, (2015)

4. A. FORTINI, A. SUMAN, M. MERLIN, G. L. GARAGNANI, "Morphing blades with embedded SMA strips: An experimental investigation"*, Materials & Design*, **85**, 785–795, (2015)

5. A. SUMAN, A. FORTINI, M. MERLIN, "A shape memory alloy-based morphing axial fan blade: functional characterization and perspectives"*, Energy Procedia*, **82**, 273–279, (2015)

6. A. FORTINI, A. SUMAN, N. ALDI, M. PINELLI, M. MERLIN, "A Shape Memory Alloy-Based Morphing Axial Fan Blade, Part I: Blade Structure Design and Functional Characterization", *Journal of Engineering for Gas Turbines and Power*, **138**(2), p. 022601 (8 pages), (2016)

7. A. SUMAN, A. FORTINI, N. ALDI, M. PINELLI, M. MERLIN, "A Shape Memory Alloy-Based Morphing Axial Fan Blade, Part II: Blade Shape and Computational Fluid Dynamics Analyses", *Journal of Engineering for Gas Turbines and Power*, **138**(6), p. 062604 (9 pages), (2016)

The findings of the study are mainly concerned with the investigation of the shape memory effect of NiTi alloy strips for the development of functional structure and the limitations of the research are:

- the NiTi alloys used were limited to the commercially available and therefore the transformation temperatures of the alloys were not well suited for the intended applications. In particular, this has an impact on: (i) the phase transformations of the NiTi alloys which were limited by the thermal performance of the experimental setup, (ii) the recovery behaviour of the functional structures is related to the shape memory effect of the SMA element in conjunction with the elasticity of the polymeric matrix;

- the recovery behaviour of the NiTi strips in partially constrained condition was affected by the properties of the polymeric compounds whose properties data were limited to the technical data of the manufacturer;

- the lack of a numerical analysis for the prediction and comparison with experimental observations related to the mechanical behaviour, during shape recovery in partially constrained conditions;

- the recovery behaviour proposed is for a limited number of cycles and higher numbers of subsequent activation thermal cycles should be analysed to assess the stabilisation of the behaviour.

In addition, the following list contains other publications concerning research works related to the three years' period but not included in the thesis:

A. L. LOMBARDO, A. ARREGHINI, E. BRATTI, F. MOLLICA, G. SPREDICATO, M. MERLIN, A. FORTINI, G. SICILIANI, "Comparative analysis of real and ideal wire-slot play in square and rectangular archwires", *The Angle Orthodontist*, **85**(5), 848–858, (2015)

B. M. MERLIN, M. SCOPONI, C. SOFFRITTI, A. FORTINI, R. RIZZONI, G. L. GARAGNANI, "On the improved adhesion of NiTi wires embedded in polyester and vinylester resins", *Frattura ed Integrità Strutturale*, **31**, 127–137, (2015)

C. C. SOFFRITTI, E. FABBRI, A. FORTINI, M. MERLIN, G. L. GARAGNANI, "Fakes in African art: study of a reliquary figure (Mbulu-Ngulu) from Gabon", *La Metallurgia Italiana*, **4**, 9–13, (2015)

D. M. MERLIN, A. FORTINI, R. RIZZONI, S. MARFIA, "Flexural recovery behaviour of a NiTi strip in partially constrained conditions", Proceedings of 6th ECCOMAS Conference on Smart Structures and Materials (SMART2013), Politecnico di Torino, Torino, 24-26 june 2013, (2013) Paper n° 20130425230124

E. D. CASARI, A. FORTINI, M. MERLIN, "Fracture behaviour of grain refined A356 cast aluminium alloy: tensile and Charpy impact specimens", Proceedings of XXII Convegno Nazionale IGF, Roma, 1-3 july 2013, 314–321, (2013)

F. A. FORTINI, M. MERLIN, C. SOFFRITTI, G. L. GARAGNANI, "Restoration of obliterated numbers on 40NiCrMo4 steel by etching method: metallurgical and statistical approaches", *Journal of Forensic Sciences*, **61**(1), 160–169, (2016)

Abstract

The ongoing employment of Shape Memory Alloys (SMAs) as solid-state actuators results from the Shape Memory Effect (SME) and the unique mechanical characteristics of these materials, including high reversible strain (up to 10 %), high-power to weight ratio and the ability to generate high recoverable stresses (up to 800 MPa). SMAs are frequently combined within polymeric materials, also reinforced with embedded fibres, to produce adaptive structures whose properties could be tuned in response to external stimuli. The integration of smart materials in actuation systems represents an excellent technological opportunity and an alternative solution to conventional mechanical systems for the development of mechanisms with improved simplicity and reliability. The possibility to use SMA elements for morphing structures is particularly attractive for aerodynamic applications where this actuation solution prevents the introduction of flow-disturbing control elements. The notion of smart advanced blades, which can control themselves and reduce (or eliminate) the need for an active control system, is a highly attractive solution in blade technology. Despite a large number of publications and patents relating to the employment of SMAs for enhancing aerodynamic and structural efficiency of automotive applications, specific studies on the behaviour of SMA-based morphing blades are not available in literature.

The aim of this work is the development and the experimental characterisation of a novel concept of morphing blade, intended for cooling fan of internal combustion engines for earth moving machines. The variable-geometry blade comprises a composite structure made up of a polymeric compound, for the elastically deformable body of the blade, with embedded SMA strips as active elements.

To assess the reliability of the SMA strip to provide the proper bending behaviour in the composite structure of the blade, the first phase of the work concerned the experimental characterisation of the NiTi material. The thermal characterisation allows to study the best shape setting parameters (temperature, time and strain) which were experimentally tuned to maximise the SME in the NiTi strip. The recovery behaviour of the SMA material, as a result of the thermally activated solid to solid phase transformations, was assessed by considering the percentage of shape recovery with the increasing number of thermal cycles. The experimental findings enabled to set the proper thermomechanical treatment related to the bending recovery performance of the strip.

Starting from the need to evaluate the actuation ability of the NiTi strip when it is indirectly embedded into a polymeric matrix, a proof of concept of composite structure, comprising a single strip and a polymeric compound was design on purpose. The bending ability of the structure was evaluated by means of repeated recovery cycles. Thermal activations were achieved by means of a fluid flow and an airstream flow heating/cooling systems.

The experiments performed on the concept of the single strip composite structure were useful for the development of the morphing blade. The study of its morphing capability was conducted by comparing the behaviour of four different polymeric compounds in order to establish the best compromise between stiffness and deflection behaviour for the intended application. The shape changes of the blade, arising from the SME behaviour of the embedded thermomechanically treated NiTi strips, were experimentally evaluated through a purpose-built wind tunnel, developed to reproduce the actual automotive thermal ramps of the heat exchanger. Experimental findings highlighted the opportunity to generate an innovative passive control system applied to an automotive cooling axial fan wherein the SMA driven activation enables the production of favourable aerodynamic shape changes.

Sommario

Il continuo impiego dei materiali a memoria di forma come elementi attivi deriva dall'effetto a memoria di forma e dalle peculiari proprietà meccaniche di questi materiali, tra le quali la capacità di recuperare elevate deformazioni (fino al 10 %), l'elevato rapporto potenza su peso e la capacità di generare elevati sforzi (fino a 800 MPa). Le leghe a memoria di forma sono spesso utilizzate all'interno di materiali polimerici, eventualmente rinforzati con fibre, per realizzare strutture attive deformabili le cui proprietà posso essere modificate in risposta a stimoli esterni. La possibilità di integrare materiali intelligenti all'interno di sistemi attuativi rappresenta una interessante scelta tecnologica ed una soluzione alternativa all'impiego di sistemi meccanici convenzionali, nello sviluppo di meccanismi con migliore semplicità costruttiva e fattibilità.

La possibilità di utilizzare elementi in lega a memoria di forma per la realizzazione di strutture deformabili è di particolare interesse nelle applicazioni aerodinamiche dove tale soluzione costruttiva permette di limitare l'introduzione di elementi di controllo che alterano il flusso. Il concetto di pale a geometria variabile, che possono modificare la loro forma in modo attivo, riducendo (o eliminando) così l'impiego di sistemi di controllo, rappresenta una soluzione estremamente interessante. Sebbene vi siano numerose pubblicazioni e brevetti riguardanti l'impiego di elementi in lega a memoria di forma per il miglioramento dell'efficienza aerodinamica e strutturale dei dispositivi nel settore automotive, studi specifici relativi al comportamento di pale a geometria variabile ottenute con leghe a memoria di forma non sono presenti in letteratura.

Scopo del presente lavoro è lo sviluppo e la caratterizzazione sperimentale di un innovativo concetto di pala a geometria variabile, ideata per l'impiego all'interno di ventole di raffreddamento di motori a combustione interna di macchine movimento terra. La pala in oggetto prevede una struttura composita formata da una matrice polimerica, che fornisce l'elasticità al corpo palare, al cui interno sono alloggiate lamine in lega a memoria di forma che rappresentano gli elementi attivi.

Al fine di studiare la fattibilità del sistema in termini di adeguato comportamento flessionale delle lamine all'interno della struttura composita della pala, la prima parte del lavoro ha riguardato la caratterizzazione sperimentale del materiale in lega NiTi. La caratterizzazione termica ha permesso l'ottimizzazione dei parametri di trattamento termomeccanico di memorizzazione della forma (temperatura, tempo e grado di deformazione), i quali sono stati determinati sperimentalmente al fine di massimizzare l'effetto a memoria di forma della lamina. Il recupero della forma da parte del materiale, come risultato delle trasformazioni allo stato solido termicamente attivate, è stato valutato prendendo in considerazione l'evoluzione del valore percentuale di recupero della forma all'aumentare

del numero di cicli di attivazione eseguiti. I risultati sperimentali hanno permesso di stabilire il trattamento termomeccanico più adatto in relazione al recupero a flessione da parte della lamina.

Partendo quindi dall'esigenza di valutare la capacità di attivazione della lamina in lega NiTi quando inserita all'interno di una matrice polimerica, è stato progettato e realizzato un primo prototipo di struttura composita costituito da una singola lamina collocata all'interno di una matrice polimerica. La capacità di deformazione a flessione è stata studiata attraverso l'esecuzione di cicli di attivazione ripetuti. Le attivazioni termiche hanno previsto l'impiego sia di un sistema a fluido sia di un sistema a flusso d'aria.

Lo studio sperimentale condotto sul prototipo di struttura composita con una singola lamina è stato propedeutico al successivo sviluppo della pala a geometria variabile. L'analisi della sua capacità di deformazione è stata condotta attraverso il confronto tra quattro diverse matrici polimeriche al fine di stabilire il miglior compromesso tra rigidezza e deformazione flessionale per la specifica applicazione in esame. Le modifiche di forma della pala, derivanti dall'effetto a memoria di forma delle lamine, sono state studiate sperimentalmente mediante l'impiego di una galleria del vento appositamente progettata e realizzata, al fine di riprodurre le reali rampe termiche degli scambiatori di calore. I risultati sperimentali hanno evidenziato la possibilità di realizzare un sistema di controllo passivo per ventilatori assiali applicati nel settore automotive sfruttando un sistema di attuazione con leghe a memoria di forma in grado produrre modifiche della geometria palare che ne migliorano il comportamento aerodinamico.

Table of contents

List of Figures

Chapter 1

Chapter 2

Chapter 3

Chapter 4

List of Tables

List of Symbols

Normal letters

A	austenite
C	stress influence coefficient
E	elastic modulus
h	hub
h	thickness
LE	leading edge
M	martensite
m	midspan
m	maximum camber
n	rotational velocity
n	number of cycles
R	radius
s	shroud
SM	strip at midspan
SS	strip at shroud
T	temperature
t	time
TE	trailing edge
w	heat flow
z	coordinate along the thickness
z_0, z_m, z_+	mapping coordinates of the transformation fronts
ΔH_A	latent heat for austenitic transformation
ΔH_M	latent heat for martensitic transformation

Greek letters

ε	strain
ε_L	maximum strain related to the detwinning
ε_{tr}	strain of training
λ	distance from the neutral axis
ξ_s	single-variant martensite volume fraction
ξ_{sr}	residual single-variant martensite volume fraction

σ	stress
χ	curvature

Subscripts and superscripts

0	initial
A	austenite
C	cold
f	finish
H	hot
i	ith
M	martensite
max	maximum
non-def	non deformed
r	residual
s	start
t	twinned martensite

Acronyms

2D	Two-Dimensional
3D	Three-Dimensional
CAD	Computer Aided Design
DSC	Differential Scanning Calorimetry
Nitinol	Nickel Titanium Naval Ordnance Laboratory
NURBS	Non Uniform Rational Basis-Splines
OWSME	One-way Shape Memory Effect
PMMA	PolyMethyl MethAcrylate
RE	Reverse Engineering
SBTF	Single Blade Test Facility
SDK	Software Development Kit
SE	Superelastic Effect
SIM	Stress-Induced Martensite
SMA	Shape Memory Alloy
SMC	Shape Memory Composite
SME	Shape Memory Effect
TTRs	Transformation Temperatures
TWSME	Two-way Shape Memory Effect

Chapter 1

Introduction to shape memory alloys

This chapter is focused on the theoretical aspects and fields of application of Shape Memory Alloys (SMAs). An overview of their properties, from a microstructural point of view, is proposed. The employment of these materials as active elements in actuation components and the review of recently industrial applications are also discussed to understand the potential of SMAs for engineering systems.

1.1 Principles of shape memory alloys

The materials which are able to exhibit their own sensing and actuation abilities depending on sensed environmental stimuli are called smart materials. Among them, Shape Memory Alloys (SMAs) are materials endowed with the ability to memorise and recover their original shape from a seemingly permanent strains, in response to changes in external stimuli such as temperature or stress (Otsuka and Wayman, 1998). This unique behaviour of recover the original geometry is known as Shape Memory Effect (SME).

The SME was firstly discovered in 1932 in an AuCd alloy by Ölander, who found that this alloy could be deformed when cool and recover its original shape on heating (Ölander, 1932). Even if nickel-titanium alloy was discovered in 1959, it was only in 1962 that William Buehler and Frederick Wang observed the shape memory ability of a NiTi, revealing the potential to commercialise these alloys (Buehler *et al.*, 1963). It was only since 1971, when a significant recoverable strain was observed in a NiTi alloy at the Naval Ordnance Laboratory, that this phenomenon started to attract attention for engineering applications. In honour of the discovery at the Naval Ordnance Laboratory this NiTi alloy was identified with the term NiTiNOL. Since then, the demand for SMAs for engineering application has been increasing in several fields. A recently BCC research reports that the global market for smart materials was about USD 19,6 billion in 2010 forecasted to reach over USD 40 billion by 2016 (McWilliams, 2011). As shown in Fig. 1.1, the largest application segment of the market is actuators and motors, with sales of nearly USD 10,8 billion in 2010 and forecasted to reach USD 25,4 billion by 2016.

The property of SMAs to recover their shape is dependent on reversible crystallographic phase

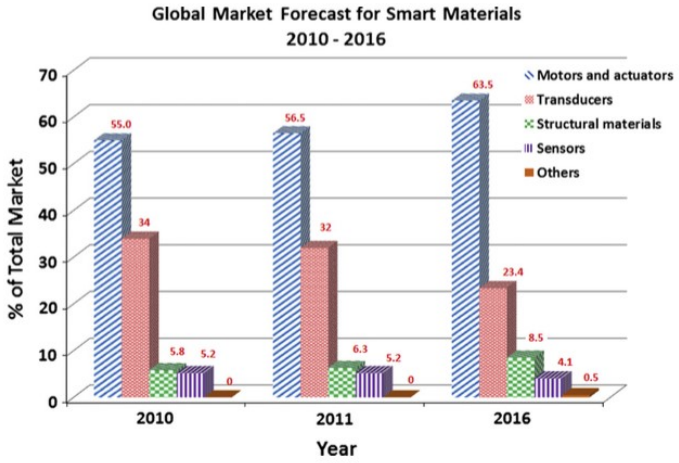

Figure 1.1 – Global market forecast for smart materials for 2010–2016 (Jani *et al.*, 2014)

transformations which occur between two crystallographic phases. In the absence of applied load, the cubic crystal structure is stable at high temperature while the monoclinic crystal structure is stable at low temperature. The high temperature phase is called austenite (A) while the low temperature phase is called martensite (M). The transformation from one crystallographic phase to the other occurs by means of displacive transformations. Unlike diffusional transformations, in which the new phase arises from long range diffusion and atomic migration, displacive transformations are the result of shear lattice distortion. As a result, the atoms are rearranged into a more stable crystal structure without changing the chemical nature of the matrix. The martensitic transformation which occurs on cooling by the nucleation and growth of the martensitic phase from the austenitic phase and it is called forward transformation.

In the absence of applied load, the temperature induced phase transformation on cooling leads to the formation of twinned martensite (M^t). Austenite shows a symmetric structure with a high elastic modulus while boundaries of twinned martensite can be easily moved and thus SMAs elements can be deformed with quite low forces in the martensitic state. Each formed martensitic crystal has its orientation direction, namely variant. During the forward transformation there is an arrangement of the variants of the twinned martensite. As the resulting macroscopic shape change is negligible, the twinned martensite is also named self-accomodated martensite. A scheme of the crystal structures of self-accomodated martensite along with associated forward transformations is depicted in Fig. 1.2. On cooling the transformation from austenite to twinned martensite begins at the martensitic start temperature (M_s) and continue to evolve according to the temperature decrease up to the martensitic finish temperature (M_f). Below the M_f temperature the forward transformation is completed and the crystal structure is made up of twinned martensite. Similarly, heating the material from the martensitic phase the reverse transformation occurs with no associated shape changes. Twinned martensite begins to transform into austenite at the austenitic start temperature (A_s) and when the austenitic finish temperature (A_f) is reached, the material is fully austenitic. These four temperatures are also known as Transformation Temperatures (TTRs). It should be noted that there is a hysteresis between the transformation regions and there is a temperature range over which martensite and austenite coexist. The transformation from martensite into austenite always takes place at higher temperature compared with the forward transformation. Depending on the thermomechanical history of the material, the shape of the hysteresis curve may vary substantially.

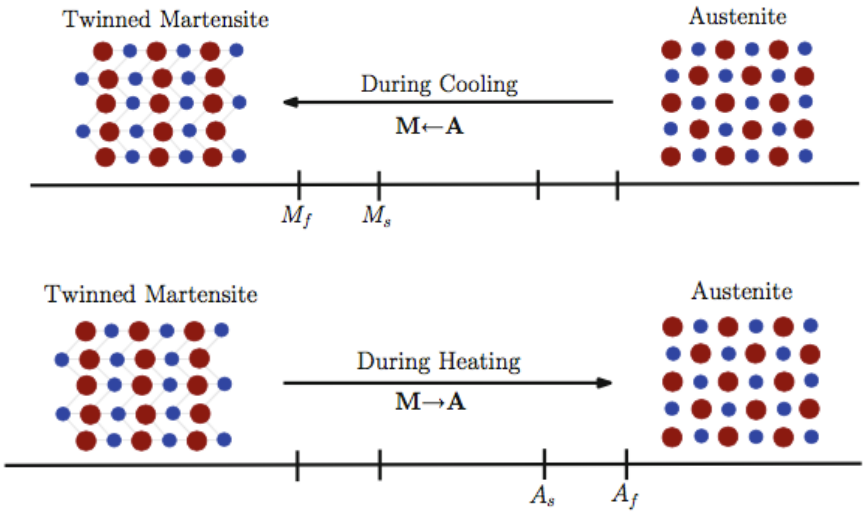

Figure 1.2 – Phase transformations and crystallographic structures associated with forward and reverse transformation under zero load case (Rao *et al.*, 2015)

A simplified scheme of a hysteresis curve is depicted in Fig. 1.3. As shown, the martensite is formed on cooling and its volume fraction increases as the temperature is reduced since it is independent of time and it is dependent only on temperature. Hysteresis is an important characteristic of SMA and devices made up of these alloys. TTRs and the hysteresis loop have to be considered during the material selection since they can deeply affect the behaviour. To this regard, for fast actuation applications a small hysteresis is required while larger hysteresis is required to retain the predefined shape within a large temperature range.

As stated above, in the absence of applied load, austenite transforms on cooling to twinned or self-accommodated martensite with no associated shape change. If this self-accomodated martensite is subjected to an applied load the detwinning process takes place: according to the orientation of the applied stress, the structure evolves to the most preferred variant. This reorientation causes a macroscopic shape change: this deformed configuration is retained even after the unloading (Lagoudas, 2008). However, the subsequent heating above A_f leads to the reverse phase transformation from detwinned martensite to austenite allowing the shape recovery through the SME. Finally, cooling back this austenite structure will lead to the formation of twinned martensite again, without shape change. Figure 1.4 shows a grid-like representation of austenite, twinned and detwinned martensite structures.

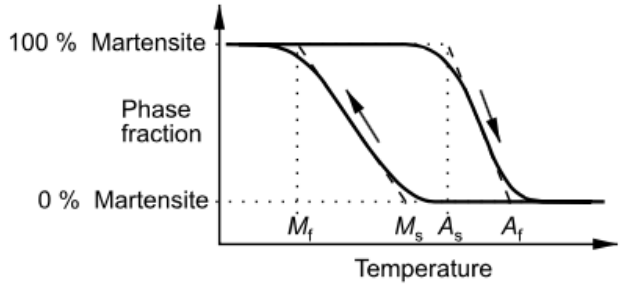

Figure 1.3 – Transformation temperatures and hysteresis curve (Janocha, 2007)

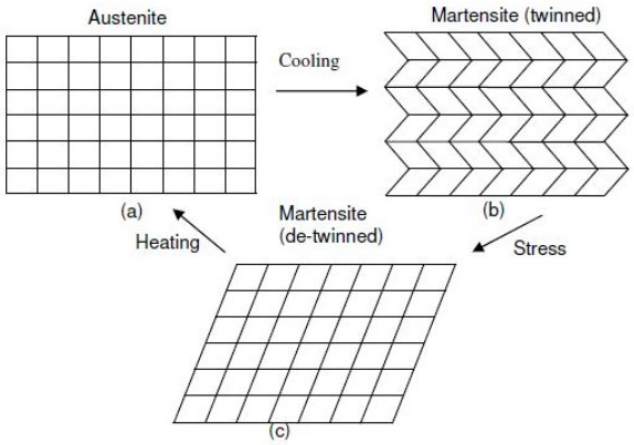

Figure 1.4 – Schematic of the SME: detwinning with the applied stress and recover by heating under no load condition (Cismasiu, 2010)

In order to study how the TTRs are influenced by the applied stresses, the phase diagram reported in Fig. 1.5, could be helpful. As a function of both applied stress and temperature, the plot addresses the region in which phases are present in pure form or as coexisting phases. The ordinate axis shows the so-called detwinning start stress (σ_s) and the detwinning finish stress (σ_f), which correspond to the minimum stress required for starting the detwinning and the stress to complete the detwinning of the martensite, respectively. As can be seen, the transformation from twinned martensite in detwinned martensite begins above the σ_s threshold value and the detwinning is completed only at the σ_f value: within these two stress levels twinned and detwinned martensite coexist. The shape change which was produced by the descripted path is not reversible since, upon the load is removed, the martensite will remain detwinned. The recover of the strain is achieved by heating the martensite above the A_f temperature, which varies in function of the applied load: higher stresses leading to higher TTRs values as it is highlighted form the positive slope of the lines, which indicate the austenite to detwinned martensite transformation regions.

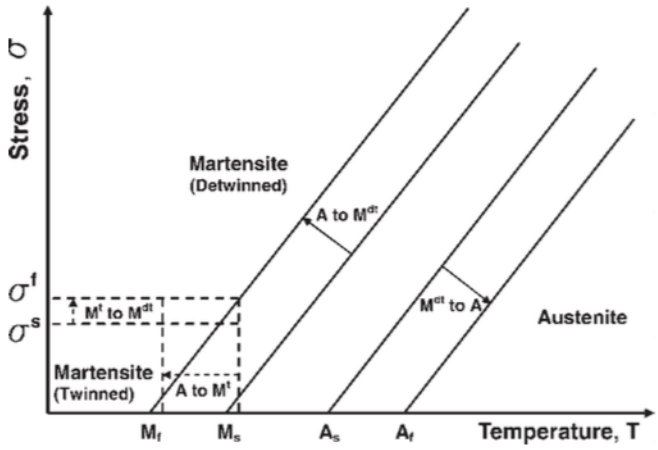

Figure 1.5 – A schematic stress-temperature phase diagram (Hartl *et al.*, 2007)

Since both the forward and reverse transformation are accompanied by the release and absorption of latent heat, the heat of these transformation and the TTRs are commonly measured by means of the Differential Scanning Calorimetry (DSC). The SMA material, in stress-free annealed condition, and a reference sample are put in the calorimeter which heats and cools the samples at a defined heating/cooling rate. The system registers the rate at which heat energy is supplied to a specimen to maintain a constant heating/cooling rate. Therefore, the term differential refers to the different energy inputs between the specimen and the reference in terms of heat flow rates. The resulting DSC curve plots the heat flow versus temperature, is reported in Fig. 1.6. If the material, from the martensitic state, it heated the reverse transformation begins at A_s and, in order to maintain the heating rate, additional heat power should be provided to the specimen. This change in the heat flow is represented as an endothermic peak on heating. Similarly, on cooling the exothermic peak indicates the forward transformation from austenite to martensite. The characteristic TTRs can be extrapolated from the DSC plot by the intersection between the tangents to the start/end regions of the peak and the baseline, according to the tangential line method (Lagoudas, 2008).

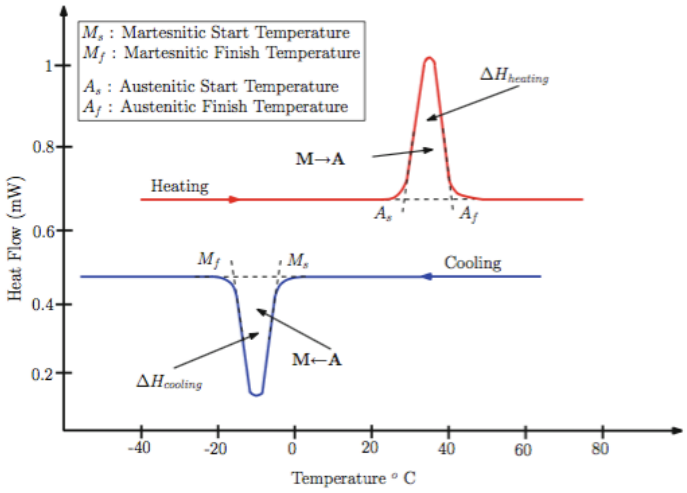

Figure 1.6 – DSC curve for an SMA with the TTRs and the associated latent heat (Rao *et al.*, 2015)

1.2 Shape memory effect and superelasticity

As mentioned, the SME is the property of the material to recover mechanically induced strains (up to 10 %) when it is deformed in the low temperature phase and subsequently heated to the high temperature phase. The return to austenite results in the macroscopic shape change associated with the recovery of the original shape of the material.

To better understand the SME, in Fig. 1.7 a stress-strain-temperature plot is reported. The start of the loading path, identified with A in Fig. 1.7, it is above the A_f and thus the material is fully austenitic. Upon cooling, in the absence of an applied load, the crystal structure changes from austenite to twinned martensite (point B). As stress is applied and increased, the the twinned martensitic variants twin into detwinned martensite. The detwinning process causes a large macroscopic strain (6–8 %) and a shape change, identified by the so-called martensitic plateau. Upon unloading from point C, the elastic portion of the strain is recovered and the material does not return back to its non deformed state because of the 4–6 % of inelastic strain from the detwinning.

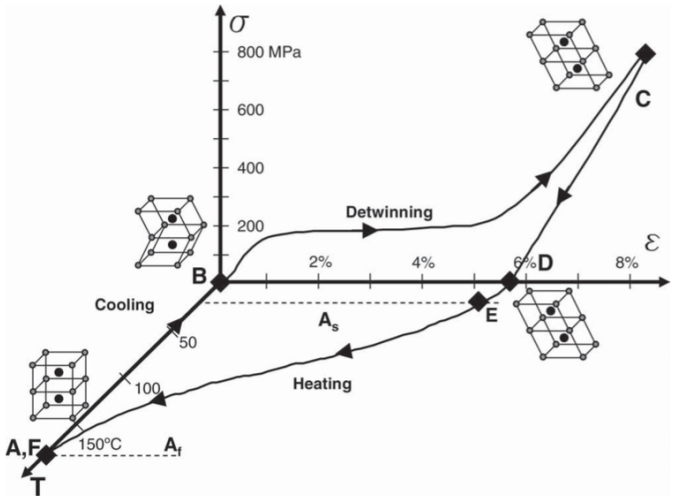

Figure 1.7 – Stress-strain-temperature curve of a NiTi SMA (Hartl *et al.*, 2007)

However, this is a seemingly permanent strain since it can be recovered upon heating the SMA, to allow the reverse transformation to the austenitic phase to occur. The recovery process begins at the austenitic start temperature, point E, and it is completed at the austenitic finish temperature, identified with point F, which coincides with the starting point of the loading path. As a result, the inelastic strain is fully recovered and the original shape is restored. It should be noted that, once the shape has been recovered, there is no macroscopic change when the specimen is cooled to below M_f and the SME is reactivated only by deforming the material from the twinned martensite to the detwinned martensite. For this reason, the shape memory effect is also referred to as One-way Shape Memory Effect (OWSME) since it is a one-time phenomenon.

The process described above could be also explained using a coil spring, as it is proposed in Fig. 1.8. A shape memory coil spring is extended when it is in martensitic phase thus providing the condensation of many twin variants into a single favoured variant. This macroscopic deformation, depicted as the spring in the stretched shape, remains when the stress is released, as it happens in common plastic deformation. However, if the material is heated above A_s the spring starts to contract to return to the original shape, thanks to the reverse transformation into austenite, which is completed at the A_f temperature. On the contrary, no macroscopic shape change is associated to the subsequent cooling to the martensite phase and, therefore, the contracted shape of the spring remains. To produce another shape recovery cycle the spring must be deformed to provide the detwinning of the martensite.

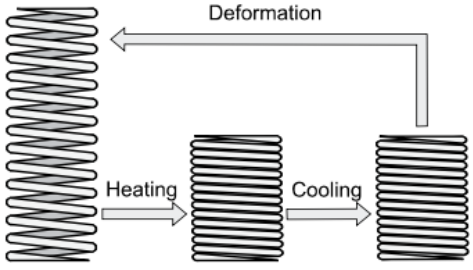

Figure 1.8 – One-way shape memory effect in a coil spring (Janocha, 2007)

In addition to the OWSME, SMAs may also show another particular property which is the so-called Two-way Shape Memory Effect (TWSME). Through the OWSME the material could recover the macroscopic shape of the austenitic phase upon heating above A_f, while through the TWSME, it also exhibits a return to the reoriented martensitic shape upon cooling below M_f, in the absence of applied stress. Therefore, the material is able to remember the high-temperature shape, above A_f, and the low-temperature shape, below M_f. With reference to Fig. 1.9, the TWSME enables the extension of the contracted spring when it is heated above A_f and the spontaneous contraction when it is cooled below M_f.

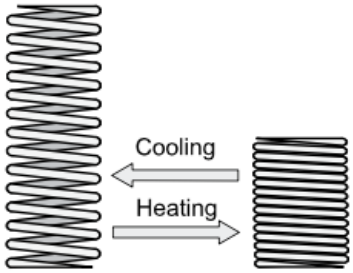

Figure 1.9 – Two-way shape memory effect in a coil spring (Janocha, 2007)

This spontaneous repeatable shape change on heating and cooling is an acquired behaviour, rather than an inherent property of the material, obtained by specific thermomechanical loading cycles, named training treatments, to which the SMA must be subjected. A training procedure usually consists of repeated deformation and transformation between austenite and martensite to develop a residual internal stress state which produces a dislocation structure. From a crystallographic point of view, it is widely accepted that preferential martensite formation is due to the generation of permanent defects in the austenitic phase resulting from training procedure (Liu *et al.*, 1990, Perkins *et al.*, 1984). Generally, training procedures have the purpose to induce the low temperature shape in the sample introducing permanent defects such as dislocations, stabilised stress induced martensite and precipitates. These dislocation structures create an isotropic stress field which guides the growth of certain martensitic variants, towards the preferred orientations, regarding the deformation adopted during training when SMA is stress-free cooled. This results in a macroscopic shape change between the phase transformation temperatures.

The training process typically consists of several cycles of deformation to the desired low-temperature shape and subsequent shape recovery by heating. Different training methods for obtaining the TWSME are described in literature and the influence of the type and training parameters, the stability of the TWSME during thermal cycling as well as the efficiency of the methods have been widely investigated (Lahoz *et al.*, 2002). Common methods of training include: shape memory cycling, pseudoelastic cycling, combined shape memory cycling/pseudoelastic cycling and constrained cycling of deformed martensite (Luo *et al.*, 2007, Perkins *et al.*, 1990). All of these thermomechanical treatments deal with the repetition of a procedure that considers the transformation from austenite to a preferentially oriented martensite or from deformed martensite to austenite.

The other unique behaviour observed in SMAs, with respect to common engineering alloys, refers to the ability of recover large strains (8 %) as a result of mechanical loading and unloading in

isothermal conditions. This phenomenon is known as Superelastic Effect (SE) since the material, at a temperature above A_f, is able to support relatively high strains in a loading process and, by means of a hysteresis loop, recovers its original shape when the load is removed. Both SME and PE concern the ability to recover the original shape of the material by heating above the austenitic finish temperature and by removing the mechanical load, respectively. To better understand the material response, a superelastic loading cycle is depicted in the σ–ε diagram of Fig. 1.10. Starting from a temperature above A_f at zero stress level, the material, in the austenitic phase, is subjected to a mechanical load which leads to the transformation into martensite in correspondence of the σ^{Ms} stress level indicated by point 2. The element deforms like a conventional linear elastic material under load. With increasing loads, the stress-induced martensite (SIM) is formed with large reversible strains at nearly constant stresses, resulting in a stress plateau shown from point 2 to point 3 of Fig. 1.10. The SIM formation and detwinning is fully completed at point 3 that is the σ^{Mf} stress level which marks the end of the transformation. Further increase in loading will lead to elastic deformation of the detwinned martensite, as it is indicated by the slope of the curve above point 3. Upon unloading the stress is released and no transformation occurs up to point 4. At this stage, which corresponds to the austenitic start level stress σ^{As}, the martensite starts to transform into austenite and at the end of the unloading plateau the transformation is complete, as indicated by the σ^{Af} level stress. Finally, from point 5 to point 1 the material is elastically unloads.

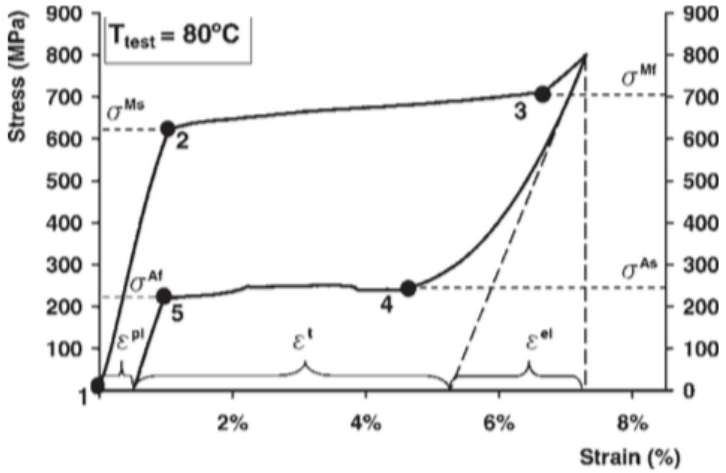

Figure 1.10 – SMA superelastic loading cycle (Hartl *et al.*, 2007)

1.3 Commercial alloys

Over the last decades a wide variety of SMAs have been investigated and several compositions have been studied, by adding different alloying elements (such as zinc, copper, gold and iron) to existing alloys, providing a wide variety of compositions to choose from. Alloys with shape memory effect are different amongst themselves with respect to TTRs, hysteresis behaviour, fatigue strength and other properties. Of these alloys the most commonly used are the nickel-titanium (NiTi), the copper-based SMAs, such as the copper-zinc-aluminum (CuZnAl) and the copper-aluminum-nickel (CuAlNi), and the iron-based SMAs, such as iron-nickel-cobalt-titanium (FeNiCoTi). Figure 1.11 summarises the most important properties of commonly used shape memory alloys.

	NiTi	CuZnAl	CuAlNi	FeNiCoTi	Unit
Range of transformation temperature	−100 to +90	−200 to +100	−150 to 200	−150 to +550	°C
Hysteresis width	30	15	20		K
Max. one-way effect	8	4	6	1	%
Max. two-way effect	4	0.8	1	0.5	%
Fatigue strength	800 ... 1000	400 ... 700	700 ... 800	600 ... 900	N/mm^2
Admissible stress for actuator cycling	150	75	100	250	N/mm^2
Typ. number of cycles	>100 000	10 000	5 000	50	
Density	6450	7900	7150	8000	kg/m^3
El. resistivity	80 ... 100	7 ... 12	10 ... 14		$10^{-8}\,\Omega\,m$
Young's modulus	50	70 ... 100	80 ... 100	170 ... 190	GPa
Corrosion resistance	very good	fair	good	bad	

Figure 1.11 – Properties of some shape memory alloys (Janocha, 2007)

Even if many alloys with SME are low-cost, commercially available and provide designers great flexibility according to their different transformation temperatures, NiTi-based alloys are much more preferable for most applications. In fact, even if the range of TTRs is limited to approximately 100 °C, NiTi alloys show the best properties for actuator purposes. Another drawback is the considerable hysteresis width. Despite this, there are some important benefits like high electrical resistivity, high mechanical strength, large recoverable strains resulting in a higher work density, easy workability, biocompatibility and corrosion resistance comparable to stainless steel. Copper-based alloys (CuZnAl, CuAlNi) are an attractive alternative to NiTi given their good electrical and thermal conductivity, their formability along with their lower cost (can be 5-10 times more cheap than NiTi). Compared to NiTi alloys they exhibit wider range of transformation temperatures but, since lower lifespan and lower work output, they are not feasible for electrical actuator applications. Finally, other shape memory alloys such as FeNiCoTi or NiTiHf, NiTiPd, NiAl have not been perfected for commercial use yet.

1.4 Functional structures

The so-called adaptive composite structures are realised by incorporating an active element with other functional or structural materials. SMAs are frequently combined within monolithic or composite host materials to produce devices whose properties could be tuned in response to environmental stimuli (Wei *et al.*, 1998). These structures could be simple beams controlled with a single actuator or more compliant geometries controlled by a network of actuators.

The integration of smart materials in actuation systems represents an excellent technological opportunity and an alternative solution to conventional mechanical systems for the development of simple, very compact and reliable active mechanisms. A complete and extensive review of hybrid SMA composites which deals with constitutive models, technological problems that arise in the manufacturing processes and structural problems of SMA structures is proposed by Birman (1997). Owing to the simplicity in the fabrication of commercial shape memory alloys in form of wires, fibres, ribbons, particles and thin films it is possible to realise a large variety of adaptive composite structures by means of conventional fabrication techniques.

Since SMAs are able to provide large actuation forces and displacements together with high strain outputs, they are frequently employed for the development of hybrid composite structures with adaptation features. Most of these active composite structures are made by directly or indirectly embedding shape memory elements into thermoplastic and thermosetting matrices. Under constrained conditions, SMA elements work against the elastic stiffness of the host matrix, biasing their strain recovery. Thus, the phase transformation is accompanied by large recoverable transformation strains which lead to the generation of considerable stresses. SMA elements embedded in composite materials as active component yield adaptive composite structures with large bending deformation capabilities when activated.

The development of an adaptive structure requires that SMA elements are integrated in the host material such as a composite one. For this reason, it is clear the necessity to guarantee the right synergy between the important parameters of the SMA actuator and the properties associated with the host structure. Thus, these devices usually take advantage of the adhesion between the SMA element and the matrix. An example of composite beams embedded with prestrained NiTi wire is reported by Zhou and Lloyd (2009). The authors described an experimental study focused on the manufacturability and actuation repeatability of the composite beams (E-glass/epoxy and carbon/epoxy). Figure 1.12 depicts the E-glass/epoxy beam actuated by an applied current.

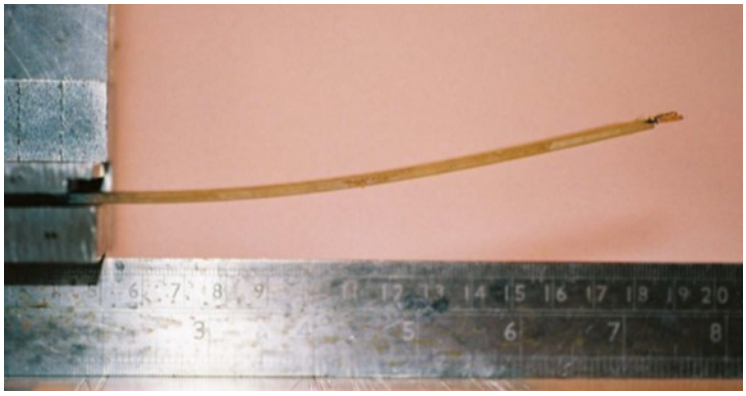

Figure 1.12 – Actuated E-glass/epoxy beam (Zhou and Lloyd, 2009)

The main issues of embedding NiTi wires into a polymer matrix are related to manufacturing difficulties and problems associated with interfacial bonding. To overcome these limits related to the adhesion characteristics, other solutions were evaluated, such as incorporating the SMA wires into the polymeric matrix by means of coupling sleeves. This solution enables the thermal buckling of the composite due to the thermal stresses induced by the activation of the SMA elements.

To this regard, Baz *et al.* (2000) proposed a composite beam reinforced with NiTi strips, indirectly embedded inside sleeves, located at the neutral planes and arranged parallel to the longitudinal axes of the composite beam, as can be seen from Fig. 1.13. The strips, prior to the insertion into the beam, were thermally trained in order to memorise controlled transverse deflections. The experimental investigations and the related models proposed by the authors assessed the advantages of the non-embedded solution for beam shape control and for structural stiffness of the matrix.

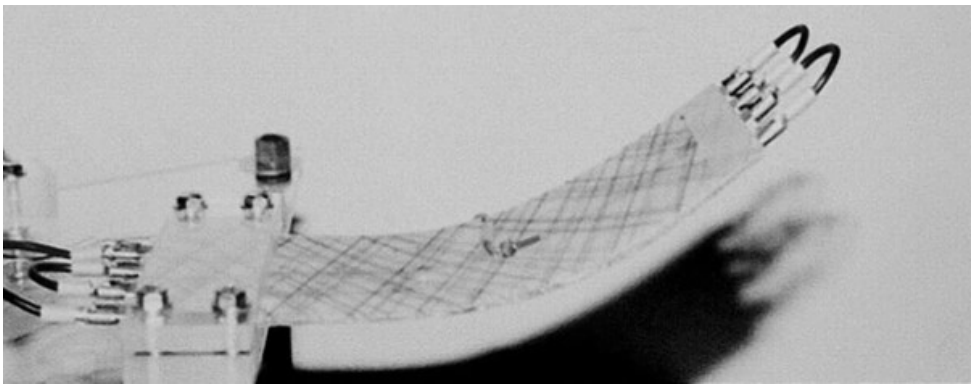

Figure 1.13 – Actuated fiberglass beam reinforced with NiTi strips (Baz *et al.*, 2000)

1.5 SMA-based actuators

A sensor is a device which converts a mechanical signal into a non-mechanical output, while an actuator converts a non-mechanical input into a mechanical output, such as moving an object, either on demand or in response to certain environmental changes (temperature, pressure, etc.). Active materials, such as SMAs, when subjected to non-mechanical field provide a mechanical response which is typically one or more orders of magnitude greater than the response resulting from conventional material behaviour such as thermal expansion (Lagoudas, 2008). Taking advantage of the solid-to-solid martensitic phase transformations, which allow the development of large recoverable strain, shape memory alloys are widely used as actuator elements (e.g. valves, active actuators, on/off devices). As a result, they are able to promote the development of more advanced and cheaper actuators with a significant reduction in mechanical complexity and size.

According to the load case, the functions of SMA actuators are usually classified as: (i) free recovery, (ii) constrained recovery and (iii) work production. These functional mechanisms of SMA actuators are summarised in Fig. 1.14 which shows the stress-strain diagrams for the three cases, as it is reported by Kohl (2004).

Figure 1.14a shows the stress-strain diagram for a SMA element in the absence of an external load. The material is deformed in its martensitic state and, if the stress is released, it remains in stretched condition until it is heated above the transition temperature in the absence of any constraint. This promoted the recovery of the original form and any macroscopic change occurs on cooling below the transition temperature. In this process, the material only provides motion or strain of the device and thus this behaviour is commonly referred to as free recovery.

As mentioned, SMAs phase transformations are accompanied by large recoverable strains which can be transformed into considerable stresses if the material is properly constrained. Figure 1.14b refers to a SMA component which is prevented from changing its shape on heating above A_f thus exerting a

large force. In the majority of real applications SMAs are subjected to an external load which prevents the returning to its original shape upon heating and it is described as constrained recovery.

When, the SMA component overcomes an external reset force, on heating above its A_f temperature, it generates motion and produces work. When cooled down, the reset force causes a movement back into the initial position. The principle of work production with an external reset mechanism is typical of most SMA actuators. Figure 1.14c shows reset movement for a constant reset force, whereby the stress remains unchanged.

Three basic types of actuators can be identified by using one-way SMAs, as it is reported in Fig. 1.15. Figure 1.15a reports an actuator in which the SMA element, which is in the martensitic state, is initially elongated by the action of an external force, indicated as F. On heating, the element comes back to the initial condition providing the movement of the weight P in the direction of the arrow. This type of actuator is known as one-directional actuator. If, instead, a spring is adopted to generate the restoring force, the actuator is named bias force actuator (Fig. 1.15b). In this case, the device is able to move the weight back and forth by the action of the SMA element, which is first elongated at low temperature, before the insertion. On heating, the SMA recovers its shape and pulls the bias spring, which stores potential energy in it. Finally, when the SMA is cooled down the energy of the spring is released and the SMA element deforms back, completing the cycle. In the last type of actuator, namely differential actuator, the system is composed by a SMA element with initially stored energy and an opposing SMA element which provides the bias force (Fig. 1.15c). By appropriately heating/cooling strategy, the actuator produces the intended motion and the weight moves back and forth by heating and cooling the two elements alternatively. It should be noted that the behaviour of the differential actuator is similar to a SMA material which has been trained to acquire the TWSME. Even though these two approaches provide the same function, a bias actuator enables to obtain higher actuation stress and larger actuation strain compared to SMA with the two-way shape memory effect (Sun *et al.*, 2012).

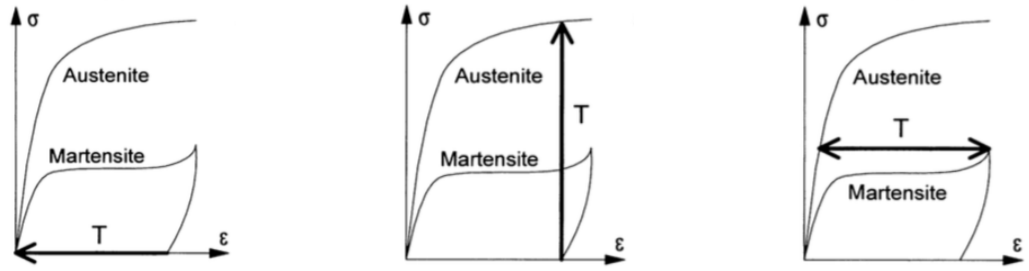

(a) (b) (c)

Figure 1.14 – Functional mechanisms of SMA actuators in stress-strain diagram: (a) free recovery, (b) constrained recovery and (c) work production at constant reset force (Kohl, 2004)

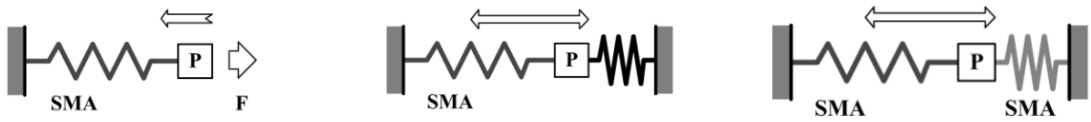

(a) (b) (c)

Figure 1.15 – Basic types of SMA actuators: (a) one-directional actuator, (b) bias force actuator and (c) differential actuator (Liang *et al.*, 1992)

The different modes of operation of SMA actuators can be summarised as: (i) constant force mode, (ii) constant deflection mode and (iii) simultaneous force/deflection mode (Rao *et al.*, 2015). Actuators which operate at constant force manner have the SMA element which works against a constant force and vary its shape according temperature changes, as depicted in Fig. 1.16. As can be seen, the spring is contracted at a temperature below M_f and deforms when an external load is applied. Subsequently, upon heating to above A_f, the spring contracts and reaches an intermediate configuration between the initial condition and the deformed condition. Finally, on cooling the spring comes back to the deformed condition. This thermally-activated behaviour enables the SMA element to work as a thermal actuator since it can lift the weight.

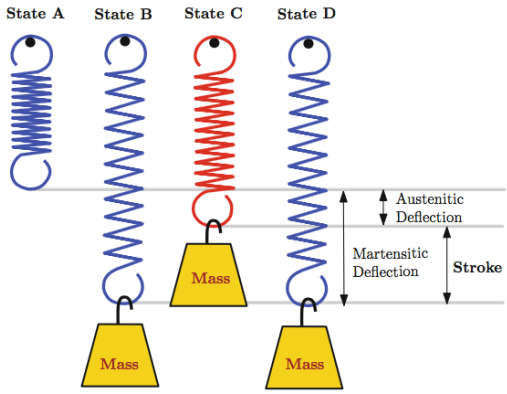

Figure 1.16 – Example of constant force mode of a SMA spring (Rao *et al.*, 2015)

As regards the constant deflection mode, the SMA element is constrained and the force output from the spring varies with temperature. This method, only applicable with small diameter SMA elements which are able to provide enough heating, is really simple but needs the electrical insulation of the element. When a martensitic wire, constrained at constant deformation, is heated above A_f the recover to original shape induces a recovery pull force due to external constraint. Note that this recovery force can be tweaked by changing the operating temperature above A_f. Thus, internal stresses are continuously changing and the transformation is spread over a range of temperatures.

Finally, the simultaneous force/deflection mode typically occurs in real application where force and deflection vary with temperature. As a consequence, the systems consists of an SMA spring working against a steel bias spring. When the temperature is below M_f the bias spring compresses the SMA spring and upon heating above A_f the recovery force of the SMA spring compress the steel spring.

As stated above, actuators have the ability to change the shape, stiffness, position, natural frequency, damping, friction, fluid flow rate and other mechanical characteristics in response to changes in temperature, electric field or magnetic field (Janocha, 2007). SMAs employed as actuators to generate repeated movements have therefore to be heating above the transition temperature A_f. According to the heating method, actuators can be divided into thermal actuators and electrical actuators. Thermal actuators combine the sensing and the actuating functions and they work, by changing shape and/or generating a force, as they are heated by changes in ambient temperature. The function of electrical actuators, on the other hand, is simply to move an object or perform a task on demand. They are heating by Joule heat created by direct flow of an electrical current, which enables the recovery of the original shape by internal heating above A_s.

With regards to the heating mode, SMAs wires or spring, by virtue of their small diameter, may by heated up by passing an electrical current through them. This method, applicable only to small diameter SMA elements which are thus able to reach the electrical resistance to provide heating, is very simple (no heater or cooler are necessary). Despite that, high electrical resistance and electrical connections, with low electrical resistance between the SMA and dissimilar conductive material, are request. Relatively high electrical resistance of SMA is required to avoid a high electrical current for actuating the SMA. Even if the small or thin structure of SMA has high electrical resistance, it cannot generate high power. An array of small or thin SMA structures connected as a series circuit can solve this problem, but the structure is relatively complex. A rapid heating by means of electrical current can be achieved by applying large electrical currents to increase the heating rate. Conversely, in case of bulk SMA they can be heated by passing an electrical current through a high resistance wire or tape, wrapped around the SMA element. In this case as well, the wire or tape needs to be electrically insulated but in addition the insulator should have good thermal conductivity to let the heat flow to the SMA. Finally, is possible to heat the SMA element by using hot air/water to provides the thermal activation.

Huang (2002) proposed the selection of SMAs for actuators based on performance indices. The materials taken into account were three most popular SMAs alloy, namely, NiTi, CuZnAl and CuAlNi. He illustrated the employment of charts according to the heating mode, comparing thus the minimum input power per kg as a function of the electrical resistivity and the thermal conductivity. Figure 1.17 reports the heating and cooling speed charts for electrical resistivity and thermal conductivity.

As regard the heating by means of electrical current, it should be achieved by input current control and input voltage control. As shown in Fig. 1.17a, the input current control requires a material towards the lower right corner of the chart. Thus, material with high electrical resistivity enables lower input current to obtain the same electric power and therefore NiTi alloys are the best compromise.

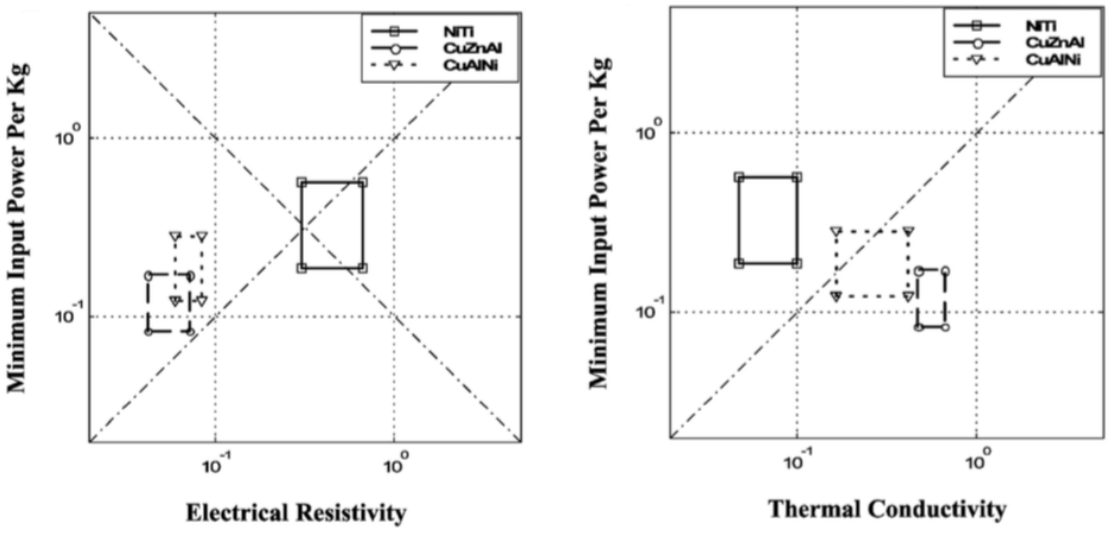

(a) (b)

Figure 1.17 – Heating and cooling speed charts: (a) electrical resistivity vs. minimum input power per kg and (b) thermal conductivity vs. minimum input power per kg (Huang, 2002)

Conversely, input voltage control requires a material with low electrical resistivity which enables to obtain high voltage with low applied current. The latter is related to a material that lies towards the lower left corner of the chart and therefore Cu-based alloys are better than NiTi. On the contrary, in case of heat transfer the heating and cooling speed depends on thermal conductivity and thus CuZnAl alloy is the best to reach high thermal conductivity coupled with minimum input power per kg.

In real cases, by virtue of its high electrical resistivity, work outputs and fatigue lifetimes NiTi alloys are frequently being used in electrical actuators providing a simpler, more compact and less expensive solution compared to conventional devices (e.g. solenoids, servomotors, hydraulics and pneumatic systems). Conversely, thermal actuators are usually made up of both NiTi and Cu-based alloys since their fatigue lifetimes and work output in the first case or higher TTRs and less costs in the second case. In addition, the size and shape of SMA element affects the actuator response time. As a result, actuators with smaller diameter heat faster due to their higher resistivity, and cool faster due to their higher surface-to-volume ratio.

Nonetheless, the cooling process is an aspect of primary importance since the heat energy removal rate is limited by the mechanisms of heat conduction and convection.

To improve the control of both the heating and the cooling processes several strategies were been developed, such as by means of airstream flow, flowing liquids, thermoelectric modules, heat skins and conductive materials.

SMA elements provide an attractive alternative over existing actuation solutions such as electric motors, pneumatics and hydraulics. This is mainly due to some important advantages which are briefly summarised below.

Hirose *et al.* (1989) compared the output/weight ratio as a function of the weight among SMA actuator and conventional motors (e.g. DC/AC motor, motor car, aircraft, hydraulic motor and pneumatic motor). They reported that the output/weight ratio increases as the mass of the actuator increases. Moreover, different type of actuators has specific output/weight ratios and different mass ranges to reach the most efficient performance. The power/weight ratio as a function of the weight is reported in Fig. 1.18. The data suggest that SMA actuators have a potential performance equivalent to that of electric motors in terms of output/weight ratio and in addition, can be designed in very small size. As a result, SMA actuators have the potential capability to achieve an output/weight ratio which can not be realised by traditional actuators.

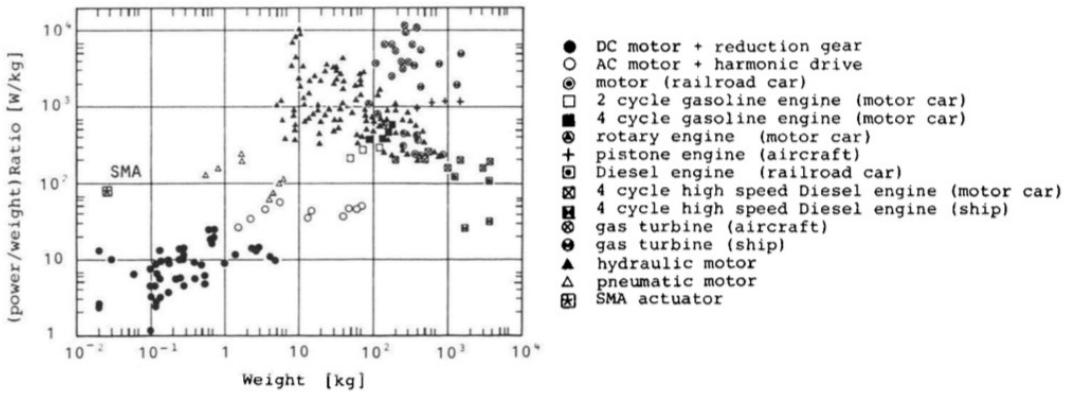

Figure 1.18 – Power/weight ratio vs. wright diagram of actuators (Hirose *et al.*, 1989)

As already mentioned, the simplest type of actuator consists of a SMA spring with a weight on the end. Being driven by the martensitic transformation of the SMA element, the actuation takes place on heating as the spring recover the shape and the weight is lifted up. Subsequently, when the spring is cooled down, the weight stretched it again.

The ongoing employment of SMAs elements as solid-state actuators results from the SME and the unique mechanical characteristics of these materials, including high reversible strain (up to 10 %), high-power to weight ratio and the ability to generate high recoverable stresses (up to 800 MPa) (Tsoi *et al.* 2004, Otsuka *et al.*, 1998). The application of smart materials to devices and control systems characterized by high-energy density and compactness has been of a great interest over the last decade. When a SMA material is intended as an actuation element it should meet the requirements of: (i) large shape memory effect resulting in a long actuator stroke, (ii) high transformation temperatures since the phase transformation should occur at high temperatures like 150 – 200 °C to avoid unwanted activation by warm ambient air and because high transition temperatures also guarantee a complete phase transformation to the martensitic state, (iii) high number of activations and a stable SME and (iv) small hysteresis width between forward and reverse transformations.

The unique characteristics of SMAs make them suitable for innovative applications in many industrial fields like aerospace, automotive, automation, energy, heating and ventilation, safety, security and electronics.

Considering these benefits, the present thesis is aimed at studying the employment of SMAs as element actuator for the development of functional structures and particular attention is given to the development of a SMA-based morphing blade, the following selection of the state of the art and SMAs applications are focused on automotive and aerospace domains. In this context, smart materials and adaptive structure give the chance to realise system with improved performances in comparison with traditional solutions.

Technological progress has ensured the achievement of high efficiency levels as the result of the real-time performance evaluation. The entire control system is therefore optimized, even in nonstationary operating conditions. In this context, shape morphing technology represent a challenging approach to overcome the limits of conventional actuation systems. This is especially noticed in the aerospace domain where the ability to provide shape adaptation to optimally respond to very different operation conditions, even if very far from the nominal design ones, is a key aspect.

A considerable amount of literature considered the potential of morphing applications taking into account aspects related to the variable stiffness concepts as well as the material engineering possibilities (Kuder *et al.*, 2013).

Given that it is not possible to define a configuration able to maximise the aerodynamic efficiency, flow controls for improve aerodynamic performances of adaptive wings is of interest. This solution provides the optimisation of the aircraft performance on changing flight conditions (Stanewsky, 2001). As aerofoils are usually designed for a specific flight condition, the possibility to realise an adaptive structure with the ability to alter its shape continuously to optimally respond to actual operating conditions is of great interest. SMAs cables, beams, torque tubes are used in tailoring geometry and orientations of aerodynamic devices in several aerospace applications.

To this regard, the employment of SMA gives the chance to design structures with improved system performance as in the case of aircraft morphing flaps for enhancing aircraft aerodynamic efficiency.

Many studies have been focused on the investigation of SMAs as linear actuators, to realise reconfigurable aerofoils which enable an increase in the efficiency of the wing in flight at several different flow regimes. Owing to their high recovery forces, large deformations and small volume, SMAs are especially suitable for morphing wings. Examples of morphing structures concerned camber changes, wing cross-section changes and spar changes are widespread. The employment of SMAs as solid state actuators enables to replace conventional devices with more compact, more powerful and less complicated solution. In particular, traditional hinged control surface or lift devices generally lead to a 50 % increase in weight relative to a naked wing (Barbarino *et al.*, 2009). This is because to simplify the actuation chain and deform a limited part of the structure, mobile devices are placed to limited regions and this badly affecting the aerodynamic field in addition to a remarkable increase of the structural weight (Barbarino *et al.*, 2009).

Studies and applications that address to wing morphing technology are widespread in literature and a complete review of the state of the art on morphing aircraft and the related structural shape changing is proposed by Barbarino *et al.* (2011). The authors claimed that wing morphing is a promising technology to realise the wing shape modification for several flight conditions. They made a comparison between different actuation methods showing how advances in smart materials research could enhance the benefits from existing design solutions.

As reported by Melton (1999), the first large scale application of SMA in aeronautic field was a coupling to connect titanium hydraulic tubing on a F-14 aircraft in 1971. Advantages of NiTi couplings for aircraft tubing were, among others, the weight reduction, the easy installation even in difficult access areas and high reliability. Starting from this application, the employment of SMA in aeronautical applications, in particular for aircraft, has increased substantially over recent years. The potential benefits, in both aerodynamic and structural efficiency, can be obtained for example through aircraft morphing wings and rotorcraft smart blades. To this regard, early studies on possible way to control aerofoil shape concerned the embedding or attachment of SMA, in form of wires or tendons, to the wing structure (Pecora and Dimino, 2015). The thermally activated shape recovery enables the proper deflection to modify the camber line of the aerofoil.

Strelec *et al.* (2003) reported a complete analysis, with numerical and experimental approach, of a reconfigurable aerofoil which takes advantage of SMA wires actuators. They assessed the capability of a reconfigurable wing to increase the efficiency at several different flow regimes showing how SMA elements could modify the global shape of an existing aerofoil.

The incorporation of SMA into morphing structures can concern the development of an entire system, as for the wing case, or only focused on a local actuation which is easy to be implemented (e.g. tabs, flaps, engine inlets/nozzles etc.). To this regard, Hutapea *et al.* (2008) proposed the development of an actuation system to control the position of an aircraft's flaps. The smart wing is made up of SMA springs, fixed at the leading edge of the aerofoil. Figure 1.19 reports an image of the smart wing prototype which provide the rotation of the flap in both the upward and downward directions by an upper and lower set of SMA springs which take advantage of the SME, resulting from the applied current.

Even if incorporating SMA elements intro the system structure can be advantageous in terms of space and weight, such control solution leads to non-continuous wing surface which affects the airflow behaviour in the neighbourhood of the profile (Schick *et al.*, 2012).

As reported by Roh *et al.* (2009), the aircraft wing performance could be thus improved by removing discrete control surface and related hinge lines. The authors have numerically compared the

aerodynamic performances of a shape adaptive aerofoil actuated by an SMA film actuator with those of a conventional aerofoil. Figure 1.20 depicts the aerofoil geometries and the related stream lines. By comparing the numerical results, it appears clear that the conventional wing induces flow separation in the flap area; conversely the shape adaptive wing shows more improved aerodynamic performance.

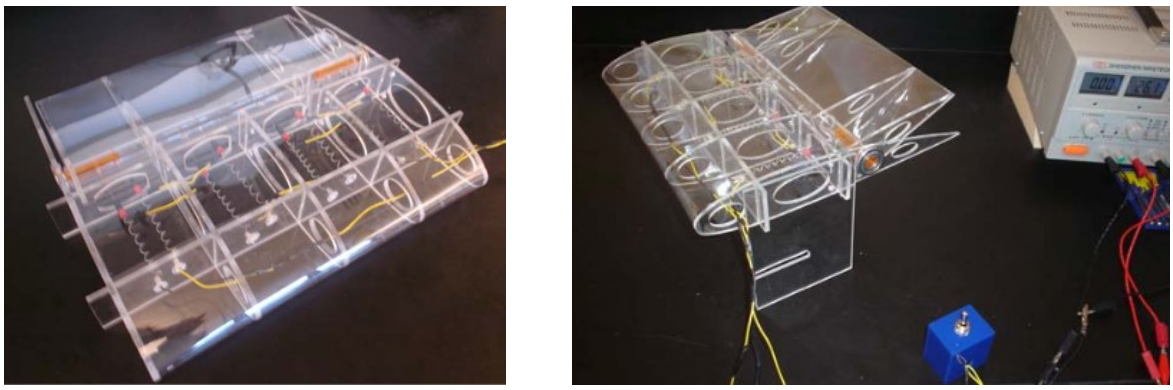

Figure 1.19 – Images of the prototype of the flap (Hutapea *et al.*, 2008)

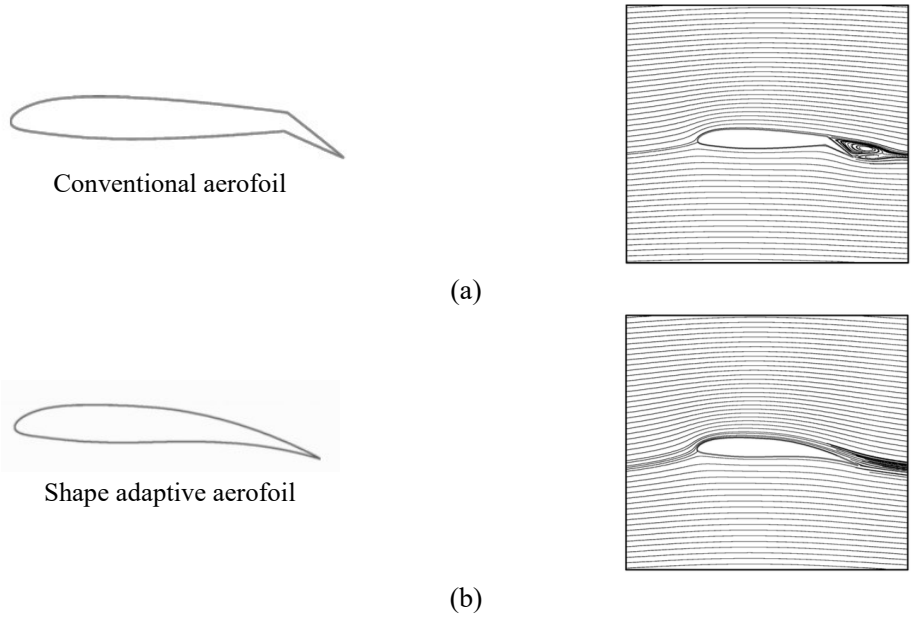

Figure 1.20 – Aerofoils geometries and relative stream lines: (a) conventional aerofoil and (b) shape adaptive aerofoil. Adapted from Roh *et al.*, 2009

Two of the most well-known examples of morphing wings projects are the DARPA Smart Wing program and the Smart Aircraft and Marine Propulsion System (SAMPSON). The first one was intended to develop a continuous wing able to provide the variable twist for the optimisation of the performance during the different flight regimes (Kudva, 2004). In this program, a SMA torque tube was employed to initiate spanwise wing twisting of a scaled-down F-18 wing, as it is reported in the installation image of Fig. 1. 21 (Sanders *et al.*, 2004).

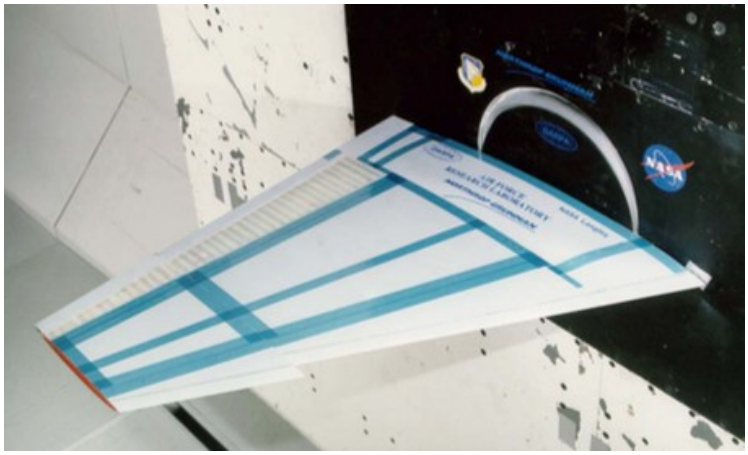

Figure 1.21 – Image of the SMA torque tube installed in the model wing of the DARPA program (Sanders *et al.*, 2004)

Another example of SMAs elements used is aerospace application is for the optimisation of the trade-off between noise mitigation at take-off and landing. To reduce the noise levels flow mixing devices, named chevrons, are installed along the trailing edges. Their configuration can be changed by using SMA beams which take advantage of the changes in flow temperature.
At low altitudes and speeds, with higher engine temperatures, the chevrons fold inward for improved gas mixing and thus lowering noise while, at lower temperatures, they relax to a different configuration to improve engine performance. Hartl *et al.* (2010a) provide an extensive analysis related to the use of a NiTi shape memory alloy for the fabrication of active beams incorporated into a variable geometry chevron. After a complete thermomechanical characterisation of the material, which enables to predict the SMA response, the authors proposed a numerical modelling of the application (Hartl *et. al*, 2010b). The current Boeing design for these variable geometry chevron is reported in Fig. 1.22.

An alternative approach to control the wing shape is to employ an underlying structure with SMA active components, as it is reported by Elzey *et al.* (2003). The authors described the study of a bio-inspired vertebrate structure in which a series of tubular elements are linked together by cylinder and sleeve joints, which enable the relative rotation on actuation. The system comprised this cellular flexible core sandwiched between shape memory alloy sheets whose contraction on heating provide the curvature of the structural actuator. Figure 1.23 shows the shape morphing panel concept, the side view of the control surface in the two different morphed configurations and the span wise twisting (Elzey *et al.*, 2003).

A novel shape morphing wing for small aircraft, capable of large planform and out-of-plane transformations by means of smart materials, was proposed by Sofla *et al.* (2010). To make a reconfigurable aerofoils able to provide an increase in efficiency of the wing in flight at several different flow regimes, they suggested the design of a shape-morphing wing which takes advantage of an antagonistic SMA-actuated flexural structural device that enables the wing profile to change by bending and twisting. Figure 1.24 depicts the light weight SMA actuated beam which is the the spar and ribs of the wing design. As shown, the beam moves a load that exceeds six times of its weight to a distance comparable with the half of the beam span.

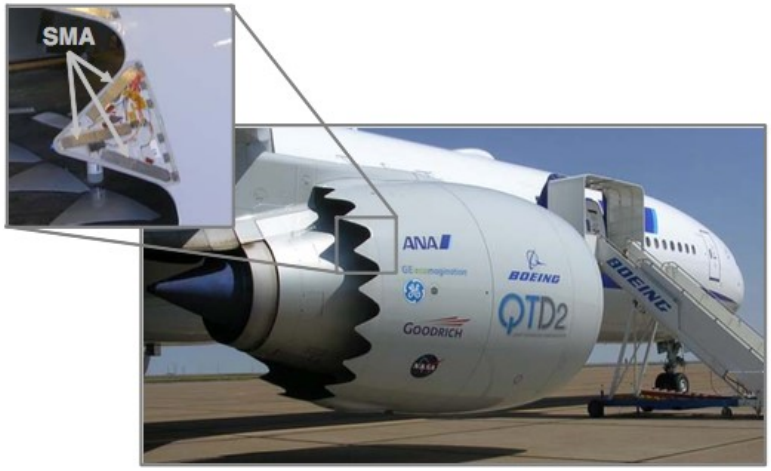

Figure 1.22 – Application of SMA in Boeing variable geometry chevron (Mabe *et al.*, 2006)

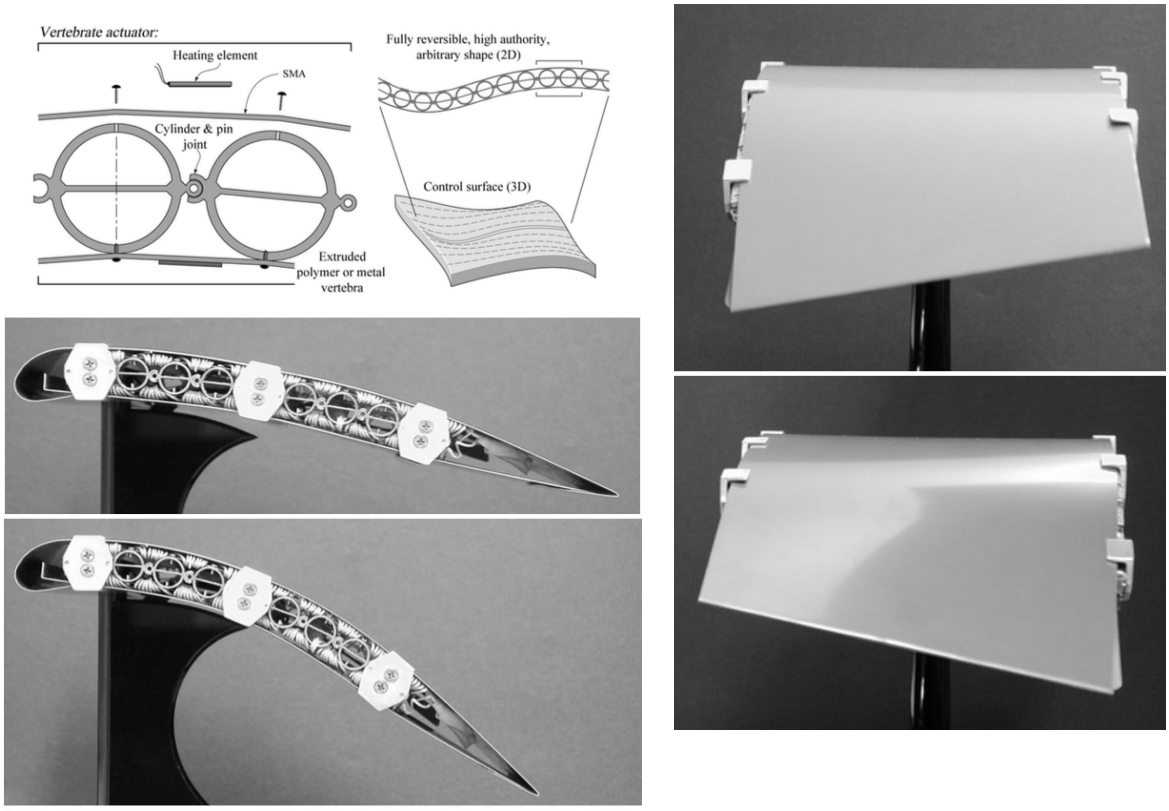

Figure 1.23 – Shape morphing panel concept and views of the control surface on actuation. Adapted from Elzey *et al.*, 2003

Focusing on the employments of SMAs in the automotive field, it should be highlighted that in modern vehicles the numbers of actuators and sensors is particularly high due to the demand for safety, engine controls, driver comfort and better performance. As a result, the numbers of automatic functions (e.g. sensors, actuators, microchips) are highly increased, affecting the weight and volume of the vehicle components.

Figure 1.24 – A light weight SMA actuated truss beam (Sofla *et al.*, 2010)

As reported by Butera *et al.* (2007), more than sixty actuators on a vehicle are activated only by conventional electromagnetic motors. Moreover, in many cases, they are certainly not optimised for weight, volume and reliability. To this regard, SMAs actuators are an attractive alternative to electromagnetic actuators for the development of electro-mechanical devices suitable for a wide range of applications. Within the actuators which could be efficiently replaced by SMAs, the most interesting ones are, among others, rear-view mirror folding, climate control flaps for airflow adjustment, lighting devices, fuel management and lock/latch control systems (Butera, 2008).

In an attempt to provide a general overview of the SMA applications, starting from the selected vehicle parts depicted in Fig. 1.25, the existing SMA actuators are listed in Tab. 1. 1 (Jani *et al.*, 2014). As can be seen, the fields of application are various and SMAs are employed both as thermal actuators and linear actuators. The actuators located on a vehicle can be divided intro: (i) low power actuators for comfort and bodywork functions, (ii) high power control actuators and (iii) high frequency engine control actuators (Butera *et al.*, 2007)

Even if there are many potential applications for SMAs, only few of them have actually been implemented and are technically and economically feasible due to the limited range of TTRs (Jani *et al.*, 2014).

Figure 1.26 provides a general overview of the operating temperature range for automotive applications combined with the TTRs of commercially available SMAs. In fact, most of the actuators are made by using the CuZnAl and the NiTi commercially available alloys. For automotive application NiTi is preferred by virtue of operational temperature range, which lies approximately within the standard range of environmental temperature extremes to which a passenger may be exposed on service, as can be seen from Fig. 1.26. NiTi alloys with TTRs from -50 °C to approximately 110 °C are suitable for repeated cycles within locations of vehicle within this temperature range but not in case of higher temperature (e.g. engine underhood) (Jani *et al.,* 2014, Stoeckel, 1990, Hodgson *et al.*, 1990). SMAs should have an Mf temperature well above the maximum operating temperatures in order to work properly. According to Fig. 1.26 CuAlNi SMAs ternary alloys show TTRs above 200 °C and should be suitable but, unfortunately, they are brittle, unstable and not suitable for multiple cyclic operations (Stoeckel, 1990 and Firstov, 2006).

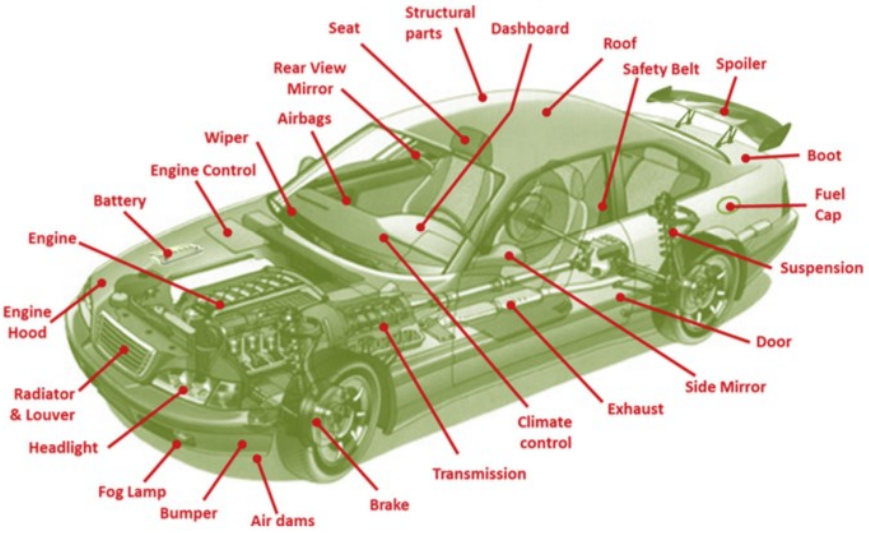

Figure 1.25 – Vehicle parts of SMA applications (Jani *et al.*, 2014)

Table 1.1 – SMA applications in the automotive field. Adapted from Jani et al. (2014)

Vehicle location	*Parts*
Engine room/underhood	radiator, fan clutch, engine control, start-up clutch, tumble flaps, fuel injector and fuel system, piston rings, booster/charger, valves, battery
Drivetrain	transmission control
Suspension/steering/wheel/tyre	brake absorber, tyre
Body/exterior	headlights and lamps, wiper, sunroof and sunshade, door and lock mechanism, side mirror, boot, engine hood, petrol cap, bumpers and crash structures, air dams, grill and louver, spoiler, structural parts and panels
Interior/passenger room	dashboard, rear view mirror, seats, airbags, structural parts and impact structures

As stated above, this thesis accounts on the experimental investigation of the recovery behaviour of SMA strips embedded in a polymeric matrix. Particular attention is given to the development of a SMA-based morphing blade for automotive cooling fan and therefore some aspect related to this specific application are reported below.

The notion of smart advanced blades, which can control themselves and reduce (or eliminate) the need for an active control system, is a highly attractive solution in blade technology. Current systems based on morphing or adaptive blades, beyond aerospace applications, are used in wind turbine

applications, where fast actuation without complicated mechanical systems and large energy-to-weight ratios are required. In such cases, it is important to save in weight and complexity in the rotor design and its auxiliary mechanisms while also reducing the costs of energy generation. In addition, in the gas turbine field, Schetky and Steinetz (1998) proposed an adaptive tip clearance control based on shape memory alloy ring which is shrunk to a predetermined diameter on heating, in order to reducing the tip clearance of a turbine compressor and thus improve the compressor efficiency.

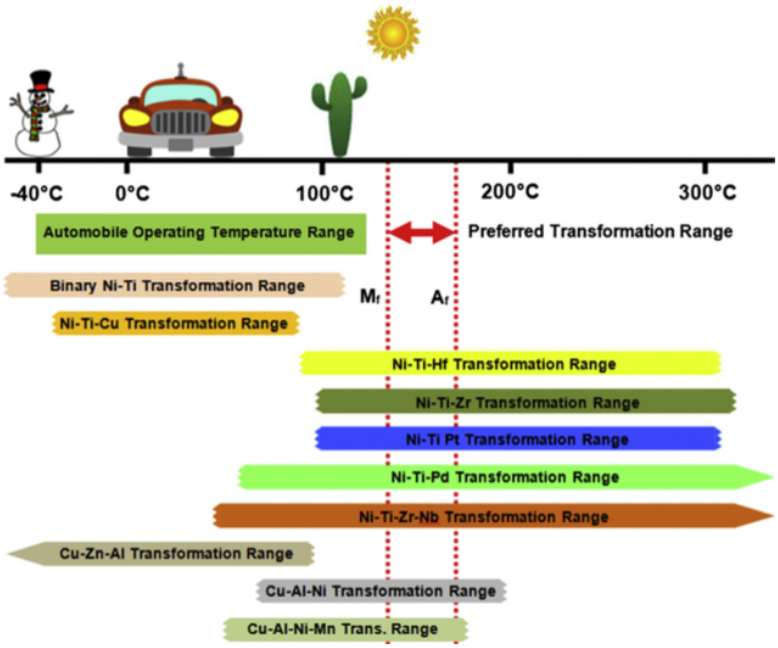

Figure 1.26 – Operating temperature range for automotive application and TTRs of commercially available SMAs (Jani *et al.*, 2014)

With regards to automotive field, it should be noted that the automotive development trend moves toward the increase in engine power and the decrease of under-hood space in favour of driver and passenger compartment space. Besides, the under-air flow has a negative effect on the total drag. The cooling air drag can be as large as 8 % of the total air resistance (Hallqvist, 2008). In support of this, the fan-to-radiator spacing and fan-to-engine spacing play a key role in the cooling circuit performance. The air flow at the front of the vehicle, passes through the grille, condenser, radiator, cooling fan, and other components, removing the rejected heat to the surrounding environment (Baniasadi *et al.*, 2013). The cooling fan operates in a blockage condition due to the upstream radiator and downstream engine, and for these reasons, the axial fan works with a higher radial flow.

Research on possible ways to control the automotive cooling fan has been proposed since the 1970s (Blair, 1974). Cooling fans can be actuated and controlled by a friction-type fan clutch (commonly named on/off clutch) and an air sensing modulated viscous clutch. The on/off clutches were most widespread in the past especially in North America for heavy-duty vehicles. On/off clutches operate by design with the fan either at an idle rotational velocity (typically ± 200 rpm) or at a fully engaged rotational velocity (± 2000 rpm). These types of clutches penalized the power efficiency in providing engine cooling (Elmer *et. al*, 1994). The modulated viscous clutches have a continuous velocity control

that provides the proper cooling air flow rate proportional to engine cooling load by means of a bimetal element (Lee *et. al*, 1998). The bimetal element senses the air temperature approaching the drive from the radiator opening and closing a valve spring to either store the fluid (low fan velocity) or allow full flow to the working area, providing maximum fan velocity. The bimetal element expands and contracts in proportion to the variation in temperature. The two basic benefits derived from the utilisation of fan clutches are reduced horsepower drainage to the fan and a lowering of the average noise output of the fan.

As reported by Elmer *et. al* (1994) the average power consumption of an on/off friction clutch is higher than that of a modulating fan clutch providing the same average cooling rate. A modulating fan clutch theoretically consumes only 22 % of the power of an on/off clutch, providing equivalent average cooling during a duty cycle, which requires on/off fan engagement 20 % of the time. Even if the modulated viscous clutches allow the control of the fan velocities, the proper management of the engine cooling rate and, in particular, of the engine temperature must be realized by linking the coolant engine temperature with the cooling capacity of the fan. The clutches join the engine shaft with the cooling fan which does not follow the engine thermal requests strictly since it is closely connected with the engine rotational velocity, without being affected by the airflow temperature. Also, engine encapsulation increases the retarders that lead to unacceptable time response lag from indirect sensing in new generation vehicles Elmer *et. al* (1994). In fact, in some cases the electric driven fans have replaced the clutch-driven fan and the rotational fan velocity is controlled by some sensors positioned in the cooling circuit Kim *et. al* (2010). This approach improves the engine thermal management but, on the other hand, by using many sensors and devices makes the control system more complicated.

As a result, it appears clear the benefits related to the integration of smart materials in actuation systems. This challenging solution represents an excellent technological opportunity for the development of simple, very compact and reliable actuator devices. Active materials could be integrated into the host structure by means of surface bonding or embedding without affect the mass or the structural stiffness of the device. These structures are thus transformed from static to dynamic or, in some cases, adaptive as they can react directly to environmental stimuli. In a nutshell, smart materials can simplify products, add new functions, upgrade performance, improve reliability and reduce component cost, mechanical complexity and size.

Unfortunately, specific studies on fan performance modification using the SMA devices are limited or even not available in literature. In addition, the variation of the blade shape based on the strain provided by the SMAs is not widely investigated.

Chapter 2

Experimental characterisation of shape memory alloy strips

In this chapter the recovery behaviour of NiTi shape memory alloy strips is reported. The assessment of the shape setting treatment parameters was experimentally investigated by means of recovery tests considering the bending behaviour in terms of curvature evolution with the increasing number of thermal cycles. An experimental and numerical analysis of the two-way shape memory effect, induced by the shape memory cycling, is proposed.

2.1 Introduction

The use of SMA as active elements in composite structures represents a challenging approach for the development of novel types of actuator systems. Given that SMAs are capable of generating high stress and strain, actuators embedded with shape memory alloys materials are of a great interest. Adaptive structures, resulting from the polymeric matrix-SMA coupling, enable to achieve strong actuation forces, due to the SMA elements, combined with large deformation, resulting from the properties of the polymer. Performance of these structures are dependent on the thermal and mechanical behaviour of the polymer-SMA coupling. As a result, the behaviour of the SMA elements as well of the composite structure represents a key aspect for the development of composite structures, characterised by structural simplicity and high power to weight ratio.

The present work is intended at design and testing composite structures in which SMA elements, in form of strip, are embedded into a polymeric matrix. Moreover, the ultimate goal of this work is the development of a morphing blade for an automotive cooling axial fan activated by means of SMA strips. In the light of these considerations, it is clear that prior to the insertion inside the matrix, the strips should be thermally treated to memorise transverse deflections. Upon heating, thanks to the thermally driven phase transformation of the SMA elements, the composite is forced to bend providing the active shape control of the structure. Against this background, the SME behaviour of the strip both in free shape recovery conditions (without any polymeric matrix) and in partially constrained conditions (embedded into the polymeric matrix) are key aspects to be taken into account.

For these reasons, the workflow has concerned (i) characterisation of SMA strips by means of thermal activation cycles in order to study their recovery behaviour as a function of the shape setting treatment, (ii) design and testing of a polymeric structure for the analysis of its adaptive behaviour as a result of the shape recovery of the thermally activated SMA strip and (iii) design and testing of a morphing blade with embedded SMA strips.

The present chapter reports the experimental characterisation of SMA strips during the thermally activated shape recovery tests. With regards to the heating mode, it should be noted that usually, for specimens like wires, the resistive Joule heating is the preferred solution since it provides a convenient mechanism to control the SMA activation. In this case, the electrical power transferred due to resistive heating, is a function of the wire resistance and associated current. As reported by Huang *et al.* (2012), assuming that the electrical power transferred due to resistive heating is converted to heat, it is possible to predict the temperature achieved by the SMA wire, which is a function of associated constants (applied current and time), material parameters and external properties but independent of SMA length. Since response time is a key aspect of the design of SMA actuators and resistive heating is able to provide relative fast actuation, this method is commonly used. Despite that, the complexity system and the relative difficult implementation in some cases are drawbacks of considerable relevance. As a result, the present study has concerned the thermal activation of the strips by means of both an airflow and a fluid flow heating/cooling systems.

2.2 Material characterisation

In this paragraph, the material characterisation performed by means of DSC measurements and tensile tests are described.

Among the commercially available NiTi shape memory alloys, the choice was guided by the need to have the M_f value as close as possible to room temperature. For this reason, the NiTi shape memory alloy (alloy H, supplied by Memry Metalle Company), of nominal composition $Ni_{49.6}Ti_{50.4}$ was chosen. Starting from a plane foil of the as-supplied material, several strips of 107 mm × 8 mm × 0,8 mm in dimension were cut by means of electro-erosion.

In accordance with the ASTM F2004 standard, DSC tests, by TA Instruments DSC Q2000, were carried out on a small fraction of the material in order to evaluate the transformation temperatures ranges. A few thermal cycles at constant heating/cooling rate of 10 °C/min were set. Figure 2.1 reports the DSC thermogram of the alloy whose transformation temperatures and latent heats for both direct and inverse martensitic transformations are summarised in Tab. 2.1. TTRs were evaluated according to the tangential line methods by the intersection between the baseline of the DSC curves and the tangents to the peaks (Lagoudas, 2008).

The mechanical properties of the NiTi material were obtained through uniaxial tensile tests performed at 25 °C and 150 °C respectively under displacement controlled loading conditions. An Instron 4467 testing machine with a 30 kN load cell was used and the loading rate of 1 mm/min was set in order to minimise the self-heating effect due to the transformation latent heat. According to TTRs data, the elastic modulus of the martensite, E_M, the transformation stresses at the onset/end of the martensitic plateau, σ_S and σ_F, and the maximum recoverable strain ε_L were estimated at 25 °C while the elastic modulus of the austenite, E_A, was estimated at 150 °C. These material properties are listed in Tab. 2.2.

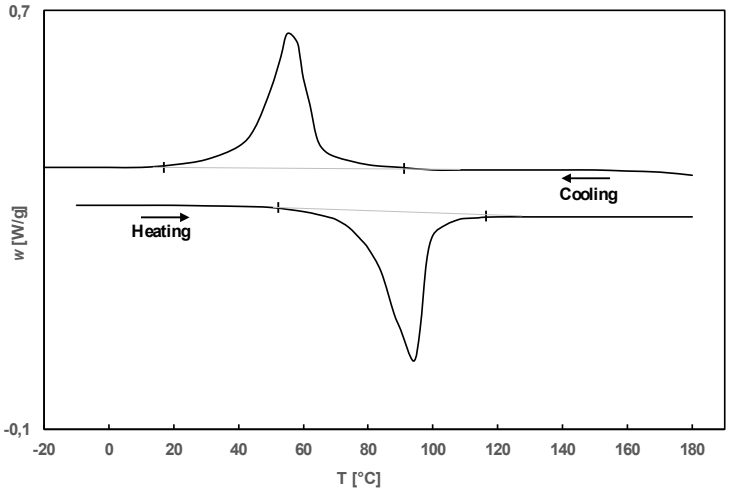

Figure 2.1 – DSC thermogram of the untreated $Ni_{49.6}Ti_{50.4}$ alloy

Table 2.1 – TTRs and latent heats for both direct and inverse martensitic transformation

Austenite start temperature, A_s	82 °C
Austenite finish temperature, A_f	104 °C
Latent heat per unit mass, austenite (ΔH_A)	24,7 J/g
Martensite start temperature, M_s	69 °C
Martensite finish temperature, M_f	46 °C
Latent heat per unit mass, martensite (ΔH_M)	25,3 J/g

Table 2.2 – Material properties obtained by tensile tests

σ_S [MPa]	σ_F [MPa]	ε_L	E_M [MPa]	E_A [MPa]	C_A [MPa/°C]	C_M [MPa/°C]
149	210	0,06	28423	63475	7,25	8,22

2.3 Shape setting and thermal activation tests

As stated above, the strips are intended for the employment as active elements in composite structure and therefore the shape setting treatment and the bending behaviour are the main aspects to be firstly considered.

Given that the aim was to maximise the SME and thus the flexural behaviour of the strip, an experimentally tuned shape setting treatment was developed. This process comprised the study of different shape setting treatments, whose recovery behaviour were evaluated by means of thermal activation tests, described as follows. The forward and reverse martensitic transformations of the NiTi strips were thermally activated, heating through an airstream flow and by cooling through natural convection. The attention was devoted to the influence of the shape setting and to the training process on the evolution of recovery behaviour, which was evaluated in terms of curvature evolution on

increasing the number of cycles and percentage of the recovered shape. To this regard, the quantitative assessment of the curvature evolution was achieved by digital image analyses. Digital camera acquisitions were analysed with a CAD software by interpolating the axis of the strip with a three-point arc to study its curvature.

In order to delete any previous thermomechanical history, the first step of the shape setting treatment comprised the annealing of the material in a tube furnace at 700 °C for 20 min, followed by controlled cooling to room temperature, at a cooling rate of 1 °C/min.

The first set of experimental tests were performed to study the recovery behaviour of a SMA strip which was thermomechanically treated in order to memorise the maximum uniform curvature, according to the dimensions of the strip itself. In particular, the analysis was focused on the curvature evolution on increasing the temperature. In these preliminary tests, the thermal activation was studied by the immersion of the sample in a fluid flow, whose temperature was gradually increased up to above A_f, to ensure the full phase transformation and the shape recovery.

The shape setting had firstly included the pre-strain of the strip at room temperature by applying two bending couples acting at the ends and wounding it on a cylindrical jig to reach the circular shape. In order to prevent the shape recovery during the heating, the strip was constrained into a metal clamp and thermally treated in a tube furnace at 450 °C for 25 min. Finally, the strip was quenched in water at room temperature to memorise the shape. Temperature and time parameters were chosen according to the results reported by Rizzoni *et al*. (2013) which demonstrated that this treatment enables to achieve a high percentage of shape recovery.

At the end of the shape setting, the measured curvature of strip was $\chi_0 = 0{,}057\ mm^{-1}$ which corresponds to the circular shape, after the spring-back.

Subsequently, the evaluation of shape memory effect was studied by thermal activation tests performed in an Ethylene Glycol bath which allowed the temperature to be increased up to 120 °C. To this end, after the shape setting the strip was strained at room temperature, applying a uniform bending load, to reach the flat shape and immerse in the bath into a supporting structure, with one end held in a clamp.

The tests were made up of a thermomechanical cycle comprising for each test:

(i) strain the strip at room temperature ($T< M_f$, martensitic phase) to reach the flat shape;

(ii) heating the strip in the Ethylene Glycol bath at T=120 °C ($T>A_f$, austenitic phase) with a constant cooling rate of 10 °C/min.

The recovery behaviour was assessed by 10 consecutive thermo-mechanical cycles.

During the activation tests the shape recovery was continuously recorded by means of digital image acquisitions, which were synchronised with the temperature evolution of the bath. The latter was measured by means of mineral insulated thermocouples type K place into the Glycol bath, in the neighbourhood of the strip. The values of the curvature of the strip was measured according to the marker points drawn on it, as it is reported in Fig. 2.2 where the digital captures of the strip in the flat shape (non activated condition), Fig. 2.2a, and in the recovered circular shape (activated condition), Fig. 2.2b, are reported.

Figure 2.3 depicts the mean value of the curvature, calculated for the 10 thermal cycles, as a function of the temperature. As can be seen, on heating the curvature of the strip raises up to get closer of the memorised value. Changes in the curvature value are remarkable at about 95 °C and at around 110 °C

the phase transformation could be considered finish since curvature values are almost constant. These experimental findings are consistent with the TTRs extrapolated values from DSC measurements (see Tab. 2.1).

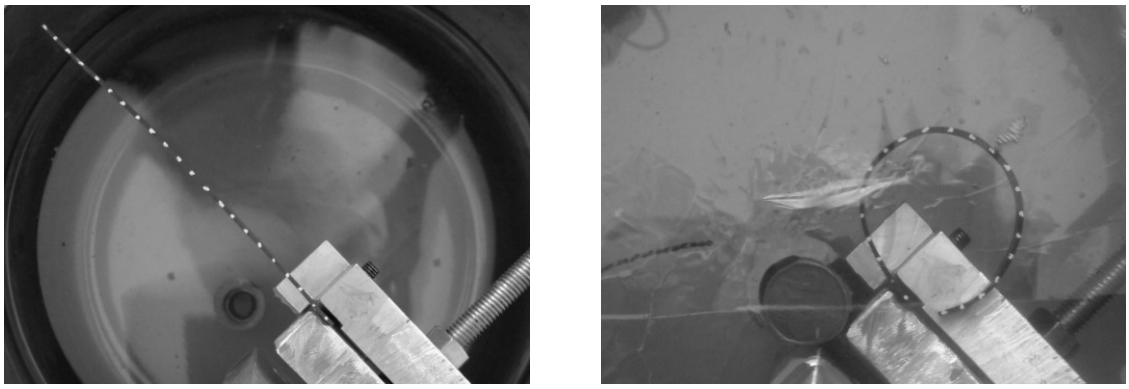

(a) (b)

Figure 2.2 – Digital captures from the recorded video of fluid flow thermal activations: (a) flat shape and (b) recovered shape

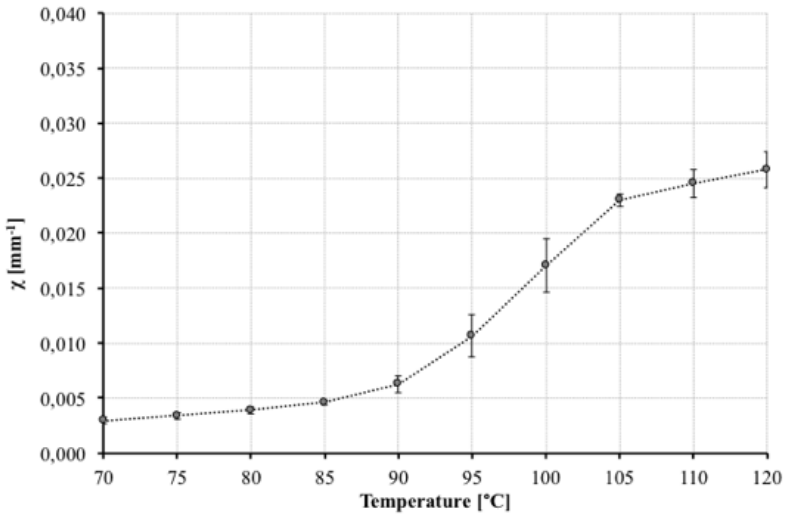

Figure 2.3 – Mean curvature evolution as a function of the temperature during the heating ramp

To study the effect of the thermomechanical cycling, the curvature evolution on increasing the temperature during each thermal cycle was studied and the results are reported in Fig. 2.4. From these data it is evident that, in the first cycle, the strip reaches the maximum curvature which is about 0,035 mm^{-1} at 120 °C and therefore the amnesia is about 39 %. Moreover, on increasing the number of cycles, the shape recovery stabilises to lower curvature values as a result of the deformation to the flat shape (detwinning process) at the start of each recovery cycle. The results presented in Fig. 2.4 suggests that, on increasing the thermal activations, the curvature evolution changes, indicating a progressively decreasing of the starting point of the shape recovery. In addition, focusing on the curvature values obtained at 120 °C (end of the thermal cycle) the decrease of the maximum recoverable curvature is remarkable.

To highlight the decreasing of the curvature achievable by the strip on increasing the number of cycles, Figure 2.5 reports the percentage of shape recovery, calculated as $(\chi_{max} / \chi_0) \times 100$, as a function of the numbers of thermal cycles. χ_{max} is the value of the curvature achieved by the strip at the maximum temperature (120 °C). As can be seen, the percentage of shape recovery quickly decreases and after 10 thermal cycle is about 40 %, suggesting a progressive stabilisation effect of the maximum recoverable curvature.

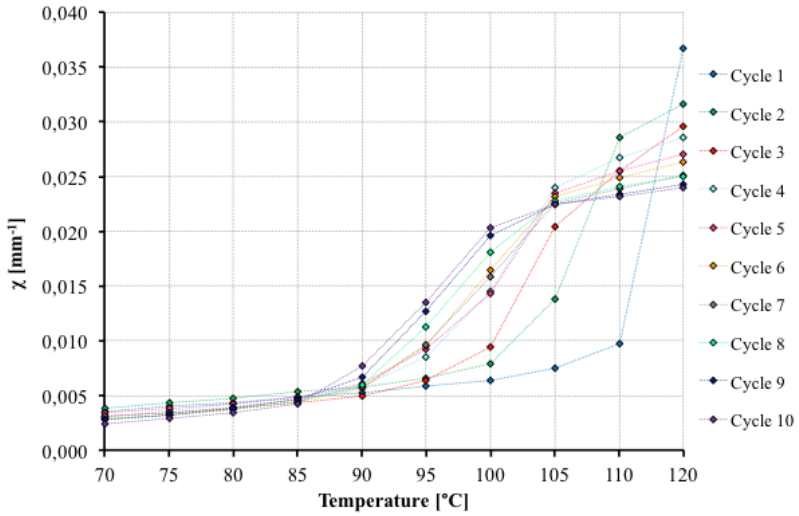

Figure 2.4 – Curvature evolution as a function of the temperature for the 10 thermal cycles

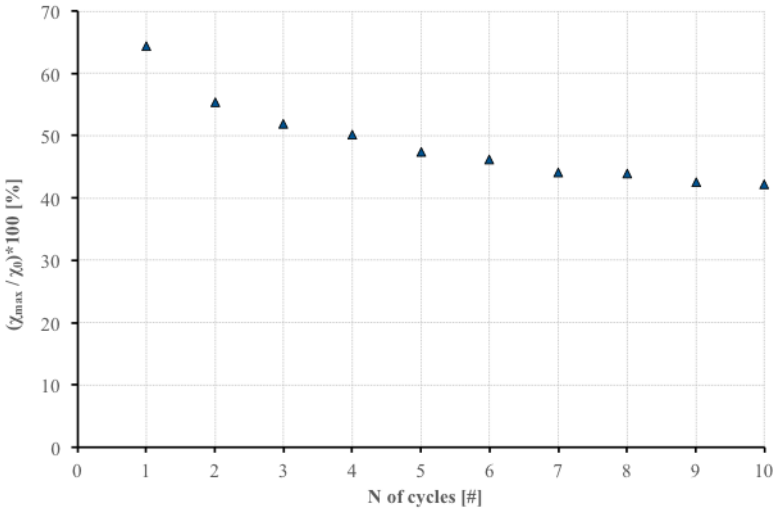

Figure 2.5 – Percentage of shape recovery on increasing the number of cycles: fluid flow activations

Starting from the results obtained in this first set of experiments, it was decided to study the effect of different memorised shapes on the recovery ability of the strip. Aiming at both improving the recovery behaviour in terms of percentage of shape recovery on increasing the number of thermal cycles and maximise the bending behaviour of the strip, the curvature to be memorised was increased.

Thus, starting from a new annealed strip, the shape setting comprised the memorisation of a spiral shape which was achieved according to the aforementioned temperature and time parameters. Figure

2.6 shows a representative scheme of the performed shape setting. As can be seen, the first step comprised the pre-strain at room temperature up to reach a spiral shape as a result of the detwinning of the martensite. In this case as well, in order to prevent the shape recovery during the heating the strip was constrained into a metal clamp and thermally treated in a tube furnace at 450 °C for 25 min. Finally, the strip was quenched in water at room temperature to memorise the shape.

The quantitative evaluation of the curvature was performed by means of digital image analyses according to the marker points drawn on the thickness of the strip (see Fig. 2.6). Since in the present case the curvature was not uniform, the CAD measurements concerned three zone with an almost uniform curvature. In Fig. 2.7 is shown the superimposition of the three arcs of circle and the digital capture with the indication of the three radii of curvature. The three curvature values, at the end of the shape setting and after the spring-back, were $\chi_1 = 0{,}164$ mm^{-1}, $\chi_2 = 0{,}145$ mm^{-1} and $\chi_3 = 0{,}130$ mm^{-1}, respectively.

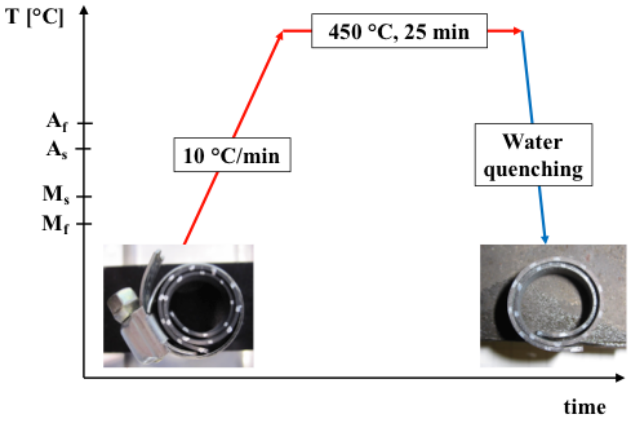

Figure 2.6 – Scheme of the shape setting treatment

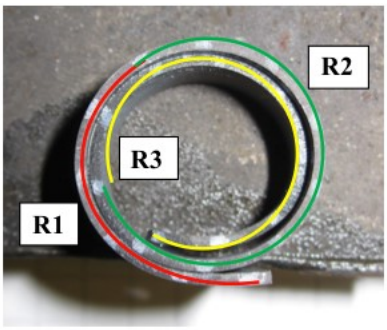

Figure 2.7 – Superimposition between arcs of circle and digital capture

Subsequently to the shape setting, the strip was strained at room temperature, applying a uniform bending load at the ends, to reach the flat shape. The evaluation of shape memory effect was studied by thermal activation tests achieved by an airstream flow realised into a purpose built experimental setup. The latter comprised (i) a heater to provide the heated airflow, (ii) a holder system to clamp the

sample and (iii) a camera for the digital video acquisition. The quantitative assessment of the curvature evolution, according to the increasing temperature on activation, was performed by digital image analyses. The shape changes of the strip were recorded by the video acquisition and the temperature of the strip was measured by welded tip thermocouple type K placed on it.

In order to study the curvature evolution during the complete thermal cycle, the curvature evaluations took into account the curvature values of the strip in its austenitic phase (hot curvature, χ_H) as well as the curvature of the strip in its martensitic phase (cold curvature, χ_C).

Figure 2.8 reports the digital captures of the first recovery cycle for the recovered shape at $T>A_f$ (Fig. 2.8a) and the shape at the end of the thermal cycle at $T<M_f$ (Fig. 2.8b).

As mentioned, the recovery tests were performed though an airstream flow to induce the forward transformation and natural convection provided the reverse transformation. In this case, in fact, the attention was also focused on the shape changes on cooling. To this end, after the shape setting the strip was strained at room temperature applying a uniform bending load to reach the flat shape and fixed on the holder structure with one end held in a clamp.

Training was done according to the following sequence:

(i) strain the strip at room temperature ($T< M_f$, martensitic phase) to reach the flat shape;

(ii) heating the strip by means of an airstream at T=120 °C ($T>A_f$, austenitic phase) with a constant cooling rate of 10 °C/min;

(iii) cooling the strip by natural convection to room temperature ($T<M_f$, martensitic phase).

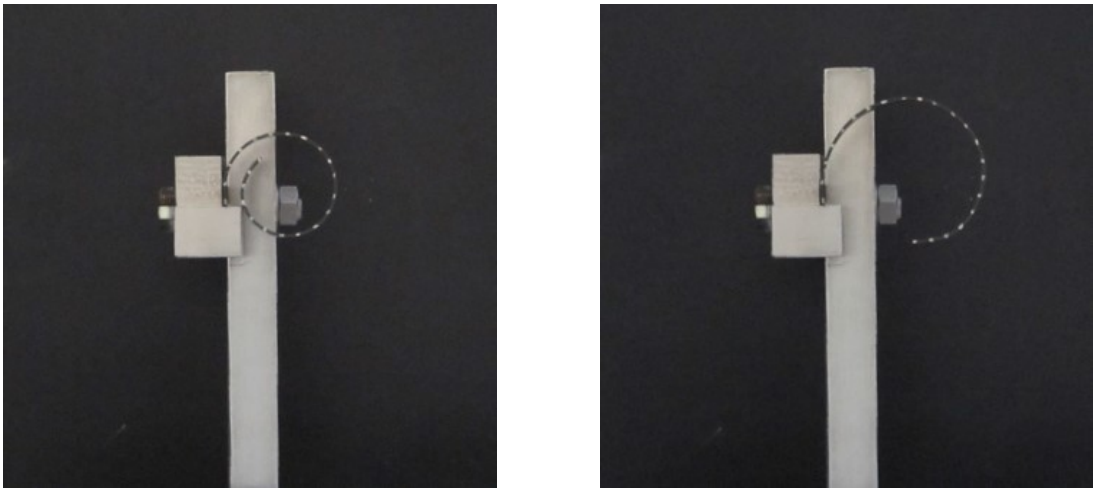

(a) (b)

Figure 2.8 – Digital captures from the recorded video of airflow activations: (a) hot shape and (b) cold shape

Figure 2.9 shows the curvature evolutions on increasing the number of the training cycles for the hot (red dots in Fig. 2.9) and cold (blue dots in Fig. 2.9) shapes. As can be seen from the χ_H experimental data, on increasing the number of cycles the strip shows a progressive loss of the memorised shape which is remarkable in the firsts 15-20 cycles. Despite that, the interesting aspect which emerges from the χ_C trend is that, at the end of the cooling process, the strip decreases its cold curvature values (see blue dots in Fig. 2.9). The reported decrease of the χ_C values demonstrated that, on increasing the number of thermal cycles, the cold shape moves closer to the flat shape. This

experimental finding suggests that the detwinning of the martensite phase, resulting from the strain of the strip to the flat shape, allows the recovery of the cold shape.

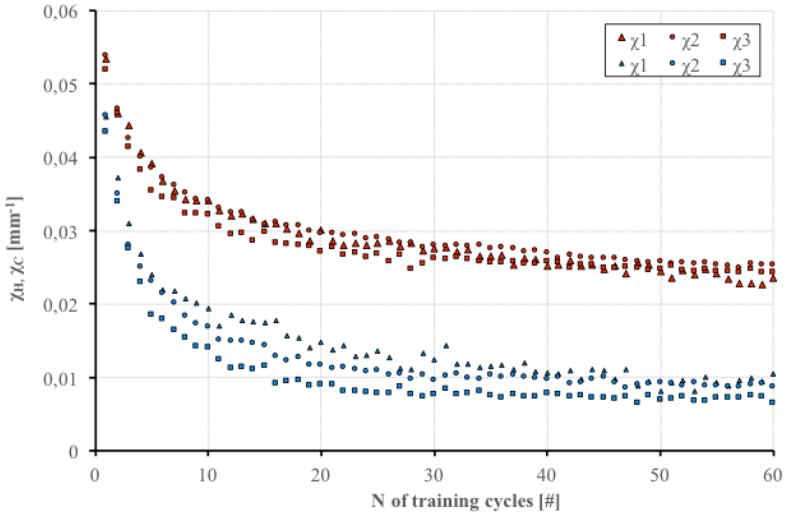

Figure 2.9 – Hot and cold curvatures evolutions as a function of the number of cycles

It should be noted that hot curvature values are comparable for the three considered regions, whereas cold curvatures values appear more scattered. To this regard, the lowest values corresponds to χ_3 which is the zone closer to the free end (χ_1 is the zone close to the clamped end).

With regard to the evolution of the cold curvature values, it should be noted that, among the different thermomechanical cycling methods adopted to induce the TWSME, the shape memory cycling is one of the most effective ones. As reported by Luo *et al.* (2007), this method comprises the repetition of the following four steps for a number of times: (i) cool to below M_f, (ii) load the specimen in martensite state to a desire cold shape, (iii) unload it, (iv) heat it to above A_f. The ability of the material to recover both the hot and the cold shapes, is not an inherent property of the material, but arises from specifically designed thermomechanical treatments that are known as training cycles. It is commonly accepted that these thermomechanical transformations produce a favourable residual stress field and associated anisotropic dislocation structures responsible for the spontaneous shape change upon cooling. As a result, after training, stress-free cooling of austenite produces a transformation strain that is further recovery during stress-free heating of the martensite. It should be noted that, the dislocation structure above mentioned, is often accompanied by a permanent strain that would degrade the memory of the hot shape, as reported by Luo *et al.* (2007). According to the results showed in Fig. 2.9, the deformation in full martensitic state and the consequent progress of dislocation arrangements are linked to the loss of memory for the hot shape with increasing the number of training cycles. As regards the cold curvature and its progressively decrease to the desired cold shape it is likely that in the initial cycles the dislocation arrangements are readily introduced and, due to the greatly increase, the level of memory in the cold shape runs up. As a result, at each cycle the amount of single-variant martensite increases, improving the memory of the cold shape. In other words, this behaviour suggests that the thermomechanical deformation of the strip made possible for the sample to remember both the high and the low temperature shapes. This experimental finding provides an important advantage since the strip is intended to be embedded into a composite structure whose recovery behaviour on cooling

could be improved. In detail, the strip is the active element of the composite whose morphing ability it is not completely demanded to the stiffness of the polymeric compound.

Figure 2.10 reports the plot of the percentage of shape recovery as a function of the numbers of training cycles. The data of Fig. 2.10 suggest that the first activation cycle shows a percentage of shape recovery of about 70 %. This percentage decreases subsequently and, from about the 40th cycle stabilises at around 30 %.

In order to highlight the stabilisation of the TWSME achieved by the detwinning process, Fig. 2.11 reports the difference between the hot and cold shape calculated as $(\chi_H - \chi_C)/ \chi_H$ as a function of the number of training cycles. As expected, the difference between the two shape (hot and cold) initially tend to increase and gradually become almost constant.

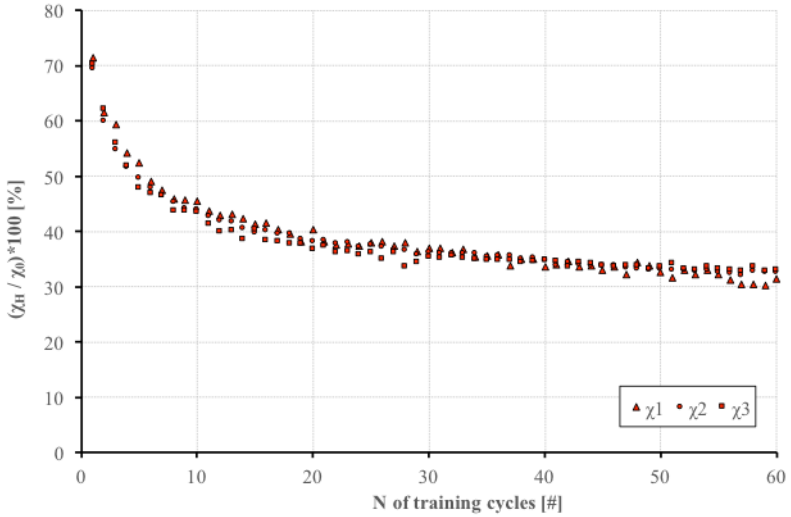

Figure 2.10 – Percentage of shape recovery on increasing the number of cycles: airflow activations

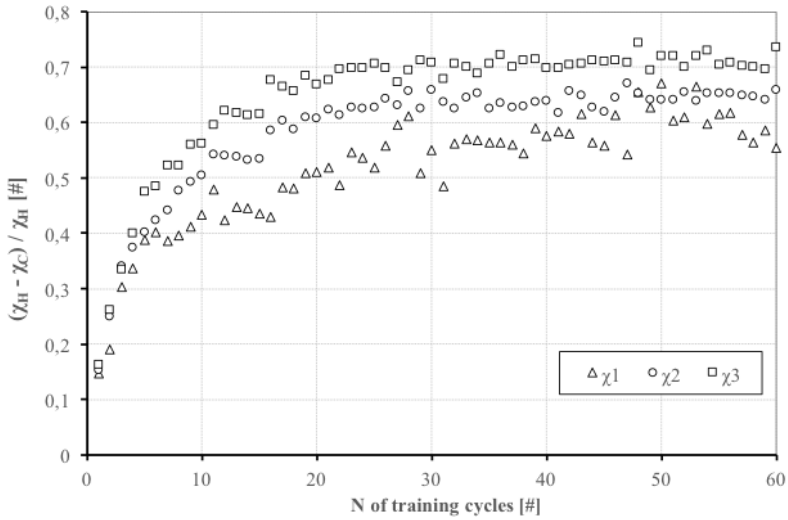

Figure 2.11 – TWSME on increasing the number of training cycles

Given that the memorisation of a spiral shape did not provide a significant increase of the percentage of shape recovery, another annealed strip was considered to be subjected to a double shape setting treatment. In the first shape setting process, it was previously strained at room temperature and wounded on a cylindrical jig to reach a circle shape. This fixture was placed into a tube furnace, heated at 450 °C for 25 min and quenched by water-cooling. Subsequently, the second shape setting provided the straining at room temperature by applying opposite bending couples acting at the ends. The strip was thus locked into a specific metallic holder to be again thermally treated as previous.

The memorised bent shape showed an initial curvature of $\chi_0 = 0{,}024$ mm^{-1}. In this case as well, the recovery was thermally activated by means of an airstream flow and the training sequence was applied to the sample repeating the following steps for 30 cycles:

(i) strain the strip at room temperature ($T < M_f$, martensitic phase) to reach the flat shape;
(ii) heating the strip by means of an airstream flow up to $T > A_f$ (austenitic phase) with a constant cooling rate of 10 °C/min;
(iii) cooling the strip by natural convection to below M_f (martensitic phase).

Figure 2.12 shows the digital captures at the end of the heating phase (Figure 2.12a) and at the end of the cooling to room temperature (Figure 2.12b). In this case as well, CAD curvature measurements, χ_H and χ_C, were achieved by interpolating the marker points with a three-point arc.

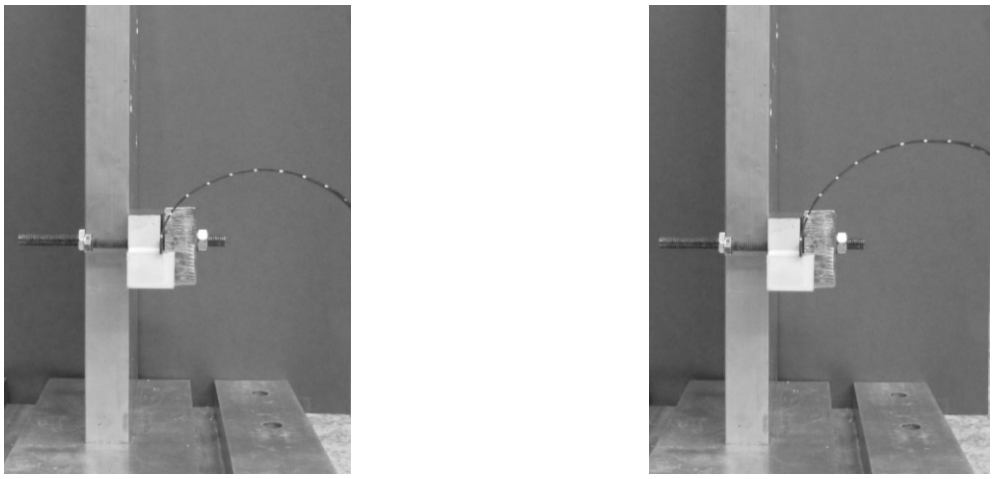

(a) (b)

Figure 2.12 – Digital captures from the recorded video of airflow cycles: (a) hot shape at the end of the heating ramp and (b) cold shape at the end of the cooling ramp

The evolution of hot and cold shapes over the range of the training cycles is reported in Fig. 2.13. The desired hot shape (red line in Fig. 2.13) corresponds to $\chi_0 = 0{,}024$ mm^{-1} of the memorised arc, while the desired cold shape (blue line in Fig. 2.13) corresponds to the flat shape and it is therefore equal to 0. As can be seen, during the training process, the evolution of hot curvature suggests that, apart from the initial cycles where a gradual loss in the memorised shape occurs, the data level off to a value close to 0,015 mm^{-1}. As regard the cold curvature, the trend decreases as the numbers of training cycles increases. As a result, the difference between hot curvature and cold curvature progressively increases, reaching the maximum value of 0,073 mm^{-1} after 30 cycles.

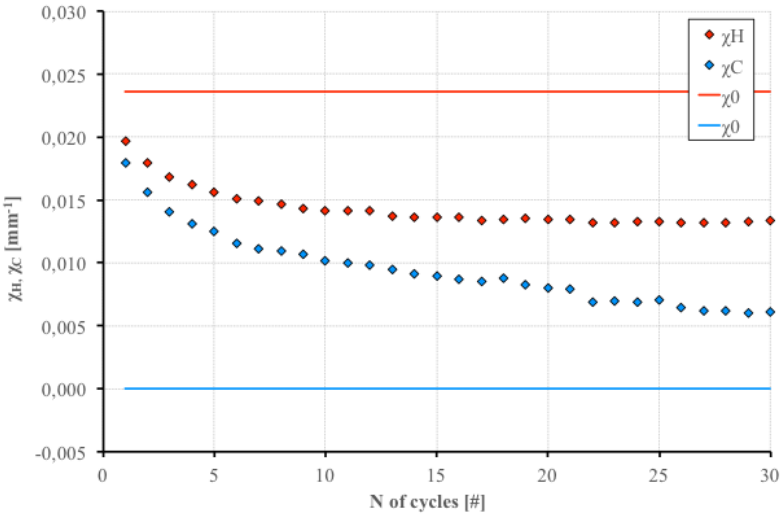

Figure 2.13 – Hot and cold curvatures evolutions as a function of the number of training cycles

The percentage of shape recovery was assessed as $(\chi_H / \chi_0) \times 100$ and its evolution as a function of the numbers of thermal cycles is depicted in Fig.2.14. It can be seen from the data in Fig. 2.14 that for about the first 10 recovery cycles the percentage of shape recovery significantly decreases and then shows an almost steady-state trend with a percentage of shape recovery around at 60 %. From the comparison among the two different shapes considered, it follows that the spiral shape allows a percentage of shape recovery about 30 % (see Fig. 2.10) while the double shape setting provides higher values of percentage of shape recovery (around 55 %) as it is shown in Fig. 2.14.

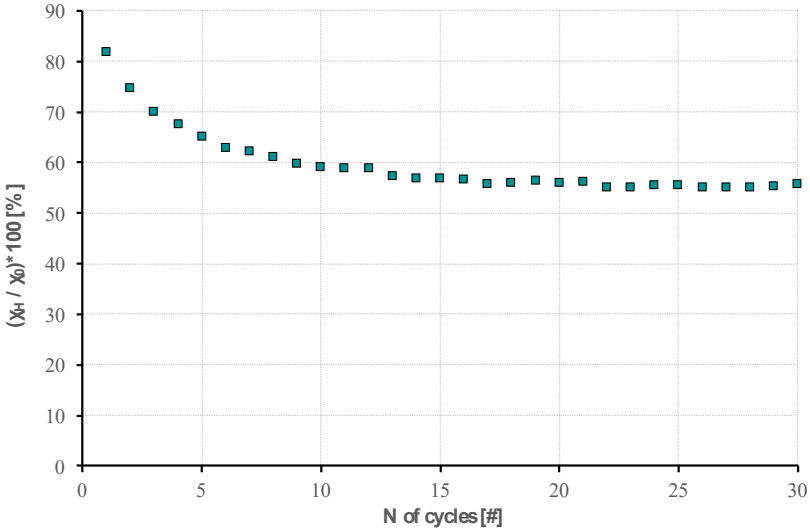

Figure 2.14 – Percentage of shape recovery on increasing the number of training cycles

Moreover, the amount of two-way behaviour, $(\chi_H - \chi_C)/ \chi_H$, as a function of the number of cycles is depicted in Fig. 2.15. In accordance with the results reported in Fig. 2.13, the increase of the two-way behaviour observed in Fig. 2.15 is completely due to the improved cold curvature behaviour, which

gets closer to the desired cold shape, rather than the hot curvature evolution, which is almost steady as the number of cycles increases.

It is well known that there is a limit to the amount of reversible strain that can be achieved in TWSME (Perkins *et al.*, 1990). In particular, the two-way recoverable strain is significantly less than the one-way recoverable strain and it is typically in the neighbourhood of 2 %. The bending deformation strain was calculated as $\varepsilon_{tr} = t/(t+2R_0)$, where t is the radius of the memorised shape. Therefore, the target two-way recoverable strain between the desired hot shape of the arc and the desired cold shape of the straight line, in this case was equal to 0,9 %, less than the threshold of 2 %.

Aiming at assess the observed spontaneous shape change behaviour of the strip as a result of the training cycles describe above, additional 30 stress free thermal cycles were performed on the trained specimen. These activations were achieved by heating at T=120 °C ($T>A_f$) by means of the airstream flow and cooling through natural convection to room temperature ($T<M_f$). The evolution of the curvatures versus the thermal cycles, named TWSME cycles, enables to evaluate the TWSME behaviour achieved by the training process described above.

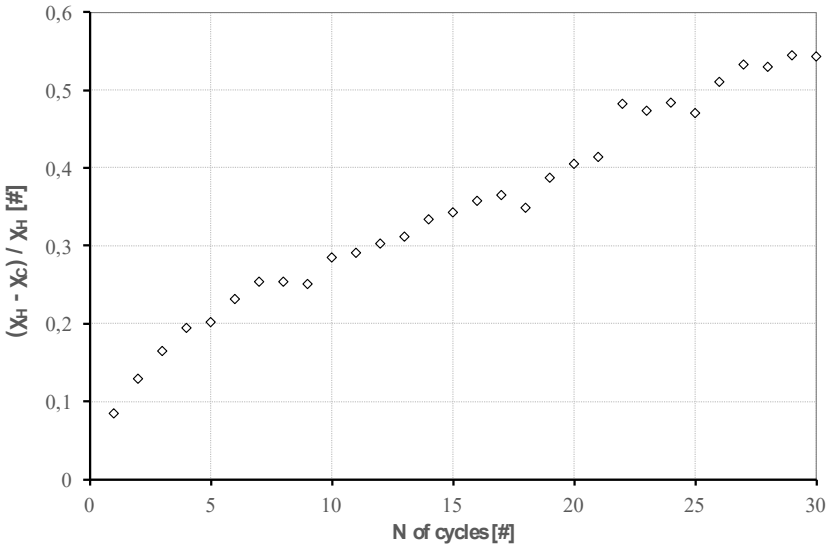

Figure 2.15 – TWSME on increasing the number of training cycles

The results of these TWSME cycles is shown in Fig. 2.16 where the desired hot shape (red line) corresponds to χ_0 = 0,024 mm^{-1} of the memorised arc, while the desired cold shape (blue line) corresponds to the flat shape and it is therefore equal to 0. As can be seen, while the hot curvature has a slightly increase to the desired hot shape, the cold curvature shows a quite constant evolution rather than a decrease to the desired cold shape. The difference between the hot and cold curvature is almost constant with increasing the number of cycles, but this doesn't mean the establishment of the two-way behaviour. It can be pointed out that during the TWSME cycles, where no external stress is applied, the amount of single-variant martensite will decrease and, as a result, the cold behaviour moves away from the desired cold shape.

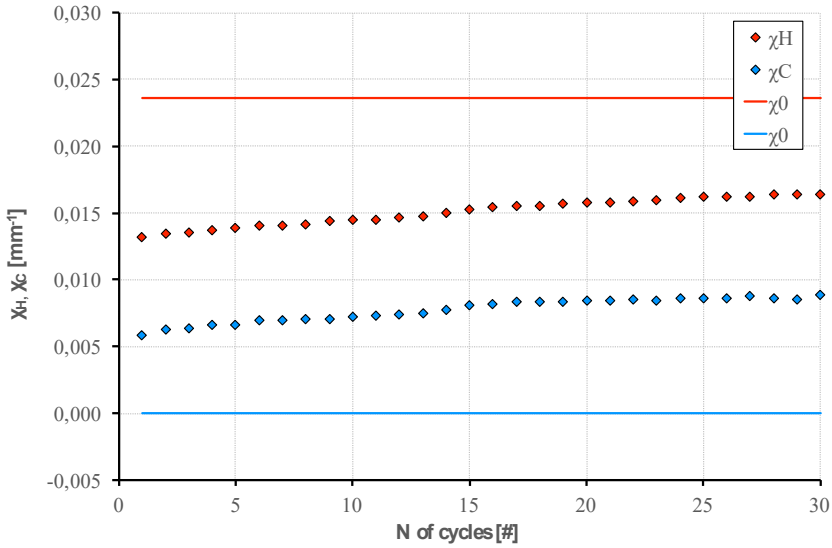

Figure 2.16 – Hot and cold curvatures evolutions as a function of the number of TWSME cycles

2.4 Constitutive modelling

To describe the thermomechanical behaviour of shape memory alloy strips a phenomenological constitutive modelling, whose form and constants in the equations are determined from experiments, is reported herein.

Starting from the results obtained by Rizzoni *et. al* (2013), a one-dimensional phenomenological model, based on stress σ and temperature T as external control variables and on single-variant and multi-variant martensite and austenite volume fractions as internal variables, is proposed. The phase production processes that are considered during bending and free shape recovery under heating are (i) during bending at low temperature, multi-variant martensite transforms into single-variant martensite, (ii) during shape recovery upon heating, both multi-variant and single-variant martensite volume fractions transform to austenite. Each phase production is detailed by kinetic equations describing the evolution of the phase fractions during transformation in terms of the current values of the stress and the temperature. The kinetic equations are assumed to be linear for simplicity and more details can be found in Rizzoni *et. al* (2013).

The stress σ is related to the strain ε via the following constitutive equation (1):

$$\sigma = \begin{cases} E(\varepsilon - \varepsilon_L \xi_s) \; if \; \varepsilon \geq 0, \\ E(\varepsilon + \varepsilon_L \xi_s) \; otherwise. \end{cases} \tag{1}$$

where ε_L>0 is the maximum strain achievable by the transformation of multi-variant into single-variant (detwinning), E is the elastic modulus, assumed to take the same value, 28423 MPa, for all the three phases and ξ_s is the single-variant martensite volume fraction. The behaviour is assumed symmetric in traction and compression.

The first set of bending at low temperature (T<M_f) of the NiTi strip (training cycles, see Fig. 2.13) was modelled as the uniform bending of a beam entirely made of multi-variant martensite. The beam

is taken to be l =107 mm long, and it has the same rectangular cross-section of the NiTi strip, with thickness h = 0.8 mm and width b = 8 mm. Two opposite couples are applied to the ends of the beam, to bend it from the initial memorised curvature χ_0 = 0,024 mm^{-1} to the final curvature reached after elastic springback χ_r = 0,0 mm^{-1}, corresponding to the flat shape.

Using the Euler-Bernoulli theory, it can be shown that during bending single-variant forms initially at the outer and inner fibres of the cross-section and the transformation spreads inside the beam as the value of the applied couples is further increased. The residual stress and single-variant martensite distributions, calculated using the material data listed in Tab. 2.2, are piecewise linear and they are shown in Fig. 2.17 where, for symmetry reasons, only the distributions in the upper half of the cross-section are shown. In the following, λ will denote the distance from the neutral axis to the level at which the residual single-variant fraction ξ_{sr} vanishes.

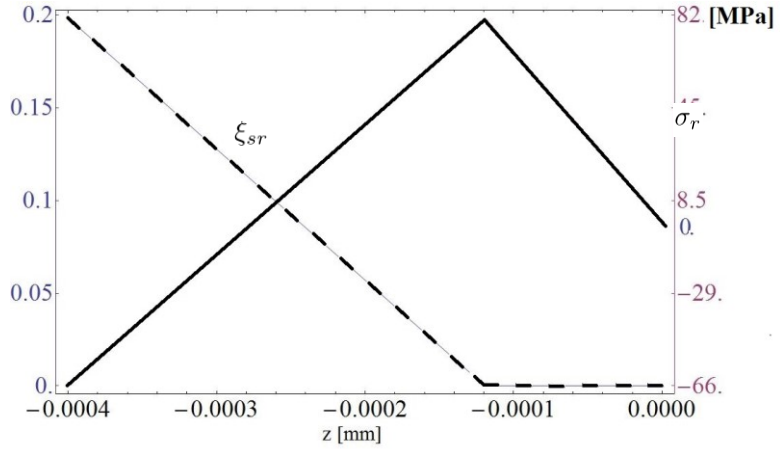

Figure 2.17 – Stress (σ_r) and single-variant martensite (ξ_{sr}) residual distributions after the first bending (ref. 1 of Preface)

For the free shape recovery under heating, a semi-analytical solution is proposed in Rizzoni *et. al* (2013) and here applied. The solution, valid under the assumption of a uniform temperature distribution throughout the cross-section, is based on the existence of transformation fronts, nucleating from the points where the residual stress vanishes and evolving with the temperature. Indeed, the kinetic relations for the transformation of multi and single-variant martensite into austenite impose that points at zero stress transform first. There are two points at which the residual stress vanishes: one is the origin, and the other is calculated at the distance $z_0(A_s)$ = 0,27 mm from the origin. As can be seen from Fig. 2.17, the single-variant martensite is absent at the origin and thus from the origin only a front nucleates, that one for the transformation of the residual multi-variant martensite into austenite. This front is denoted z_m in Fig. 2.18. In Fig. 2.18 z indicates the coordinate along the thickness of the cross-section. At the temperature A_s, single-variant martensite is present only below λ (see Fig. 2.17) and multi-variant martensite is present throughout the cross-section. For temperatures between A_s and T_1, multi-variant martensite transforms into austenite in the region between the origin and the front z_m (dot-dashed line), and both multi-variant and single-variant martensite transform into austenite in the region between the fronts z_+ (dashed line) and z_0 (continuous line). At the temperature T_1, the fronts z_m and z_+ coalesce, thus for $T>T_1$ multi-variant martensite transforms into austenite between the origin and the front z_0 and single-variant martensite transforms into austenite between $z_+(=-\lambda)$ and z_0. From

the point $z_0(A_s)$ two transformation fronts nucleate, denoted z_+ and z_0 in Fig. 2.18, which shows the evolution of the fronts with the temperature calculated using the material data listed in Tab. 2.2. In the region between z_+ and z_0, both multi- and single-variant martensite transform into austenite. At the temperature T_1 = 90,4 °C, the fronts z_m and z_+ coalesce, thus for $T>T_1$ multi-variant martensite transforms into austenite between the origin and the front z_0, and single-variant martensite transforms into austenite between $z_+(= -\lambda)$ and z_0. At $T = A_f$, the transformation of both martensite variants into austenite finishes and the beam recovers its original (memorised) curvature χ_0.

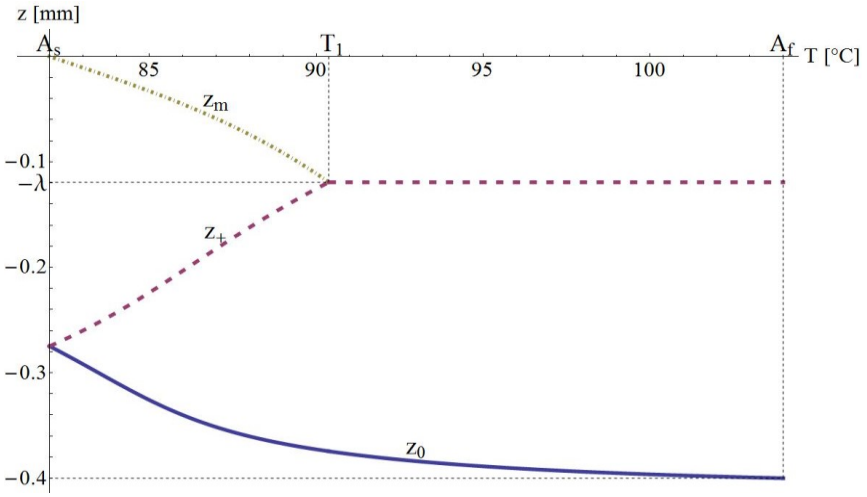

Figure 2.18 – Calculated evolution of the phase transformation fronts with the temperature (ref. 1 of Preface)

As the fronts evolve, the curvature of the beam also evolves along the continuous curve plotted in Fig. 2.19. Correspondingly, the single-variant martensite fraction and stress distributions also change inside the cross-section and Fig. 2.20 shows the calculated evolutions. The details for calculating the curves shown in Fig. 2.18, Fig. 2.19 and Fig. 2.20 are given in Rizzoni *et. al* (2013).

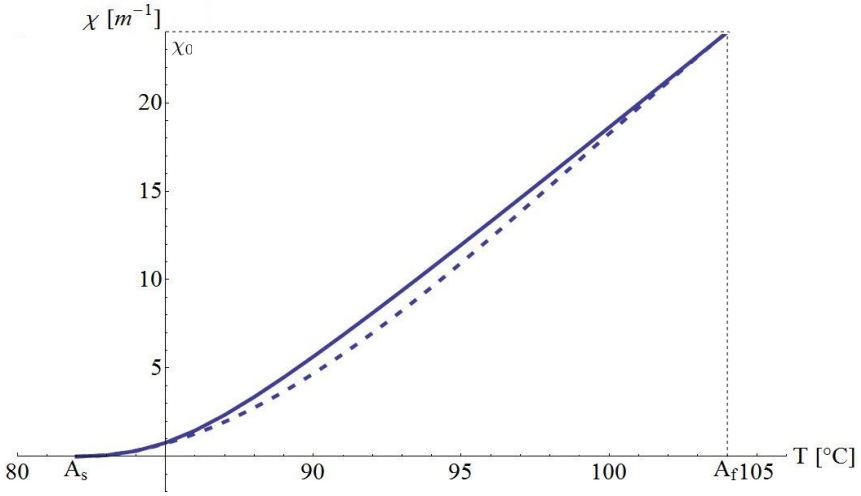

Figure 2.19 – Calculated curvature evolution (continuous line) and its cubic approximation based on equation (3) (dashed line) for the first free recovery upon heating (ref. 1 of Preface)

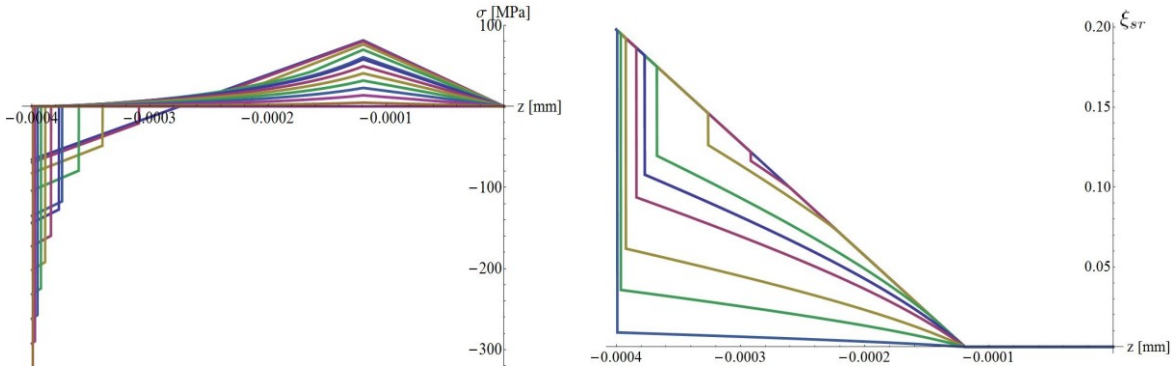

(a) (b)

Figure 2.20 – Calculated evolution of the stress distribution (a) and of the single-variant martensite fraction distribution (b) in the upper-half of the cross-section for the first free recovery upon heating (ref. 1 of Preface)

The front z also described in the solution proposed by Rizzoni *et. al* (2013) and corresponding to the transformation of the martensite in the compressed part of the cross-section, does not exists here because, given the material parameters listed in Tab. 2.2, it would violate the activation conditions of the kinetic laws. Indeed, one has:

$$\frac{C_A(A_f - A_s)}{E\mathcal{E}_L\xi_{sr}(-h/2)} < \frac{\lambda(\chi_0 - \chi_r)}{\epsilon_L\,\xi_{sr}(-h/2) - (\chi_0 - \chi_r)(h/2 - \lambda)} \tag{2}$$

which implies that the phase transformation occurs only in traction. If condition (2) applies, then the evolution of the front z_0 displayed in Fig. 2.18 suggests an asymptotic behaviour of the function $T \longrightarrow \chi(T)$ near A_f. The expression for z_0 is:

$$z_0(T) = \frac{\xi_{sr}(-h/2)\,\lambda\, f(T)\mathcal{E}_L}{(\chi_0 - \chi(T))(h/2 - \lambda) - \varepsilon_L\, f(T)\xi_{sr}(-h/2)} \tag{3}$$

where $f(T)=(A_f-T)/(A_f-A_s)$, and $\xi_{sr}(-h/2)=0{,}2$ is the value taken by the single-variant martensite distribution at the point $z=-h/2$ at the end of the uniform bending at low temperature ($\xi_{sr}(-h/2)=0{,}2$ for the parameters listed in Tab. 2.2, see Fig. 2.17). Thus, assuming that $z_0 \sim -h/2$ as $T \longrightarrow A_f$ and using (3), one obtains the following asymptotic behaviour of $\chi(T)$ near A_f:

$$\chi(T) \approx \chi_0 - \frac{2}{h}\,\varepsilon_L \frac{(A_f - T)}{(A_f - A_s)}\xi_{sr}(-h/2) \tag{4}$$

According to (4) it is possible to approximate the curvature evolution with a cubic curve having minimum at $T=A_s$ (and the minimum value is χ_r) passing through the point (A_f, χ_0) and having tangent line at $T=A_f$. For the material parameters of the alloy taken into account, the result turns out to be in acceptable agreement with the exact curvature evolution in almost all the range of temperatures (A_s,

A_f), as shown in Fig. 2.19. It should be noted that only the first free recovery upon heating has been considered, and the results have been obtained under the assumption that the beam recovers completely its original curvature χ_0 at T=A_f. However, the experimental data described in the previous sections indicates that this does not occur, and that the curvature recovered at the end of heating decreases with the number of cycles. This could be attributed to the presence of residual martensite in the parent phase at macroscopic free stress state, due to accumulation of plastic dislocations as it has been experimental reported by Saint-Sulpice *et al.* (2009) who gave the evidence of residual strain due to accumulated martensite.

To phenomenologically describe the accumulation of martensite, on the assumption that $\xi_{sr}(-h/2)$ depends upon the number n of cycles as follows:

$$\xi_{sr}(-h/2;\mathrm{n}) = (1 - e^{(1-\mathrm{n}/\mathrm{n}_0)})\xi_\infty + \xi_0 \tag{5}$$

where ξ_0= 0.2 is the value calculated for the first cycle, n_0 and ξ_∞ are two material parameters. Substituting (5) into (4) gives an equation for the curvature evolution near A_f with the number of cycles. Figure 2.21 shows the plot of the curvature at T= 101 °C as a function of n obtained with the following values of the material parameters: n_0 =4,75 and ξ_∞= 0,32. These values have been chosen so as to fit the experimental data at high temperature as close as possible.

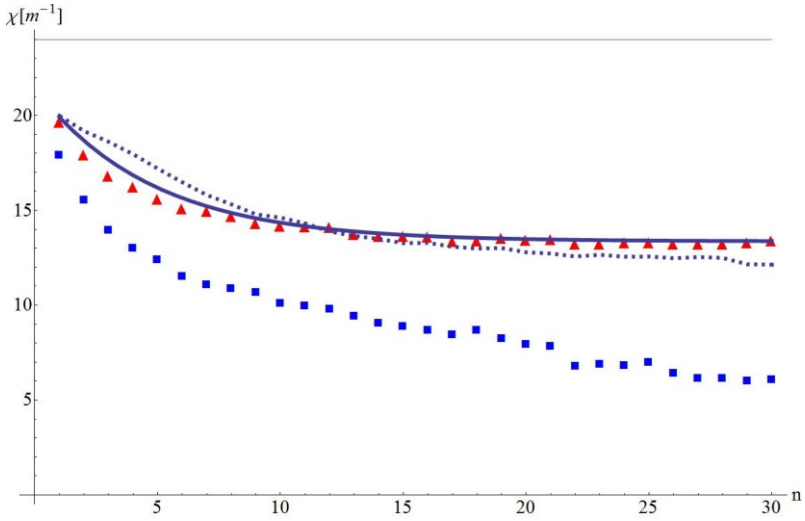

Figure 2.21 – Evolution of the recovered curvature with the number of cycles (ref. 1 of Preface)

In Fig. 2.21 the triangles represent the recovered curvatures measured at high temperature, the squares refer to the recovered curvatures measured at low temperature after cooling and the continuous line is related to the theoretical evolution based upon the phenomenological assumption reported in (5). Figure 2.21 reports also the numerical results obtained using the model proposed by Auricchio *et al.* (2003), which is adopted to reproduce the experimental data during the training and in particular, the evolution of the curvature at high temperature during the cycles (dotted line in Fig. 2.21). As can be seen, the comparison between the experimental data and the simulated evolution based on the model shows a good agreement between simulation and experimental findings.

Chapter 3

Bending behaviour of a functional structure embedded with a shape memory alloy strip

In this chapter the development and experimental tests of a functional structure obtained by embedding a NiTi shape memory alloy strip in a glass reinforced polyamide structure is described. Thermal activations were achieved by a fluid flow provided by an experimental setup realised on purpose.

3.1 Shape control of composite structures

Active shape memory alloys elements allow for the fabrication of functional structures in which they are directly or indirectly embedded in a polymeric matrix, realising what is called Shape Memory Composites (SMCs), since they comprise at least one shape memory material. Traditionally, active composite structures are realised by surrounding pre-strained SMA wires with an elastic matrix, which is usually a thermoplastic or thermosetting material (Janocha, 2007). On heating, typically by passing an electric current through the shape memory material, its martensitic phase is transformed into austenite and the resulting macroscopic shape change enables the composite to be activated. Conversely, on cooling the austenite transforms back to martensite and the composite structure returns to its original shape.

As stated above, with regard to the activation method, electric heating is the preferred solution. Despite that, the shape control of deflections via modification of the electric input (voltage or current) is not always as feasible as it might seem, due to the associate heat transfer issues (Giurgiutiu *et al*., 1997). Moreover, even if wire is the most commonly used form of SMAs, also strip shape is an attractive solution. To this regard, it should be highlighted that using SMA strip leads to increased cross-sectional area which reflects on higher actuating force but requires higher heating and cooling times on activation. For these reasons, the shape control of incorporated SMA elements into polymeric

structures required the study of heating and cooling systems which better meet the technical requirements.

In answer to this problem, the present chapter addresses to the design, developments and experimental characterisation of a functional structure obtained by embedding a single NiTi strip into a polymeric structure designed on purpose. The construction of a such structure enables to evaluate the bending ability of the SMA strip in partially constrained conditions which is responsible for the morphing of the SMC. Since the electrical heating of the SMA strip is associated with system complexity and the cooling phase is dependent upon the natural convention, a thermally driven actuation was considered herein. To this end, the shape control was achieved by means of fluid flow which provided the heating and cooling of the composite structure.

3.2 Experimental setup

In order to test the SMC by means of fluid flow, an experimental apparatus was designed and realised on purpose. Starting from the need to continuously provide the fluid flow for the forward and reverse martensitic transformations of the strip, the first task was dedicated to the design of the thermo-hydraulic system. The basic concept was the development of two hydraulic circuits, one for the hot and one for the cold fluid flow, managed by an electric board.

To this end, the test bench was equipped with two shelves: the upper one was the measurement zone while the lower was devoted to the housing of (i) hot circuit and relating heating device, (ii) cold circuit and relating cooling device and (iii) electric board. Figure 3.1 shows an image of the entire test bench with its electric board.

As for the measurement zone, it was made up of protective PMMA transparent panels in which were housed (i) the solenoid valves for the control of the fluid flow, (ii) a vent valve to vent the air from the circuit, (iii) flexible hydraulic lines for connection with the test apparatus, (iv) a digital camera for the video acquisition and (v) two pressure gauges. To control and acquire the temperature of the fluid, mineral insulated thermocouples were located in the circuit by means of adjustable compression fittings. Figure 3.2 reports an image of the connection and devices placed in the measurement zone with an indication of the elements included.

Figure 3.1 – Digital image of the test bench

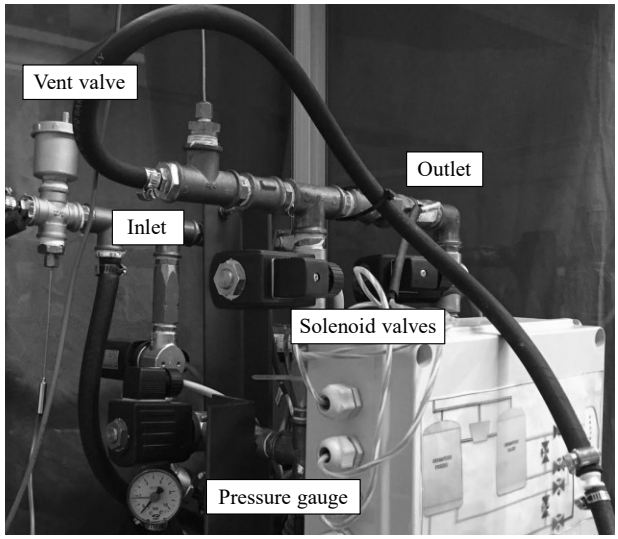

Figure 3.2 – Digital image of the measurement zone and related components

The hydraulic circuit related to the hot fluid comprised an insulated tank with a capacity of 30 l equipped with an electrical resistance (230 V and 1500 W of electric heater power) managed by a digital mechanical thermostat to set the temperature. Similarly, the hydraulic circuit responsible for the cold part, included a refrigerating unit with a capacity of 45 l, power at 230 V with an electric power of 600 W and equipped with a setting wheel for the cooling rate. This unit was connected to an insulated tank with a capacity of 30 l for the storage of the cold fluid. These two hydraulic circuits represent a pressurised sealed circuit, with a pressure load of 2 bar.

The operating fluid is an aqueous solution of Propylene Glycol (67 % in volume) which is handled by two recirculation pumps, located downstream of the hot and cold tanks, respectively. The employment of this type of operating fluid enables the regulation of the hot and cold fluid temperature in a wide range, given that the Propylene Glycol leads to an increase of the boiling point and a decrease of the freezing point of the solution.

As stated above, the test bench was equipped with an electric board to command and control the entire system, by ensuring the manual on/off switching of the system as well as of each device. In detail, on the front panel were located (i) the power button, (ii) the emergency stop button, (iii) the start/stop buttons, (iv) the thermostat related to the hot circuit and (v) the power switches for the heating and cooling devices. An image of the front panel of the electric board is depicted in Fig. 3.3.

For the system management several data acquisition modules were located inside the electric board. The devices were controlled by a dedicated software, realised in a Labview programming environment, whereby the operations of command, control and acquisition of the variables related to the system status were managed. In particular, from the main screen it is possible to control the system status (temperature and operating mode) as well as to switching on/off each device (switching on/off the pumps and the solenoid valves).

Figure 3.4 reports an example of the experimental temperature trends as a function of time of a thermal cycle which comprising (i) a heating ramp, (ii) a phase at the maximum temperature for a defined period of time and (iii) a cooling ramp to reach the target temperature. In addition to the temperature of the fluid flow at the inlet and outlet sections described above, Fig. 3.4 shows also the

temperature trend of the air inside the measurement zone, acquired by means of a welded tip thermocouple type K placed in the neighbourhood of the composite structure.

Figure 3.3 – Digital image of the electric board

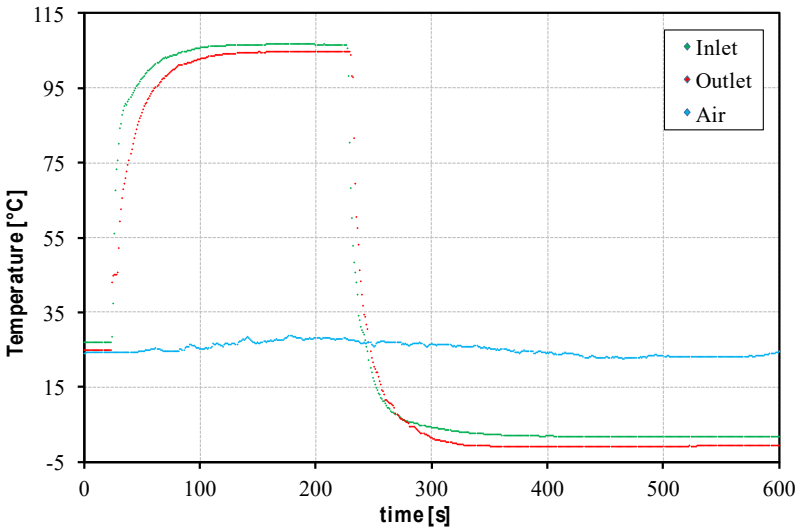

Figure 3.4 – Thermal performance evolution of the fluid flow

3.3 Functional structure design

Given that the thermally activation was entrusted to the heat transfer from the fluid flow to the SMA strip, the first task was the design of the functional structure section.

As described in Chapter 2, the strip of 107 mm × 8 mm × 0,8 mm in dimension, was a NiTi shape memory alloy (alloy H, supplied by Memry Metalle Company) of nominal composition $Ni_{49.6}Ti_{50.4}$.

Aiming at reducing the activation time and the stiffness of the system, the strip was embedded in the polymeric structure and located in direct contact with the fluid flow. Figure 3.5 shows the CAD

geometry of the cross section of the functional structure where the grey zone represents the polymeric matrix while the red one is the strip. As can be seen from Fig. 3.5, the strip was placed at half the cross section height and parallel to the longitudinal axis of the SMC, held by two specifically designed guides realised in the polymeric matrix. This housing performs multiple functions since (i) the strip ensures the bending of the functional structure on actuation, (ii) the strip represents a separating wall for the circulation of the fluid flow and (iii) the strip can slip without constrain due to the friction with the polymer.

In order to achieve an easier and proper introduction of the strip in the SMC, two openings were placed in correspondence to the front and rear section, as it is visible in Fig. 3.6. Moreover, to allow the fixing of the SMC during the activation tests, 4 holes having a diameter of 5 mm were placed in the polymeric structure (see Fig. 3.6).

The functional structure was then equipped with the inlet and outlet hose ends for the connection with the flexible hydraulic lines of the test apparatus, as it is depicted in the section reported in Fig. 3.7. As can be seen, the SMC comprises internal pipes for the fluid flow circulation to provide direct contact with the SMA strip. To ensure the water seal two components were placed in the front and rear section (see the blue parts in Fig. 3.7).

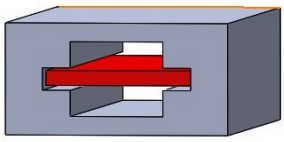

Figure 3.5 – CAD geometry of the functional structure at the cross section view: strip arrangement

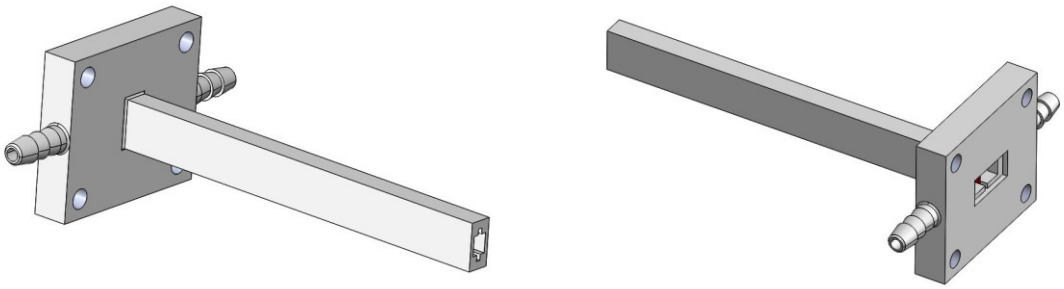

(a) (b)

Figure 3.6 – CAD geometry of the functional structure: (a) isometric front view and (b) isometric rear view

As for the polymeric compound the choice was guided by the need to be realised by rapid prototyping technique and, according to the good mechanical properties and high softening temperature, the SMC was realised in a glass fibre reinforced Nylon PA66 containing 30 % glass reinforcement. Some of the mechanical and thermal properties of the polymeric compound are reported in Tab. 3.1.

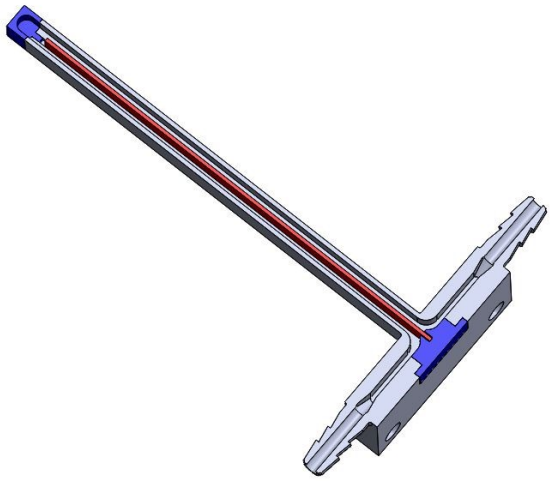

Figure 3.7 – CAD geometry: longitudinal section view

Table 3.1 – Properties of the polymeric compound

Tensile modulus [GPa]	3,30
Flexural modulus [GPa]	2,90
Density [g/cm^3]	0,84

3.4 Thermal activations

Given that the aim of the experimental tests was to study the bending deflection of the SMC by the thermally driven phase transformations of the SMA strip, according to the results reported in Chapter 2 in terms of percentage of shape recovery, the annealed strip was subjected to the double shape setting treatment. Starting from a bent shape with an initial curvature of $\chi_0 = 0{,}024$ mm^{-1}, the strip was strained at room temperature to reach the flat shape and was thus embedded in the functional structure.

The activations were performed by the test bench described above repeating the following steps for 15 cycles to evaluate its bending behaviour:

(i) heating the SMC by means of a hot fluid flow, whose temperature was set to 110 °C in the hot insulated tank;
(ii) heating for 4 min (the target temperature was reached after about 90 s);
(iii) cooling the SMC by means of a cold fluid flow, whose temperature was set to -1 °C in the cold insulated tank.

To evaluate the temperature of both the polymeric structure and the SMA strip, two welded tip thermocouples type K were placed (i) on the external surface of the SMC, named polymer and (ii) inside the inlet internal pipe in correspondence of the strip, named SMA, respectively. Figure 3.8 reports the temperature trends measured during a thermal cycle, comprising the heating, the maintenance phase and the cooling ramp. As can be seen from Fig. 3.8, the experimental apparatus enabled to reach uniform thermal conditions during the thermal cycle. It should be noted that, this configuration leads to reach a maximum temperature on the strip of about 100 °C.

The morphing properties of the SMC were studied by subjecting it to a heating/cooling process and monitoring its adaptive behaviour by means of digital video acquisitions, which were synchronised with the temperature evolution to link the shape evolution with the temperature changes.

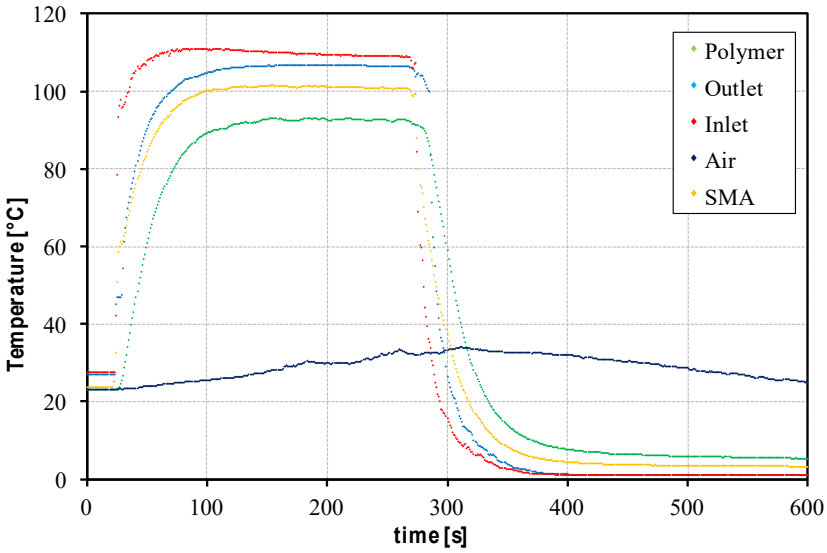

Figure 3.8 – Temperature trends during thermal activation by means of fluid flow

Figure 3.9 shows the digital captures, from the recorded video for the 1st activation cycle, of the SMC in the non activated condition (Fig. 3.9a) and in the activated condition (at the end of the heating ramp which corresponds to the maximum deflection) (Fig. 3.9b). As can be seen from Fig. 3.9, the shape modification provided by the thermally activated phase transformation of the SMA strip enabled the deflection of the SMC. It should be pointed out that the first thermal cycle corresponded to the first thermal cycle of the polymeric matrix and of the SMA strip.

To quantitatively evaluate it, CAD measurements were performed by interpolating the marker points with a three-point arc and measuring the beam deflection.

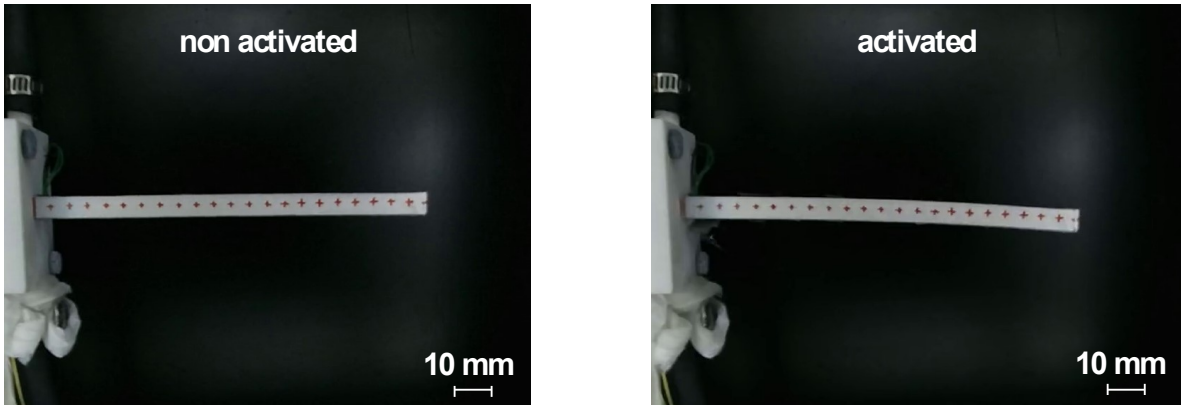

(a) (b)

Figure 3.9 – Digital captures from the recorded video of the SMC fluid flow activation: (a) non activated condition and (b) activated condition

The evolution of the deflections achieved by the SMC over the range of the 15 thermal activations is reported in Fig. 3.10. These values are (i) the maximum deflection measured at the end of the maintenance phase when both the SMA strip and the polymeric matrix reached the thermal uniformity (red dots in Fig. 3.10) and (ii) the residual deflection measured at the end of the cooling ramp (blue dots in Fig. 3.10). As can be seen from Fig. 3.10, on increasing the number of cycles the maximum deflection decreases, in accordance with the results reported above for the thermal activation tests performed with the strip without the polymeric compound (see Chapter 2, Paragraph 2.3). In addition, the residual deflection shows a slightly increase during the firsts cycles and then the value stabilises at around 2 mm.

With regard to the percentage of shape recovery, according to Chapter 2, it was calculated as (χ_H / χ_0) ×100 where χ_H represents the curvature of the SMC calculated by means of a three point arc at the end of the maintenance phase (χ_H is the curvature corresponding to the maximum deflection). It was found to be about 2,9 % which is significantly lower to the one obtained with the strip without the polymeric compound. These experimental findings are likely to be related to the temperature of the strip which is not high enough to ensure the complete phase transformation.

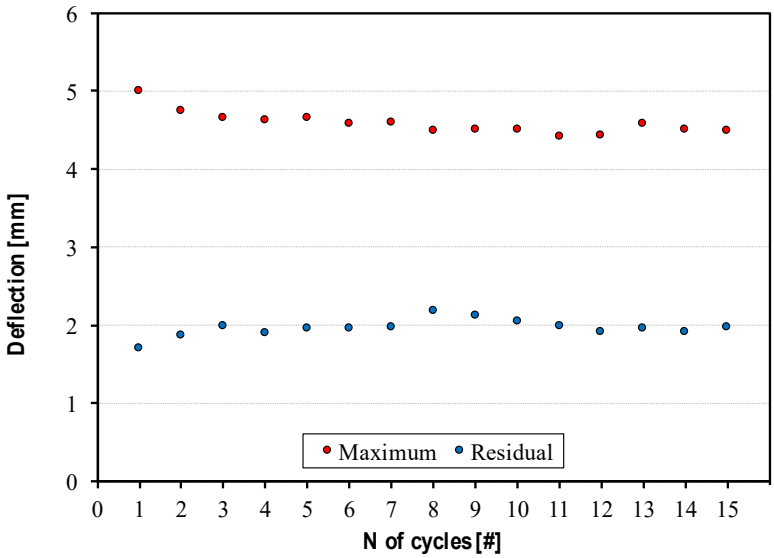

Figure 3.10 – Deflection of the SMC as a function of the number of thermal cycles: fluid flow activation

Aiming at evaluating the assumed thermal limit, additional activation tests were conducted by means of an airstream flow obtained in the experimental apparatus described in Chapter 2, wherein an airflow cooling device system was added to provide the cold airflow.

Therefore, thermal cycles were performed on an additional functional structure, identical to the previous one and containing another SMA strip thermally treated as the former. In this case as well, the first thermal cycle corresponded to the first thermal cycle of the polymeric matrix and of the SMA strip.

The activations were performed by repeating the following steps for 15 cycles to evaluate its bending behaviour:

(i) heating the SMC by means of hot airstream flow;
(ii) heating for 6,5 min;
(iii) cooling the SMC by means of a cold airstream flow.

Figure 3.11 reports the temperature trends during a thermal cycle measured by means of the welded tip thermocouples placed on the polymeric structure, named polymer and on the SMA strip, named SMA. As can be seen, this experimental apparatus enables to obtain higher temperature on both the polymer and the strip.

In this case as well, the morphing properties were studied by means of a digital video acquisitions, which were synchronised with the temperature evolution to link the shape evolution with the temperature changes.

Figure 3.12 shows the digital captures, from the recorded video for the 1st activation cycle, of the SMC in the non activated condition (Fig. 3.12a) and in the activated condition (at the end of the heating ramp which corresponds to the maximum deflection) (Fig. 3.12b). As can be seen from Fig. 3.12, the shape modification provided by the airstream flow enabled a greater deflection of the SMC compared to the activations performed by fluid flow. Also in this case, CAD measurements were performed by interpolating the marker points with a three-point arc and measuring the beam deflection.

As can be seen from Fig. 3.12, the shape modification provided by the airstream flow enabled a greater deflection of the SMC compared to the activations performed by fluid flow. Also in this case, CAD measurements were performed by interpolating the marker points with a three-point arc and measuring the beam deflection.

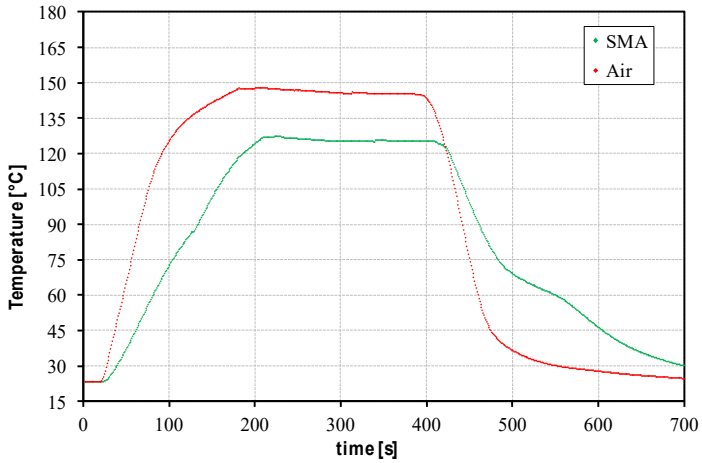

Figure 3.11 – Temperature trends during thermal activation by means of airstream flow

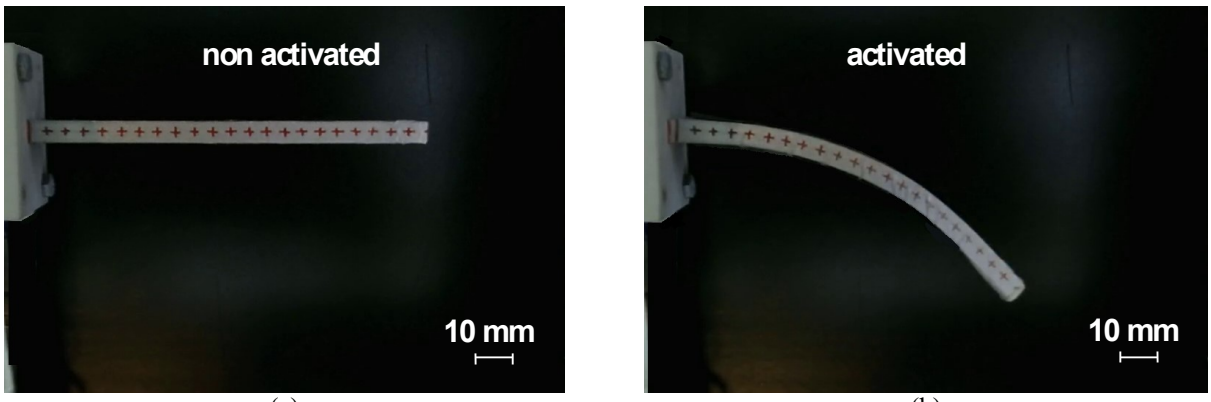

(a) (b)

Figure 3.12 – Digital captures from the recorded video of the SMC airstream flow activation: (a) non activated condition and (b) activated condition

The evolution of the deflections achieved by the SMC over the range of the 15 thermal activations is reported in Fig. 3.13 where the red dots represents the maximum deflection and the blue dots the residual deflection.

Also in the present case, the SMC did not recover all the deformation and a residual deflection of about 33 mm is present. Moreover, as can be seen from Fig. 3.13, the maximum deflections achieved by means of airflow are much higher to those obtained with the fluid flow activations. To this regard it should be noted that in this case, it is likely that the higher temperatures reached allowed a major deflection of the SMC. It could be argued that these results are related to the behaviour of the SMA strip but also the behaviour of the polymeric matrix. In particular, the higher temperature of the strip enables a greater amount of volume fraction of martensite which is converted to austenite. Moreover, during the activations by means of airstream flow, the temperature of the polymeric structure is much higher and therefore this might affect its stiffness thus the resulting deflection values.

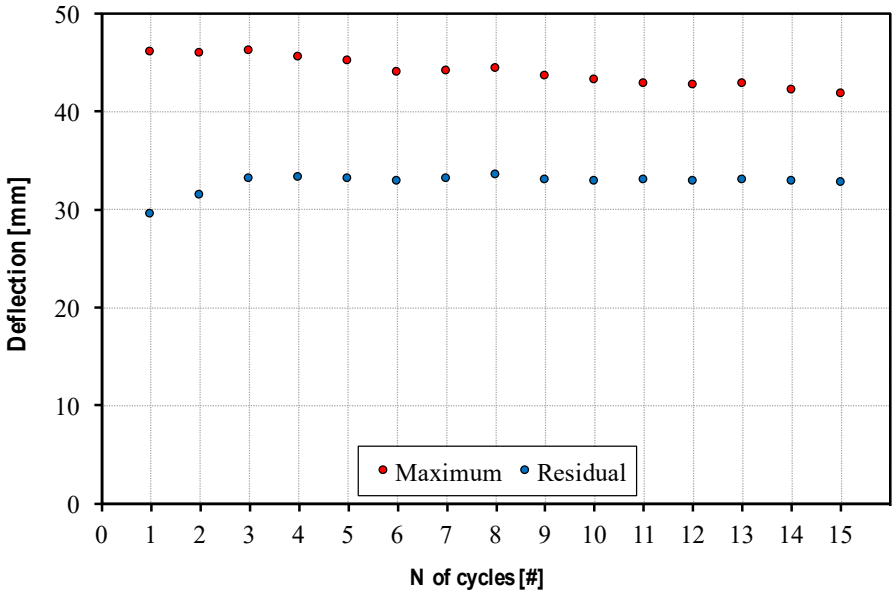

Figure 3.13 – Deflection of the SMC as a function of the number of thermal cycles: airstream flow activation

Aiming at evaluate the assumed issues related to the TTRs of the considered strip, a set of experimental tests was thus conducted by using another strip, with the same geometry, but different chemical composition and lower value of the A_f temperature. To this end, a commercially available NiTi material (alloy M, supplied by Memry Metalle Company) of nominal composition $Ni_{49.8}Ti_{50.2}$ was taken into account.

Also in this case, DSC tests, by TA Instruments DSC Q2000, were carried out on a small fraction of the material in order to evaluate the transformation temperatures ranges. A few thermal cycles at constant heating/cooling rate of 10 °C/min were set. Figure 3.14 reports the DSC thermogram of the alloy whose transformation temperatures and latent heats for both direct and inverse martensitic transformations are summarised in Tab. 3.2. TTRs were evaluated according to the tangential line methods by the intersection between the baseline of the DSC curves and the tangents to the peaks (Lagoudas, 2008).

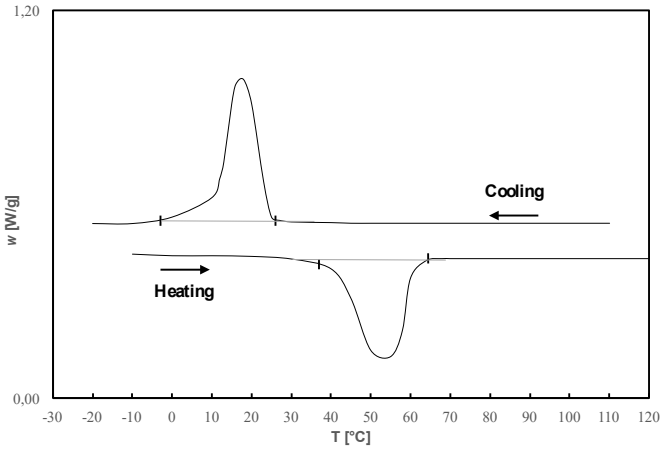

Figure 3.14 – DSC thermogram of the untreated $Ni_{49,8}Ti_{50,2}$ alloy

Table 3.2 – TTRs and latent heats for both direct and inverse martensitic transformation

Austenite start temperature, A_s	38 °C
Austenite finish temperature, A_f	63 °C
Latent heat per unit mass, austenite (ΔH_A)	25,3 J/g
Martensite start temperature, M_s	20 °C
Martensite finish temperature, M_f	-8 °C
Latent heat per unit mass, martensite (ΔH_M)	25,8 J/g

The activations were performed by fluid flow provided by the test bench described above and repeating the following steps for 15 cycles:

(i) heating the SMC by means of a hot fluid flow, whose temperature was set to 110 °C in the hot insulated tank;
(ii) heating for 1,5 min;
(iii) cooling the SMC by means of a cold fluid flow, whose temperature was set to -1 °C in the cold insulated tank.

Figure 3.15 shows the digital captures, from the recorded video for the 1st activation cycle, of the SMC in the non activated condition (Fig. 3.15a) and in the activated condition (at the end of the heating ramp which corresponds to the maximum deflection) (Fig. 3.15b). As it is shown, the thermally activated phase transformations of the SMA strip enabled the deflection of the SMC up to values comparable to those obtain with alloy H, thermally activated by means of airstream flow, as it is reported in the deflection measurements in Fig. 3.16. It should be also noted that alloy M enabled to reach a greater shape recovery on cooling as shown by the data of the residual deflections.

These results suggest that both the maximum and the residual deflections are dependent on both the behaviour of the strip and of the polymeric compound.

In order to study the evolution of the SMC deflection as a function of the temperature during activation, Fig. 3.17 reports the analysis conducted for the 15th thermal cycle. In detail, Fig. 3.17 reports the evolution of the deflection during the heating ramp (filled dots) and during the subsequently cooling ramp (empty dots). On heating, changes in the deflection values are remarkable at about 55 °C. These

results revealing the morphing properties of the SMC in term of progressively deflection during both the heating and the cooling ramp.

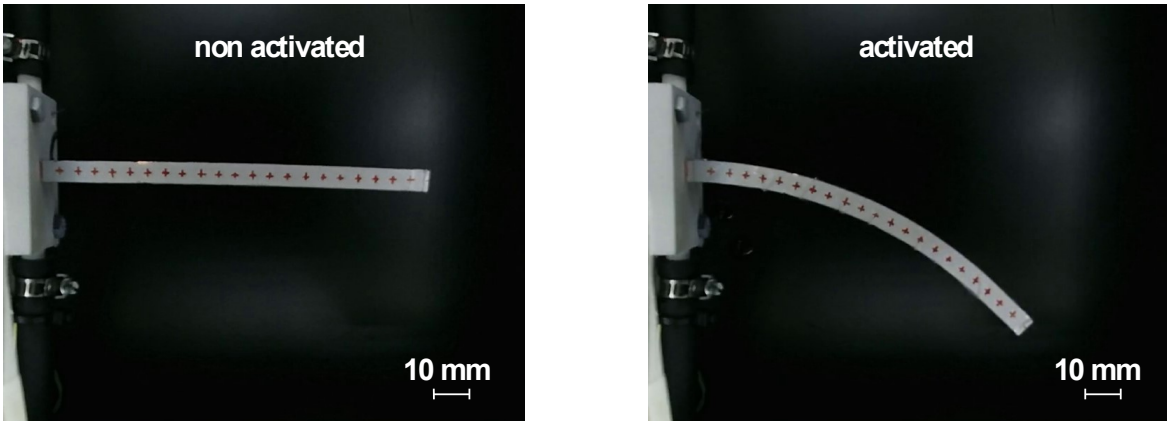

(a) (b)

Figure 3.15 – Digital captures from the recorded video of the $Ni_{49,8}Ti_{50,2}$ SMC fluid flow activation: (a) non activated condition and (b) activated condition

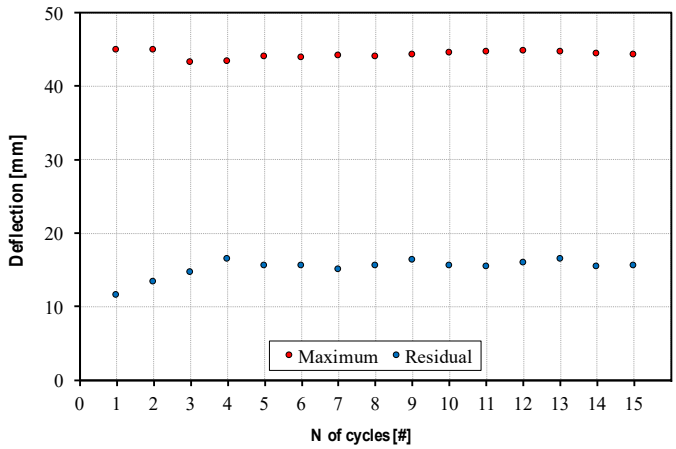

Figure 3.16 – Deflection of the $Ni_{49,8}Ti_{50,2}$ SMC as a function of the number of thermal cycles: fluid flow activation

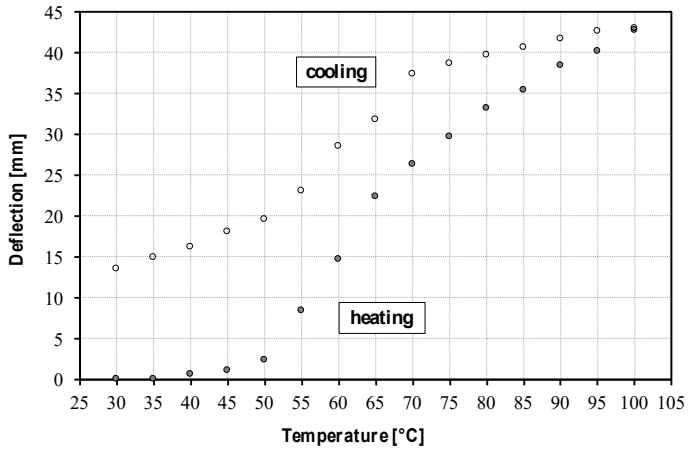

Figure 3.17 – Deflection of the $Ni_{49,8}Ti_{50,2}$ SMC as a function of temperature during heating/cooling ramp: fluid flow activation

Chapter 4

Morphing blade with embedded SMA strips

In this chapter the experimental testing of a novel concept of morphing blade for an automotive axial fan is reported. The proposed morphing blade is made up of a polymeric matrix equipped with NiTi shape memory alloy strips as active elements which were thermally activated by means of a hot/cold air stream flow provided by a purpose-built wind tunnel. The morphing capability of the blade, together with the recovery behaviour of the NiTi strips were studied for four different polymeric compounds in order to find the best solution able to replace conventional actuator systems.

4.1 Blade structure development and activation tests

In a modern car, more than one hundred actuators are used to control engine, transmission and suspension performance, to improve safety and reliability and enhance driver comfort (Stoeckel, 1990). Most of these actuators today are electric motors and solenoids. For this reason, the control systems account for the majority of the weight and volume of vehicle components and in some cases, they are too bulky, expensive and not sufficiently robust for the intended application.

To this regard, renewed interest in automotive control systems is especially due in order to limit fuel consumption and exhaust emissions. More than half of the energy in vehicles is lost as heat to the different cooling systems (engine, driver and passenger compartment space and auxiliary devices) and exhaust gas. Reducing the amount of energy lost in vehicle cooling systems will enhance the efficiency of the vehicles (Lin and Sunden, 2010).

A traditional cooling system is made up of pump, thermostat valve, heat exchanger and cooling fan. The cooling system has to simultaneously balance engine thermal management, passenger thermal comfort and cooling system parasitic losses over all vehicle operating conditions and climate control demands. For a given vehicle application (high and low velocity vehicle, truck and heavy-duty engine), the cooling system technologies evaluated for heater performance are selected with regard to the entire cooling system and thermal management objectives, such as: peak cooling system performance, fast engine warm-up, precise coolant temperature control, thermal comfort, improved fuel economy,

reduced thermal shocks and finally, low cost (Chalgren, 2004). These objectives are met by robust and efficient design including an efficient controllable water pump and electric fan, a high-performance heat exchanger with low pressure drops (air and water side) and an electric flow control valve for precise temperature control during the transient engine load through different ambient temperatures.

In order to improve the engine thermal management, many different methods have been developed in recent years: electric heaters, electric water pumps, heat pumps and fuel-fired coolant heaters. These systems vary in terms of performance, packaging considerations, reliability, costs and auxiliary devices to support them.

In automotive applications, conventional cooling systems are generally not very accurate, not controllable and lead to considerable parasitic losses. In most cases, fans and water pumps have great difficulty in correctly monitoring and maintaining multiple operating temperature levels (Nessim *et al.*, 2012). Cooling systems are designed to simply guarantee sufficient heat removal at maximum engine output conditions in the worst vehicle operating conditions (low vehicle velocity and high temperature ambient). Unfortunately, these operational conditions only represent approximately 5 % of the conditions that the cooling system encounters during its operation (Lehner *et al.*, 2006). In fact, the engine cooling system is significantly influenced by cooling air generated by a ram effect resulting from the vehicle's motion and suction produced by fan operation (Baniasadi *et al.*, 2013). The combined effect of these two factors is highly variable and their coupling with the cooling fan and pump presents a target which is difficult to reach.

In this context, the possibility to realise a passive control system for the performance optimisation of heavy-duty automotive cooling axial fan represents a challenging approach since it would allow to optimal respond to changes in turbomachinery operating conditions, avoiding any external actions on the shaft rotational velocity. In fact, it is well-known that turbomachinery are usually designed and optimised for one operating point and thus the efficiency could be increased if the flow channel geometry is able to adapt to the varying flow conditions.

The proposed system is regulated by a sensorless control taking advantage of SMAs elements, whose phase transformation enables the production of favourable aerodynamic blade shape changes, according to the air flow temperature. Unlike conventional actuation and control systems employed in cooling fans (i.e. on/off clutch and air sensing modulated viscous clutches), the SMA actuation allows to control and adjust the fan performance to the engine thermal requests. This fan's setup can allow an almost continuous operation of the turbomachinery in the maximum efficiency point and not only for a discrete number of operating points. Given that the thermally activated phase transformation does not occur instantly, the SMA enables the development of heavy-duty machines which continuously modulate their working point, following the requested operating change seamlessly. As a result, the passive SMA-controlled system allows to: eliminate the active controls (electric motor, thermostats and valves, and temperature probe), adapt the cooling fan to the engine thermal requests, change the performance independently from the engine rotational velocity, reduce the coolant warm-up time during cold engine starts and eliminate the heat-soak issue.

Against this background, starting from the need to realise a typical forward-swept blade used in partially shrouded cooling fans for automotive applications, this paragraph describes the development and functional characterisation of an innovative morphing blade activated by SMA strips.

The possibility to realize adaptive structures is of great interest in turbomachinery design, owing to the benefits related to enhanced performance and efficiency. To this regard, a challenging approach is the employment of SMA as active element. The morphing blade design was thus performed with the aim of realising an adaptive composite structure of which the thermal activation would provide the

adjustment of the working condition parameters of the axial fan, taking advantage of the SME. The intent to use the embedded SMA elements refers to realise a fan in which the blade shape changes continuously as a function of an external stimulus such as the airflow temperature. In order to study the capability of the morphing blade to adapt its shape according to the fan's operation temperature, the SMA thermal activation was achieved by a hot/cold air stream flow.

The adaptive structure included the polymeric matrix, which ensured the structural integrity of the blade, and the embedded strips, which were the actuator elements. This functional structure allows to study the behaviour of the NiTi strips working in partially constrained conditions since the recovery stress due to the SMA phase transformation enables the production of significant shape changes in the polymeric host structure.

The structure was designed in order to be sufficiently compliant and flexible to support the large deflections induced by the strips and to allow shape recovery, but was also stiff enough to withstand the aerodynamic loads. Since the SMA phase transformation was thermally activated by a hot/cold air stream flow the strips were located into purpose-built slots in direct contact with the fluid flow. The blade sketch with the essential region is reported in Fig. 4.1. As can be seen, the strips were located in the range of about (50–85) % of the blade span and, starting from the midchord, in such a way that their shape modification made a camber curvature variation of the aerofoil. Conversely, the region near the root is depicted as fixed since no actuation elements were placed there.

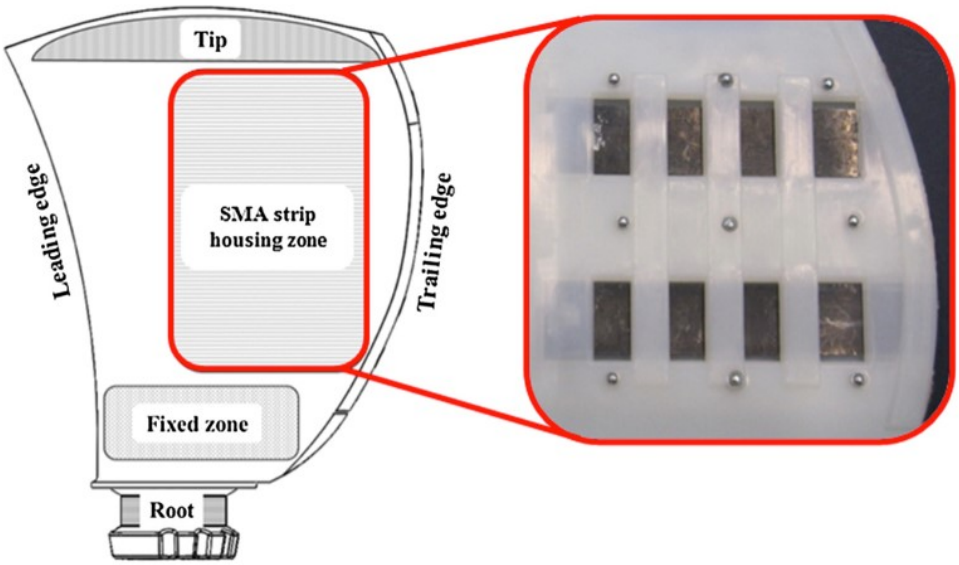

Figure 4.1 – Sketch of the SMA-based blade with its principal regions: root, fixed zone, SMA strips housing zone and tip (ref. 4 of Preface)

To meet the construction needs of injection moulding techniques, the blade geometry comprised the presence of a cover lid in the SMA strips zone which was placed on the suction side of the blade. Figure 4.2a reports the CAD geometry while Fig. 4.2b the corresponding digital images of the real component. Note that the cover was placed on the suction side since the strips exert their flexural deformation in the direction of the pressure side. Moreover, the SMA strip housing zone allows the direct contact between airflow and SMA strips which were housed inside two purpose-built slots clearly visible in Fig. 4.2b.

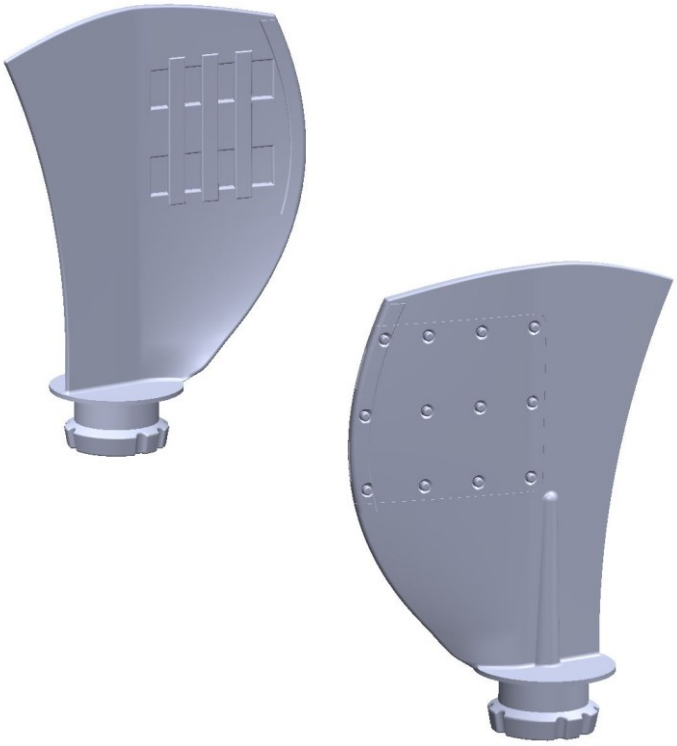

(a)

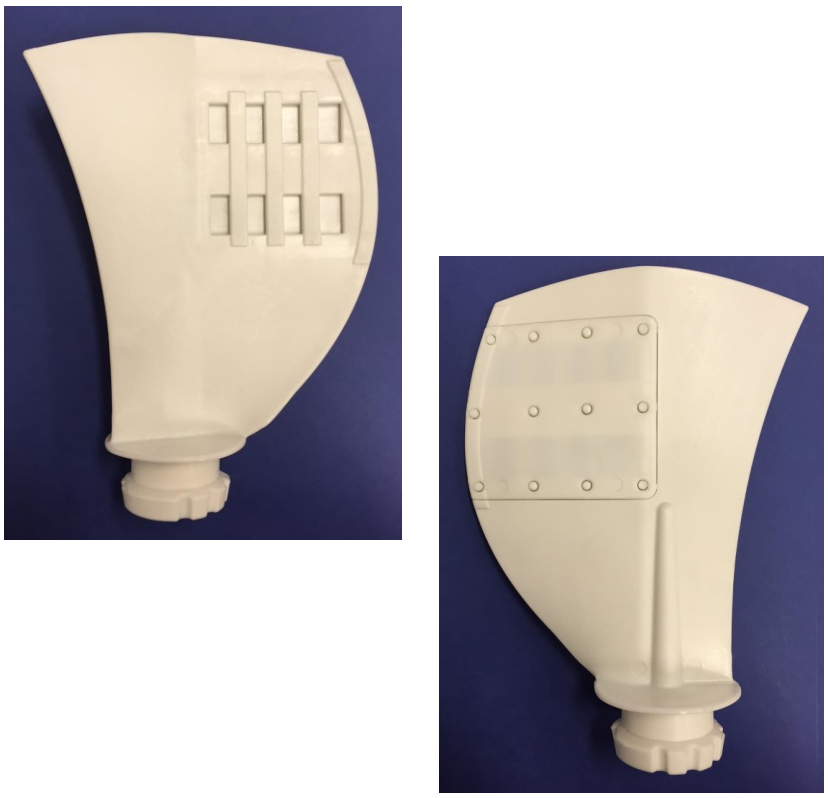

(b)

Figure 4.2 – Blade shape geometry for pressure side and suction side view: (a) CAD geometry and (b) digital images of the real component

The choice of the chemical composition of the SMA elements was linked to practical considerations since the best SMA compound must have transformation temperatures as close as possible to those encountered by the fan during operation. For this reason, the commercially available NiTi shape memory alloy (alloy B, supplied by Memry Metalle Company), of nominal composition $Ni_{50,2}Ti_{49,8}$ was chosen. Starting from the supplied 1,5 mm thick plate, the strips were cut by means of electro-erosion machining in order to minimize microstructural alterations resulting from thermo-mechanical stresses induced by the cutting process. The strips, 77 mm × 15 mm × 1,5 mm, are depicted in Figure 4.3.

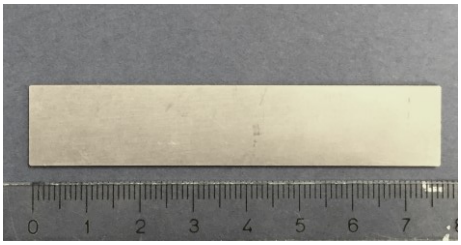

Figure 4.3 – Digital image of the SMA strips

In order to evaluate the TTRs of the chosen alloy, according to the ASTM F2004 standard, DSC tests, by means of a TA Instruments DSC Q2000, were carried out on a small fraction of the strips. A portion of the untreated material was chosen to be characterized in order to obtain useful quantitative information for the shape memory treatments described as follow. For the DSC measurements, a constant heating/cooling rate of 10 °C/min was set.

A complete thermal cycle (heating/cooling) of the obtained phase transformation is given in Fig. 4.4. The characteristic TTRs were extrapolated from the DSC plot through the tangential line method (intersections of a baseline and the tangents to each peak) (Lagoudas, 2008). The experimental values of the TTRs and of the latent heats for both the austenitic, ΔH_A, and martensitic transformation, ΔH_M, are summarised in Tab. 4.1.

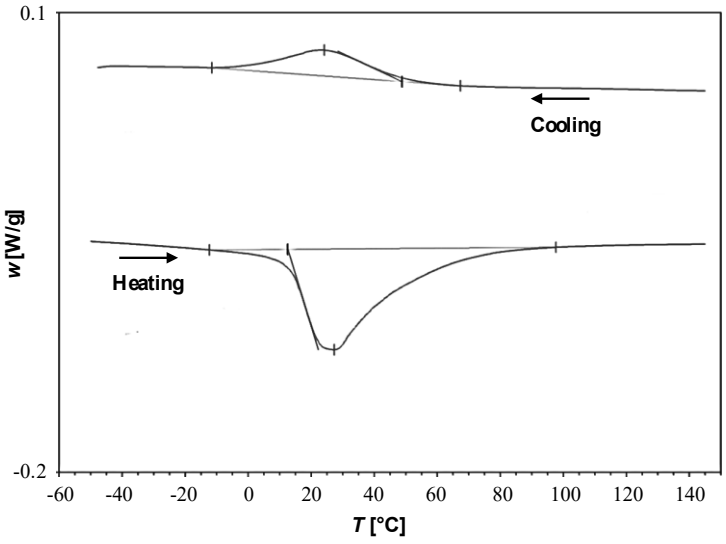

Figure 4.4 – DSC plot of the untreated $Ni_{50,2}Ti_{49,8}$ alloy

Table 4.1 – TTRs and latent heats for both direct and inverse martensitic transformation

Austenite start temperature, A_s	10 °C
Austenite finish temperature, A_f	57 °C
Latent heat per unit mass, austenite (ΔH_A)	12,4 J/g
Martensite start temperature, M_s	48 °C
Martensite finish temperature, M_f	-4 °C
Latent heat per unit mass, martensite (ΔH_M)	3,1 J/g

TTRs values were fundamental for the development of the thermomechanical treatment used to memorise the shape, described below. Figure 4.5 shows a representative scheme of the shape setting treatment.

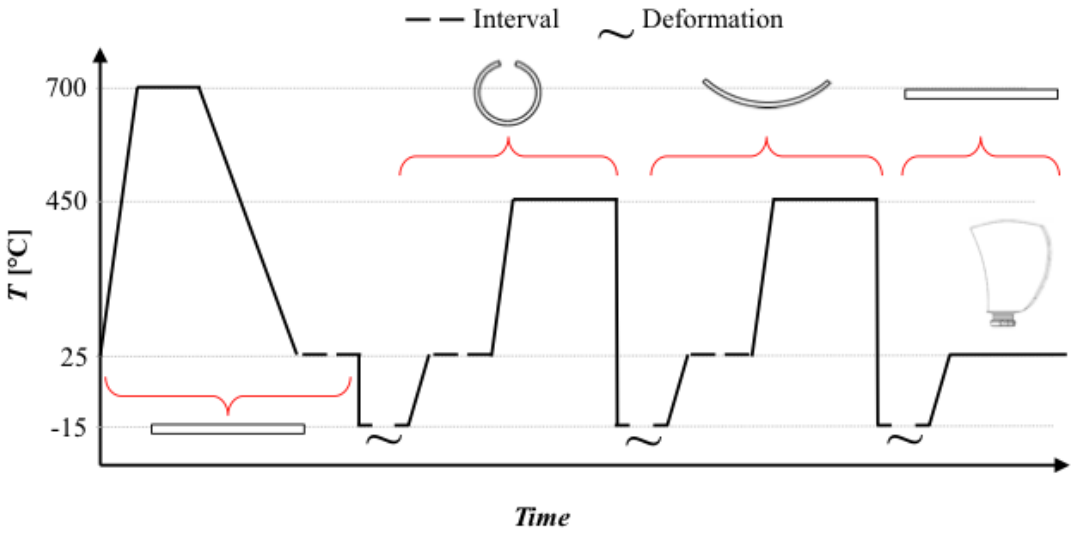

Figure 4.5 – Representative scheme of the shape setting (ref. 6 of Preface)

In order to delete any residual stress of previous deformation history, the samples were first placed in a tube furnace and annealed at 700 °C for 20 min followed by controlled cooling to room temperature. The development of the best thermomechanical treatment for memorizing the defined bent shape, which allows the bending of the blade, was experimentally carried out. Temperature and time parameters were chosen according to the results reported by Rizzoni *et al*. (2013). The authors showed that, for a commercially available Ni-50,8 at. % Ti SMA alloy, heating the material at 450 °C for 25 min represents the best shape memory setting, allowing 92 % of shape recovery.

To memorize the bent shape, the strips were thus subjected to a double thermomechanical treatment. After the annealing, they were first strained in the martensitic state by immersion in a propylene glycol bath cooled to -15 °C. The strips were strained and wound on a cylindrical jig to reach a circular shape, as can be seen in Fig. 4.6a. This setup was then placed into a tube furnace in constrained conditions, in order to avoid the shape recovery on heating. To memorize this first shape, the material was heated at 450 °C for 25 min and subsequently quenched in the propylene glycol bath cooled to -15 °C. After this treatment, the strips were again strained in the martensitic state (performed during the immersion in the propylene glycol bath cooled to – 15 °C) applying opposite bending couples acting at the ends,

and locked into a specifically designed arc clamp, as it is depicted in Fig. 4.6b. To memorize this bent shape, they were again thermally treated, at the aforementioned temperature and time conditions. Finally, the heat-treated NiTi strips were strained to a flat shape, applying a uniform bending load, to be embedded in the blade structure.

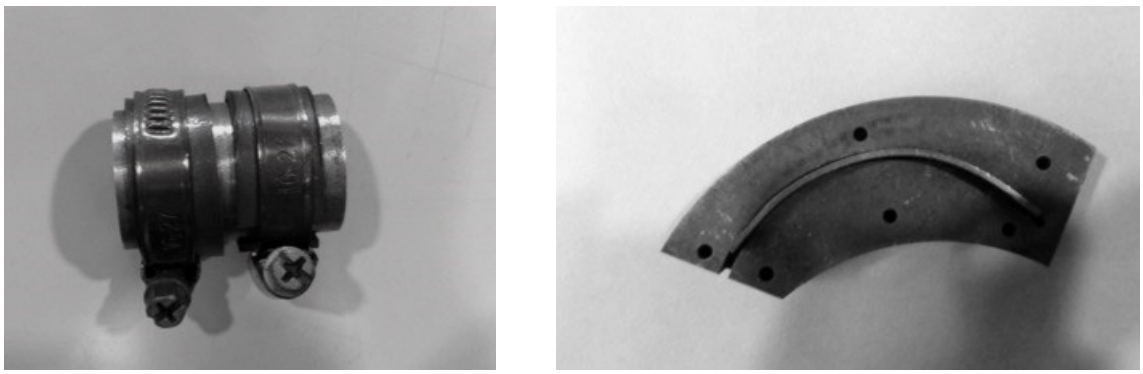

(a) (b)

Figure 4.6 – Experimental setup for the thermomechanical treatment: (a) SMA strips wounded on a cylindrical jig and (b) SMA strip locked into a specifically designed arc clamp

As for the polymeric compound selection, the first remark relates to the fact that the blade design was performed with the aim of being produced by means of injection moulding.

As a result of their good mechanical properties, which include high strength and stiffness to weight, good elongation and impact resistance, thermoplastic polymers are particularly suitable for engineering components and applications. Among them, Nylon PA66 is the most widely-used in the automotive industry, thanks to its versatility, moldability and resistance to high temperatures and harsh chemicals. Moreover, it is common practice to add glass fibre reinforcement to improve stiffness, strength and high temperature properties, or an elastomeric phase to increase the toughness of the thermoplastic matrix.

For these reasons, in the present study the following materials were chosen to be tested: (i) an unreinforced Nylon PA66 named Compound A, (ii) a glass fibre reinforced Nylon PA66 (containing 15% glass reinforcement) and 5% elastomer named Compound B, (iii) a glass fibre reinforced Nylon PA66 (containing 25% glass reinforcement) and 5% elastomer named Compound C and (iv) an acetal resin named Compound D. Some properties of the polymeric compounds are summarized in Tab. 4.2.

Table 4.2 – Properties of polymeric compounds

Properties	Compound			
	A	**B**	**C**	**D**
Tensile modulus [GPa]	1,49	3,89	6,13	3,10
Flexural modulus [GPa]	1,40	3,51	5,14	2,90
Density [g/cm^3]	1,14	1,23	1,28	1,42
Thermal conductivity [W/m °C]	0,243	0,372	0,407	0,405

In order to test the polymeric compounds under the SMA loading, activation tests were conducted in an experimental apparatus, named Single Blade Test Facility (SBTF), including temperature sensors, velocity sensor and digital image devices, was specifically designed to characterise the morphing blade.

The SBTF was composed of (i) a convergent device, (ii) a polyvinyl chloride (PVC) pipe with a diameter of 250 mm and length of 3000 mm, (iii) a flow straightener, (iv) a polymethyl methacrylate transparent measurements section with a square section of 250 mm × 250 mm and 1000 mm in length and (v) exhaust pipe with a diameter of 250 mm and 1000 mm in length. The purpose-built wind tunnel was driven by an axial fan with a nominal 1500 m^3/h flow rate that provided the airflow through a 22 kW-electric heater. By means of the convergent device the air flow is guided into the inlet pipe where the flow straightener allows a uniform and undisturbed flow field in the measurement section, built with PMMA transparent panels to detect the blade shape modifications.

The functional scheme of the system with the main devices is reported in Fig. 4.7. Figure 4.8 reports the image of the measurement section (Fig. 4.8a) and of the flow straightener (Fig. 4.8b). As it is shown in Fig. 4.8a, the blade was positioned according to the flow direction that represents the relative flow velocity in the real operating conditions.

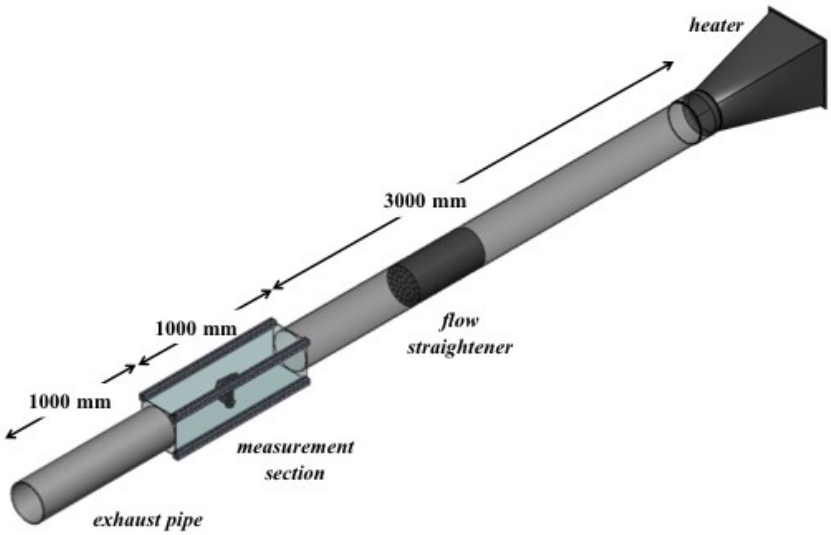

Figure 4.7 – SBTF functional scheme

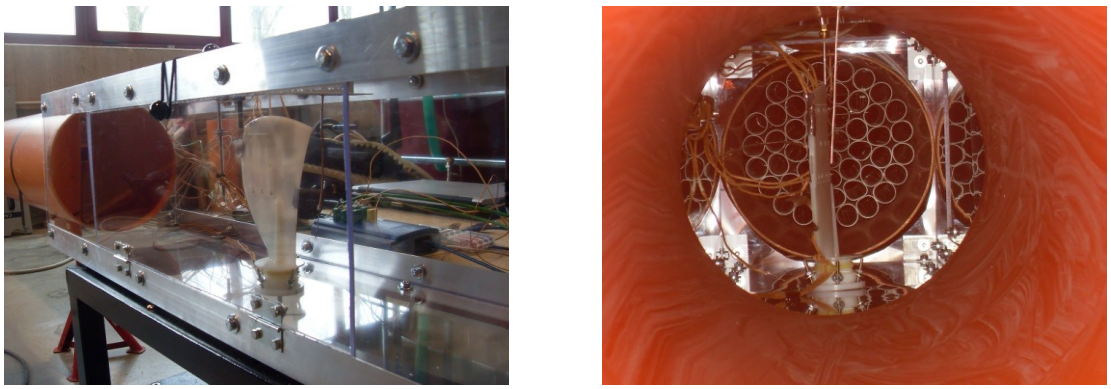

(a) (b)

Figure 4.8 – Digital image of the SBTF: (a) measurement section and (b) flow straightener

The temperature of the airflow was measured by means of mineral insulated thermocouples type K placed upstream of the blade (at the shroud and hub positions) and at the outlet of the measurement section, as it is depicted in Fig. 4.9.

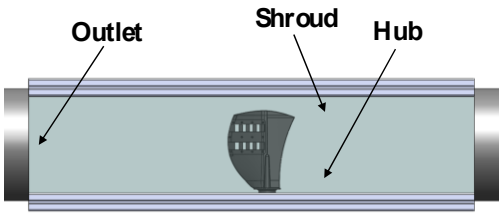

Figure 4.9 – Thermocouple arrangement in the measurement section

Figure 4.10 reports the experimental temperature trends as a function of time, in the sections illustrated in Fig. 4.9. The thermal cycle consists of a heating ramp, in which the blade is heated from room temperature, and a cooling ramp, which starts 60 s after the last thermocouple has reached 80 °C. The cycle is stopped when all the thermocouples have cooled down to 30 °C. As shown in Fig. 4.10, the SBTF enables to obtain uniform thermal conditions of the airflow which hits the polymeric blade structure. The monitoring of the airflow temperatures enabled to evaluate the repeatability and reproducibility of the tests.

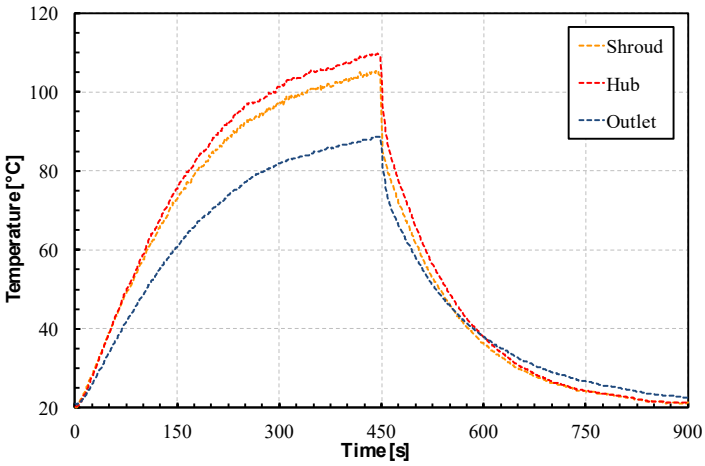

Figure 4.10 – Thermal performance evolution of the airflow during heating and cooling ramp

The hot air stream flow obtained by the electric heater and driven by an axial fan, provided an air stream flow of about 8 m/s. Moreover, the electric heater allowed the obtainment of an air flow stream characterized by a highly reproducible timewise thermal gradient, which can reach values of up to about 12 °C/min in heating mode and up to about 6 °C/min in cooling mode.

To this regard, it is important to note that the focus of the present analysis is to realise a system control for a heavy-duty automotive cooling axial fan and it is therefore necessary look at its working conditions. In this application, the rotational velocity of the fan is almost constant, but the engine load changes according to the working condition of the operating machine. For these reasons, the thermal energy that must be removed from the engine changes during operation and the cooling fan must be designed in order to remove the thermal energy at the engine load peak. Figure 4.11 illustrates a typical temperature variation for a heavy-duty engine that is related to the temperature measurements reported by Nessim *et. al* (2012) for a heavy-duty diesel engine TDC 6V2015 (6 cylinder, engine displacement of 12 l) during warm-up.

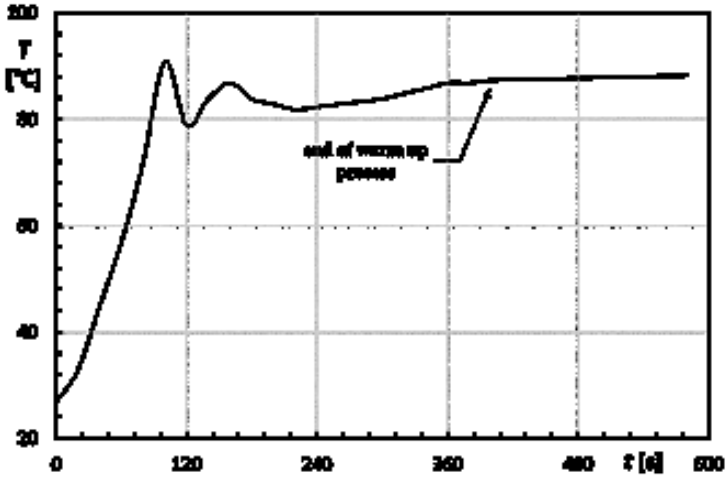

Figure 4.11 – Temperature trend during the engine warm-up (Nessim *et. al*, 2012)

The temperature trend reported in Fig. 4.11 refers to the cooling water temperature and represents only the typical temperature variation that occurs in a typical cooling circuit. It can be noticed that the maximum temperature does not exceed 95°C and the cooling water reaches a stable temperature at about 420 s from the engine start. The steep ramp and the following sinusoidal temperature variation are due to the action of the thermostat valve that controls the water flow rate through the cooling circuit. For the aim of this study, the temperature gradient that characterises the engine warm-up is related only to the temperature difference between the start and end warm-up temperature compared to the warm-up time. From the temperature and time data reported in Fig. 4.11, it can be seen that the temperature gradient, obtained as the angular coefficient of a liner interpolation between the first point and the final point of the engine warm-up, is equal to about 9 °C/min.

According to these analysis, the temperature gradients which can be obtained by the SBTF are consistent with the operating conditions of the fan when used in its normal duty. The thermal inertia of the automotive cooling water circuit induces a time-wise thermal gradient in the air stream which has the same order of magnitude as the thermal gradient reproduced in the SBTF wind tunnel.

To study the thermal condition of the airflow and its effect on the polymeric blade structure, preliminary thermal tests involved the comparison of the different compounds, without the strips. For this reason, the temperature evolution during the heating and cooling ramp was studied through the welded tip thermocouples type K placed on the polymeric structure and inside the measurement section, as described above.

With regard to the blade, Fig. 4.12 reports the scheme (Fig. 4.12a) with the measurements and the image (Fig. 4.12b) of the fourteen measurement points placed on the blade surface at the pressure side. As can be seen, five thermocouples were placed at half of the height of the slot for the first strip (named s that is shroud), five thermocouples were placed at half of the height of the slot for the second strip (named m that is midspan) and four thermocouples were placed at 50 mm from the measuring section M (named h that is hub). The same arrangement was adopted for the measurement points at the suction side.

The analyses of the different compounds regarded the comparison between the pressure side and suction side measurements. The temperature evolution for the welded tip thermocouples placed at shroud, midspan and hub positions for pressure side and suction side are shown in Fig. 4.13 and Fig. 4.14, respectively.

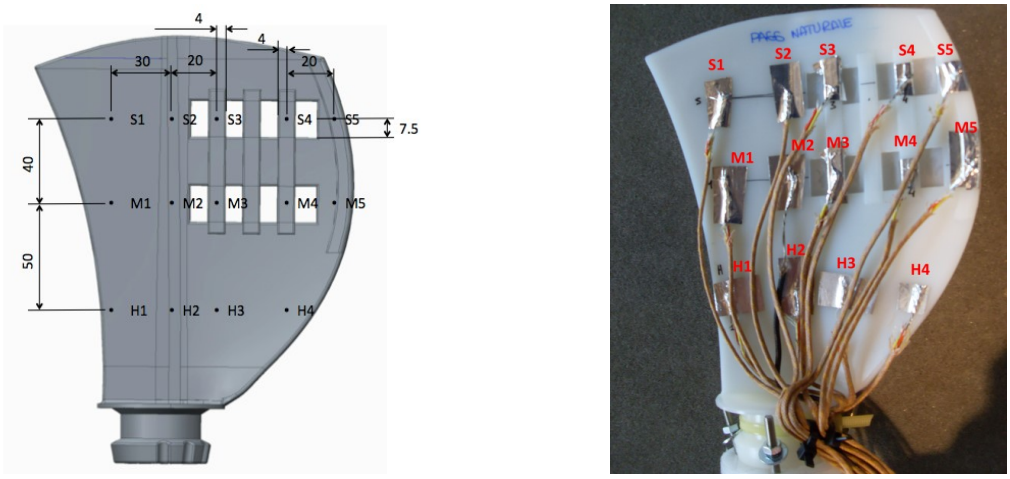

(a) (b)

Figure 4.12 – Thermocouple arrangement for the polymer thermal characterisation: (a) dimensioned CAD-scheme of the blade and (b) image of the pressure side

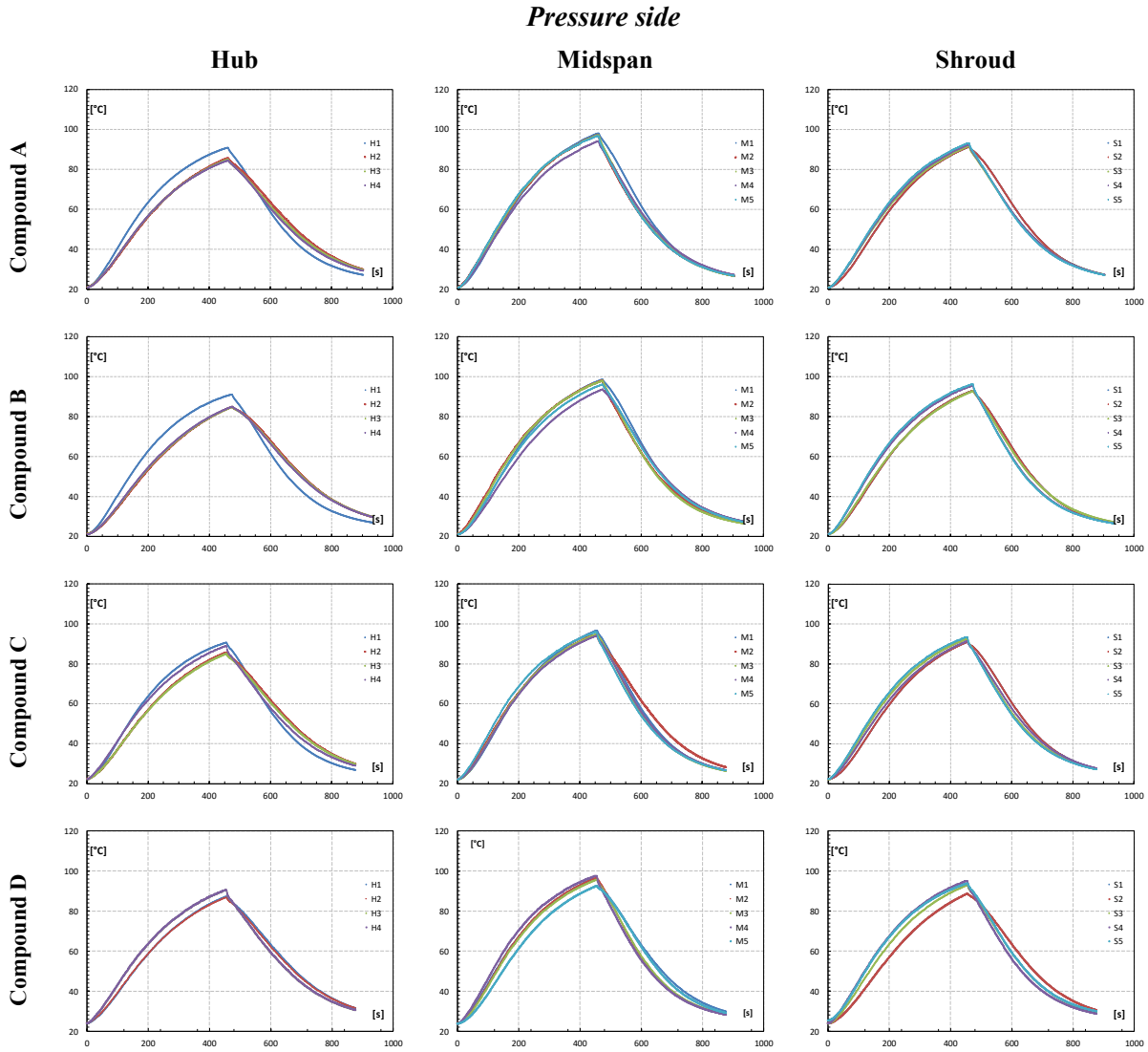

Figure 4.13 – Temperature trends for the polymeric matrices: pressure side

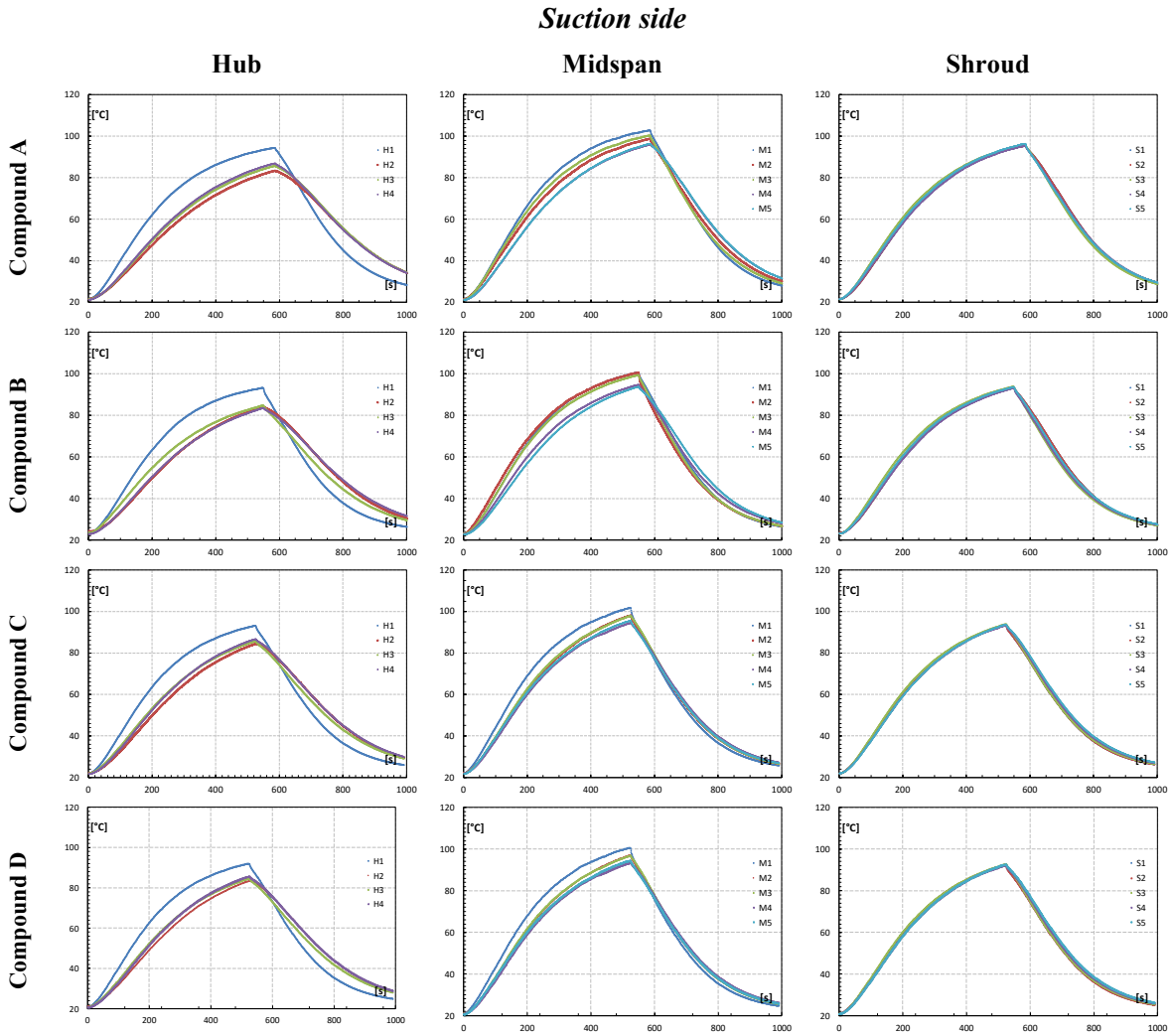

Figure 4.14 – Temperature trends for the polymeric matrices: suction side

As can be seen from the depicted trends, midspan shows the highest temperature compared with shroud and hub for both pressure side and suction side. Conversely, hub appears as the coldest zone while shroud shows intermediate temperature trends which are comparable with midspan. As expected, for all the compounds the pressure side heats up in less time with respect to suction side.

Figure 4.15 reports the calculated thermal gradients for the polymeric matrices taken into account and, in particular, the reported values are the mean values for the fastest thermocouples (shortest time to reach 80 °C, Fig. 4.15a) and for the slowest thermocouples (longest time to reach 80 °C, Fig. 4.15b). From the experimental results, Compound C seems to show a greater capacity of conduction. To this regard, Compound C shows the lower different between thermal gradients of pressure side and suction side of those measured. Moreover, thermal gradients of the thermocouples related to pressure side and suction side are characterised by higher values, compared with the other polymeric compound.

As mentioned, the thermal activation of the strips and the resulting blade deflection were achieved by a heating and a cooling ramp. During the activation tests, welded tip thermocouples type K were placed on the polymeric structure and on the SMA strips to evaluate the temperature evolution. Figure 4.16 reports the thermocouple arrangement adopted for the thermal activation tests.

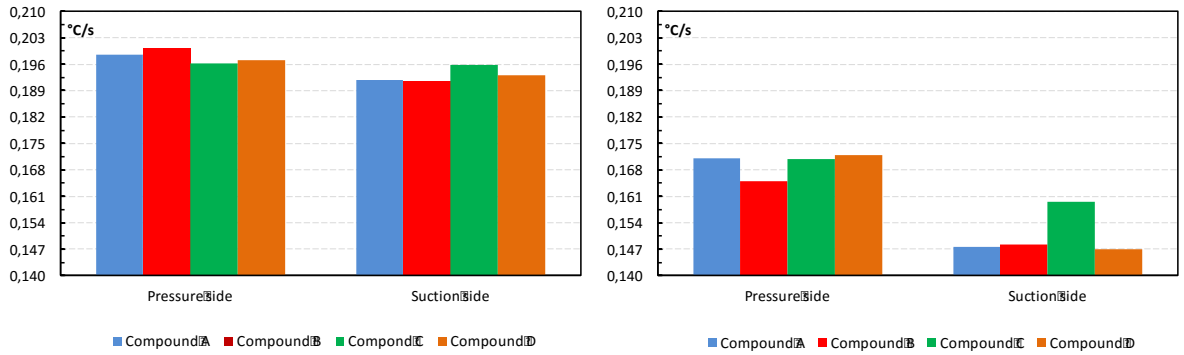

(a) (b)

Figure 4.15 – Thermal gradients for the polymeric matrices: (a) thermal gradients for the fastest thermocouples and (b) thermal gradients for the slowest thermocouples

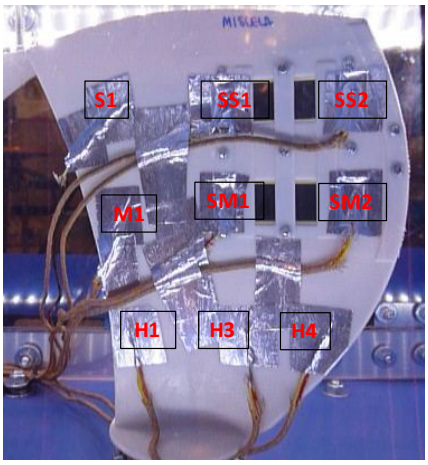

Figure 4.16 – Digital image of the thermocouple arrangement on the pressure side for the thermal activation

Figure 4.17 shows the experimental temperature evolution as a function of the time of the airflow temperature in conjunction with the polymeric structure (Fig. 4.17a) and SMA strips (Fig. 4.17b) measured by using the welded tip thermocouples. The temperature trends reported in Fig. 4.17 were obtained with Compound A but, given that uniform thermal conditions of the air flow stream and the high-reproducibility of the temperature trend on the blade were achieved by the realised SBTF, the depicted trends are representative for the four considered polymeric matrices. The air temperature evolution is calculated as the average value between shroud and hub positions. As can be seen, the temperature gradient in both the polymeric matrix structure and the SMA strips are quite similar and the blade shows an almost uniform surface temperature pattern.

Figure 4.17a shows that it was possible to achieve uniform thermal conditions of the air flow stream on the blade during the execution time, both in the heating ramp (maximum hub-to-shroud temperature difference of about 1,5 °C) and in cooling ramp (maximum hub-to-shroud temperature difference of about 0,4 °C). According to the temperature-time trends reported in Fig. 4.17b, it can be noted that the system enables an almost uniform thermal condition to be obtained on the strips during both the heating

and the cooling ramps. On heating it was possible to reach 80 °C after 450 s, while on cooling the temperature reached 30 °C after 850 s. In addition, the temperatures measured for the SMA strips (SM1, SM2, SS1 and SS2) are very similar to each other and for this reason, in the following analysis, the SMA strip temperature refers to the average values of these four measurements.

The temperature–time trends measured on the blade surface are comparable with those measured in the SBTF (see Fig. 4.10) revealing that the temperature gradient realized by the SBTF is suitable for the aim of the present research.

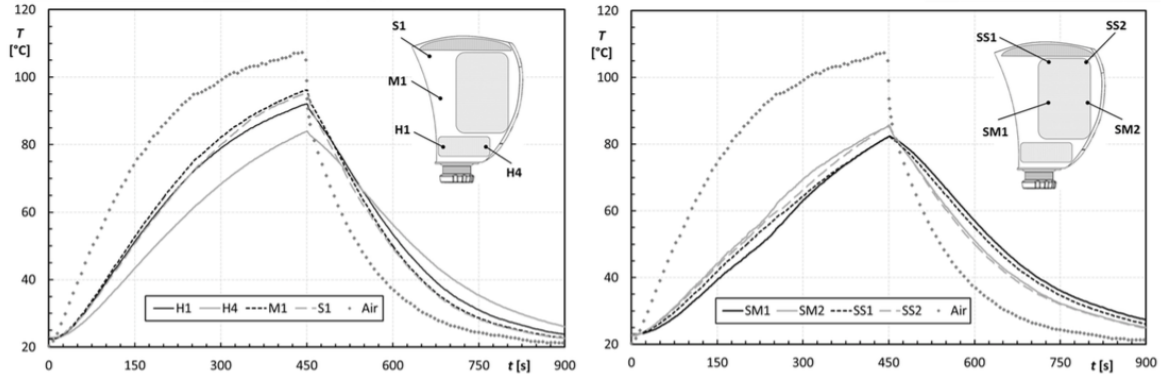

Figure 4.17 – Temperature trends during thermal activation (heating and cooling ramp): (a) polymeric structure and (b) SMA strips (ref. 3 of Preface)

The thermal cycle comprises a heating ramp during which, starting from room temperature, the blade was first heated by hot airflow from the fan and electric heater. In particular, when the temperature of the strips reached A_f they tended to recover the memorised bent shape and the blade structure was forced to bend, reaching the maximum deformation as the fluid flow reached the maximum temperature. According to the calculated TTRs of the strips, they were heated to reach an average value of 80 °C. Subsequently, the blade was cooled down to room temperature, to achieve the martensitic phase transformation, only by the supplied air provided by the fan, when the heating system was switched off.

To quantitatively evaluate the blade deformation on thermal activation, digital image analyses were performed. Taking advantage of the transparency of the measurement section, modification of the blade shape was evaluated through digital camera video acquisition which was synchronised with the temperature evolution to link the shape evolution with the temperature changes. During the activation tests, the blade shape modifications were continuously recorded by means of video acquisition of three digital cameras which were aligned at the blade tip, suction side and pressure side, respectively. The camera arrangement used for the video acquisition measurements is given in Fig. 4.18. The camera aligned with the blade tip at a distance of 300 mm (camera A in Fig. 4.18) enabled the aerofoil camber deflection to be detected. The camera aligned with the suction side, placed at a distance of 600 mm from the convex blade surface (camera B in Fig. 4.18) enabled the blade shape modification to be detected along its height. Furthermore, blade shape modification along the blade height was also detected by camera C placed close to the concave blade surface at a distance of 200 mm (camera C in Fig. 4.18).

The camera arrangement and settings allow spatial resolution up to 0,16 mm that is considered suitable for evaluate the blade shape modification during the activation tests.

In addition to 2D video acquisition, to study the blade shape modifications, which occur along the blade span during the activation cycles a 3D non-contact surface detection has been considered.

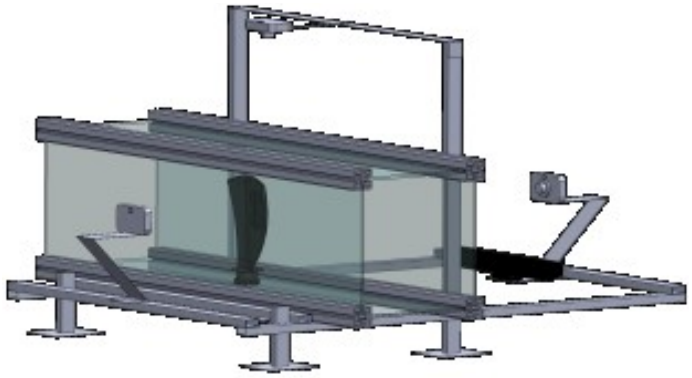

(a)

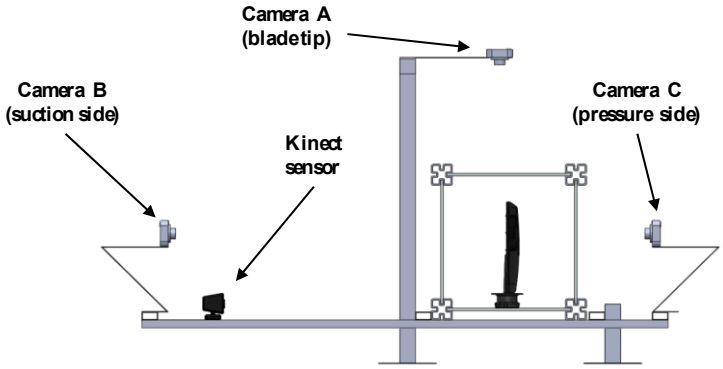

(b)

Figure 4.18 – Experimental setup for measuring 2D and 3D blade shape modification: (a) isometric view and lateral view (ref. 4 of Preface)

In order to control the thermo-fluid dynamic parameters of the airflow that hit the blade surface, it was essential that the PMMA panels were not removed during the test. For this reason, a conventional 3D scanner, such as a laser scanner or contact touch probe, could not be used. At the same time, such devices are usually unsuitable for real-time applications. Therefore, the 3D blade shape was acquired during the tests using the Kinect sensor that is a motion sensing camera, released as a peripheral device for the Xbox360 console and Windows, which is capable of providing streaming non-contact depth information and color information at a resolution of (640 × 480) pixels with a rate of 30 frames per second (Microsoft Corp., 2014). It contains (i) an RGB sensor imaging made up of double camera arrangement, (ii) an InfraRed (IR) emitter and an IR depth sensor and (iii) a 3-axis accelerometer to control its orientation. Since traditional 3D motion capture systems are generally complex and very expensive, the Kinect-based 3D surface imaging system could provide a cheap and fast scanning system with a sufficient accuracy for a number of common applications, such as health, robotics, biomechanics and engineering fields (Gonzalez-Jorge *et al.*, 2013, Khoshelham and Elberink, 2012,

Yue *et al.*, 2014). By means of its 3D depth sensor it can detect the distance between the sensor and the object and it can also provide the 3D model in cloud point format. As depicted in Fig. 4.18, the Kinect was placed with the IR emitter axis perpendicular to the suction side blade surface (aligned with camera B and camera C), at a distance of 600 mm. As well as for image acquisitions, also for the 3D blade shape scan acquisitions, they were synchronized with the temperature in order to control the shape changes related to the temperature trend. Point cloud data were obtained by the freely available Software Development Kit (SDK) provided by Windows, and by using specific open source software (i.e. Blender, MeshLab). Point cloud data were then processed and converted into a polygonal representation of the scanned blade.

From a macroscopic point of view, the final deformed shape of the blade is the results of the combination of the load provided by the SMA strips and the stiffness provided by the polymeric matrix. The blade shape change in terms of mean line deflection, develop on each blade-to-blade plane as a function of the blade span location. In Fig. 4.19 the comparison between the blade tip image acquisitions of the two blade shapes, for all the polymeric matrices, is reported: (i) initial (non activated) condition and (ii) maximum deflection (activated) captured from the blade tip view.

From the comparison among the different compounds at the activated condition it can be seen that the greatest deformation is localized at the trailing edge (TE) of the blade where the deflection of the SMA strips imposes the maximum strain on the polymeric structure. Also, on the first part of the blade chord, the blade shape changes according to the memorized bent shape and the modification of the leading edge (LE) determines a variation of incidence angle during the operation. As a result, position of the SMA strips realizes a camber curvature variation of the aerofoil and consequently, a variation of the fan performance. More details can be found in ref. 7 of Preface.

To study the blade deformation achieved by the shape recovery of SMA strips, a quantitative evaluation of the deformations of the aerofoil shape at the blade tip was performed. The functional structure comparison comprised digital image analysis techniques which enabled to study the blade deflections and to evaluate the most suitable polymeric matrix for the intended application. The four polymeric compounds were compared taking into account the maximum distance m (maximum camber) from the chord length (LE to TE line), as shown in Fig. 4.20. This distance was measured by means of CAD software reconstruction of the tip blade deflection, starting from the video frames recorded by the camera aligned with the blade tip. In particular, $m_{\text{non-def}}$ corresponds to the maximum distance at the initial condition before the first activation cycle while m_{i} corresponds to the maximum camber at the i^{th} instant during the thermal cycle. Figure 4.21 reports the blade deflection calculated as $(m_{\text{i}} - m_{\text{non-def}})/\, m_{\text{non-def}}$ as a function of the average strip temperature is proposed for the heating ramp as well as for the cooling ramp. As can be seen, the blade deflection increased during heating, reaching the maximum value at the maximum temperature. Given that the SMA thermally activated phase transformation does not occur instantly, a progressive and continuous increase in the deflection is observed. Note that, for all the polymeric compounds and SMA strip couplings, the effects of the phase transformation inside the strips appear at about 45 °C, given the presence of the polymeric structure constraint. It is well-known that the TTRs increase, with respect to the stress-free condition, when a mechanical load is applied.

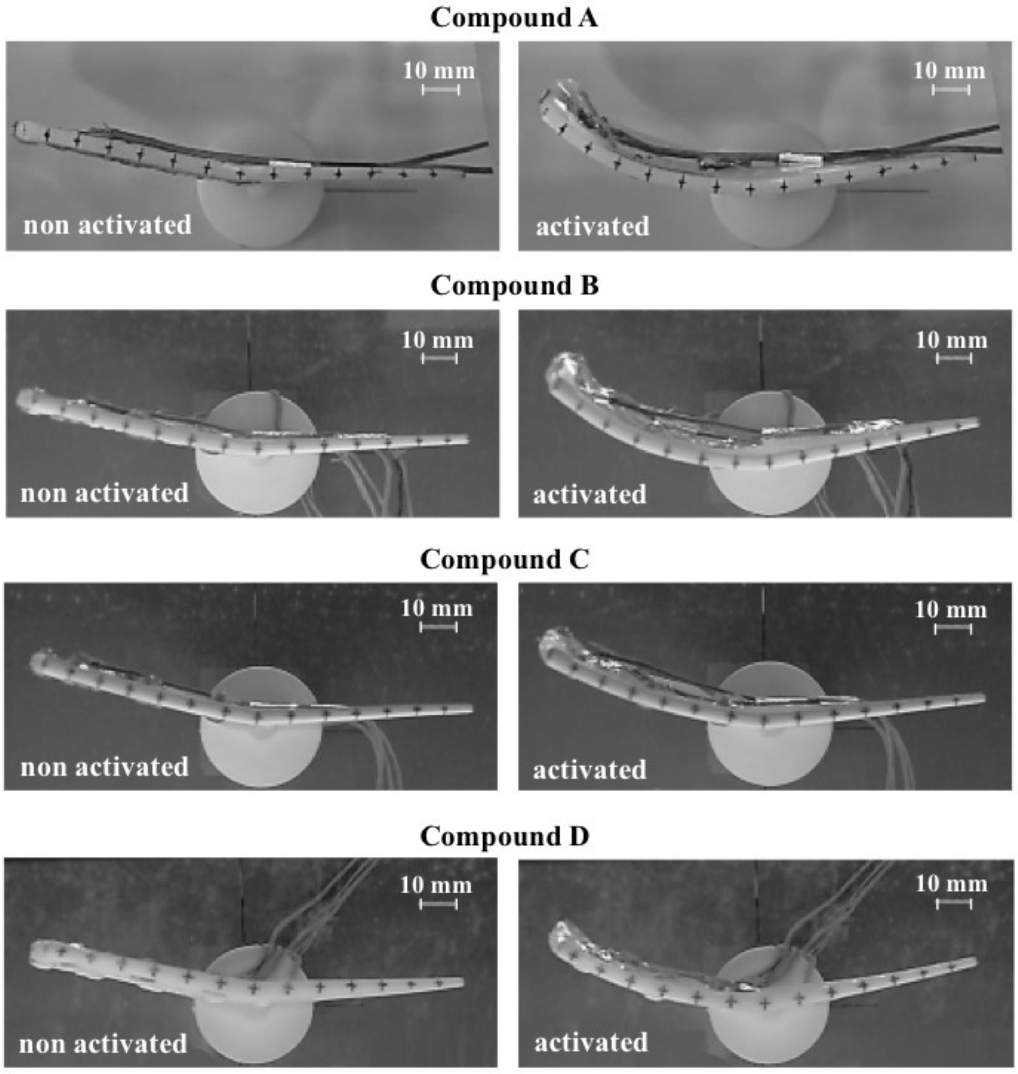

Figure 4.19 – Digital captures from the recorded video at blade tip view: comparison of the four polymeric compounds at the non activated and activated condition

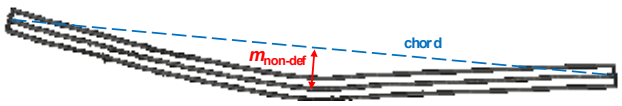

(a)

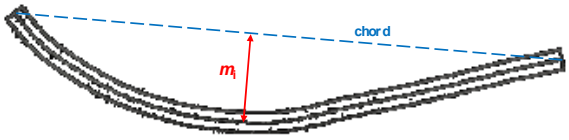

(b)

Figure 4.20 – Blade tip CAD reconstruction and measurement criterion: (a) maximum camber at the initial condition (room temperature) and (b) maximum camber at the i^{th} instant (activated) (ref. 4 of Preface)

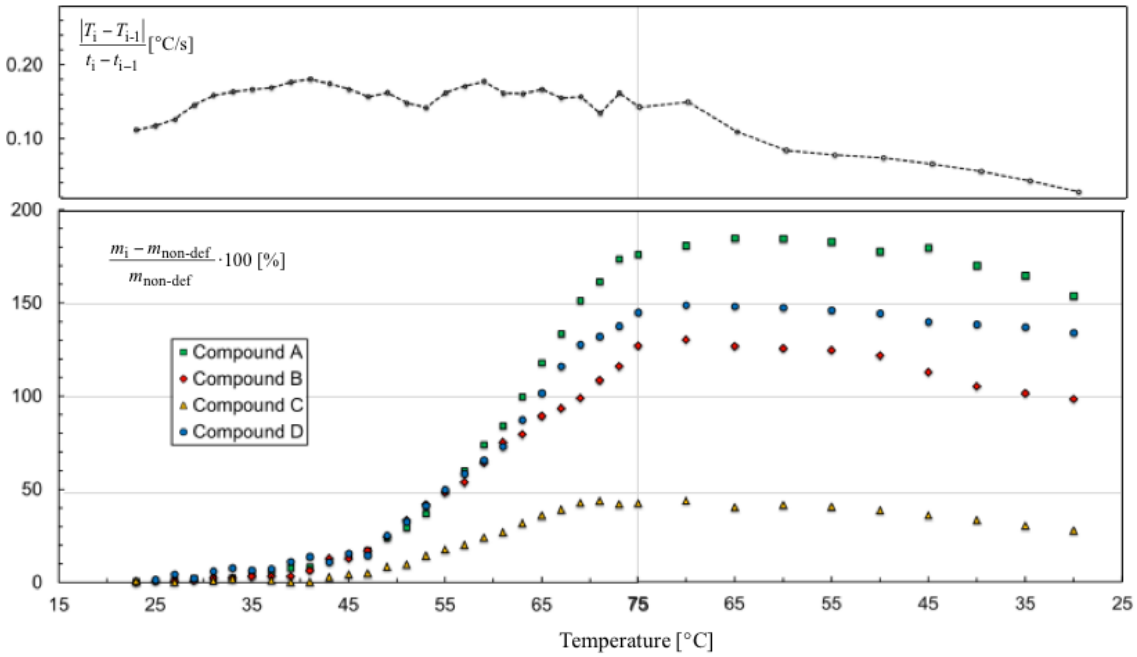

Figure 4.21 – Camber deformation for the four polymeric compounds during the heating ramp and cooling ramp (ref.4 of Preface)

According to the different mechanical properties of the polymeric compounds reported in Tab. 4.2, the blade deflection trends are closely related to these features. In particular, Compound A (flexural modulus = 1,40 GPa) shows the steepest ramp, as a result of the minimum flexural modulus value. Conversely, Compound C (flexural modulus = 5,14 GPa), which had the greatest amount of glass reinforcement, showed a very low deflection. The large addition of glass fiber reduced the functional structure deflection capability on heating. Consequently, Compound B showed a behavior between Compound A and Compound C. These experimental findings are consistent with the mechanical properties and showed the strong influence of glass fibre reinforcement on blade shape modification. Finally, Compound D exhibited a blade deflection evolution very similar to that of Compound B, since the flexural modulus of these two polymeric matrices is quite comparable. Since the morphing blade takes advantage of the OWSME, during subsequent cooling the recovery behaviour was achieved by the polymeric compound elasticity in conjunction with the SMA forward transformation. When considering the blade deflection as a function of the average strip temperature for the cooling ramp, Compound A shows increased deformation instead of decreased temperature. This phenomenon could be due to over deformation during the heating ramp (see the steepest deformation trend), which caused the plastic deformation of the blade structure. Thus, the large blade deflection for Compound A proved that, for the intended functional structure application, the flexural modulus of unreinforced Nylon PA66 is too low. On the contrary, for the other compounds, the decrement of the blade deflection is consistent with the cooling ramp. In detail: (i) Compounds B and D showed almost the same recovery trend, which also occurred for the heating ramp and (ii) Compound C showed an almost horizontal recovery trend. As a result, Compounds B and D appear to be the most suitable polymeric matrices for the development of the blade structure coupled with the SMA strips.

The average temperature gradient trends for the heating and cooling ramps are also reported in Fig. 4.21. The airflow modification and then the modification of the temperature gradient trend are clearly

visible starting from 45 °C at which the blade deflection caused flow disturbance and a different airflow field around the blade. Instead, in the cooling mode, the average temperature gradient is less steep and the flow disturbance is much less evident because blade deflection during recovery is more gradual compared to that of the heating ramp.

In order to highlight the differences between the polymeric compounds, in Fig. 4.22, the four blade tip image acquisitions are reported at (i) the instant at which the average strip temperature reached the peak value (named deflection at peak temperature) and (ii) the end of the thermal activation cycle (named residual deflection). The difference in the camber variation among the four structures is a consequence of the trailing edge deflection, while at the leading edge, the blade tip shape modification is less pronounced even though the leading edge deformation is remarkable in the case of Compound D.

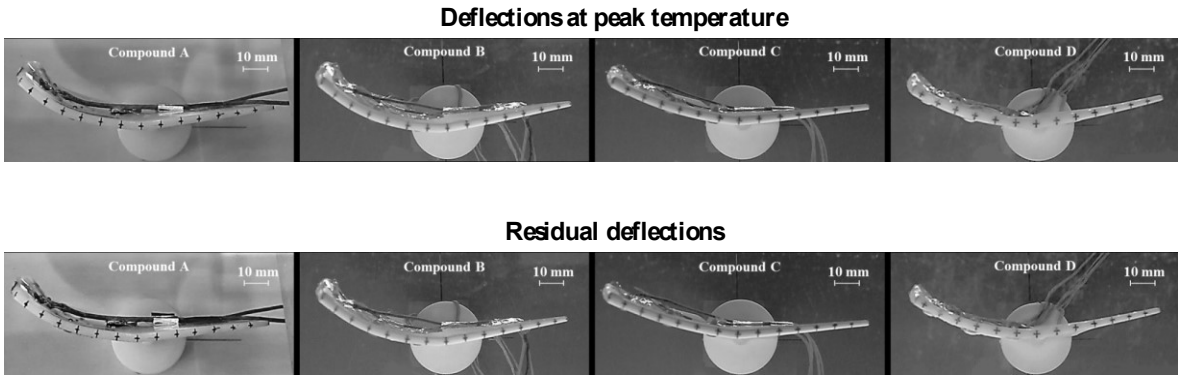

Figure 4.22 – Digital captures from the recorded video at blade tip view: comparison between the deflection at peak temperature and the residual deflection. Adapted from ref. 4 of Preface

Blade deflection in terms of (i) deflection at peak temperature, (ii) residual deflection and (iii) blade structure recovery are summarized in Tab. 4.3. The latter term is calculated by the difference between deflection at peak and residual temperature. The blade structure recovery values reported in brackets refer to the blade structure recovery divided by the maximum value. According with the values reported, Compound B, coupled with the thermally treated SMA strips, shows the best compromise between the value of deflection at peak temperature and the capability of recovery. As a result, Compound B was chosen as the matrix for the blade structure and its deflection capability was evaluated through repeated thermal cycles described as follows.

In order to study the effects of cyclic activation on the thermo-mechanical response of the SMA strips, the morphing blade was subjected to consecutive transformation cycles. It should be pointed out that the first thermal cycle corresponded to the first thermal cycle of the polymeric matrix and the SMA strips. The analysis is proposed for (i) the aerofoil camber at peak temperature and (ii) the aerofoil camber at the end of the activation cycle. The shape changes were evaluated by the CAD reconstruction, provided by using the digital images acquired during the activation tests at the blade tip view.

Figure 4.23a reports the trend of the aerofoil camber at peak temperature during the activation tests. The experimental results highlight that the blade stabilization in the activated condition is obtained from the 2nd activation test, in which the maximum camber is equal to about 21 mm, compared to a

camber value of 9 mm that characterizes the blade tip aerofoil in the initial condition. The variation in the maximum camber value is less than 1 mm. To study the capability of the blade to recover the same shape at the end of the thermal cycle, the residual deflection values are depicted in Fig. 4.23b. Experiments reveal that SMA strip displacement results in a camber variation equal to about 3 mm for each thermal activation cycle. Even though the variation of the residual deflection values is less than 0,5 mm, the residual deflection trend tends to get closer to the maximum camber trend. Therefore, the ability of the SMA strips to induce blade deflection progressively decreases as the thermal cycles increase.

Table 4.3 – Comparison of the blade deflections (ref. 4 of Preface)

Deflection	Compound			
	A	**B**	**C**	**D**
Peak Temperature [mm]	17,6	20,1	14,3	17,0
Residual [mm]	16,0	18,5	12,8	15,6
Blade structure recovery [mm]	1,6 (0,09)	1,6 (0,08)	1,5 (0,11)	1,4 (0,08)

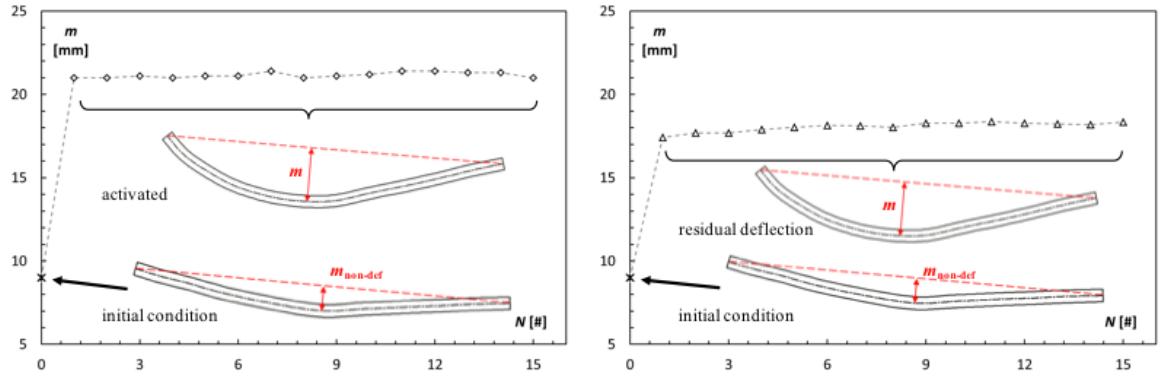

(a) (b)

Figure 4.23 – Blade structure evolution: (a) aerofoil camber at peak temperature and (b) residual deflection (ref. 4 of Preface)

4.2 Morphing analyses

Since the evaluation of the blade shape is fundamental for the overall comprehension of the SMA strip action as well as for the modification of the cooling fan performance, a detailed blade shape analysis was carried out. Due to its wide field of application, shape analyses of static and dynamic objects with non-contact shape techniques represent a hot topic. Considering the 3D surfaces, the shape measurement techniques are concerned with detecting the geometry information from the image of the measured object. These approaches are known in literature as Reverse Engineering (RE). RE is usually used for the reconstruction of an object of which the geometry is composed of several surfaces with

different shapes. In the present application, the geometry is not composed of different parts, but the blade is positioned in the measurement section and a non-contact method (optical) must be used.

As reported by Schwenke *et al.* (2002), optical methods can often acquire more data in less time, with the advantage of measuring parts without contact. However, the scanning result may not achieve high level of accuracy and may have a higher uncertainty when compared to tactile systems (Sansoni and Docchio, 2005). In order to address these issues, the combination of optical measurements and tactile systems, even at different times and locations, can yield a highly accurate 3D representation of the physical object (Carbone *et al.*, 2001, Chen and Lin, 1997). In the present study, tactile systems cannot be used and for this reason, blade shape detection was carried out by means of (i) digital image analysis (that provides quantitative and accurate blade detection) and (ii) optical scanning (that provides qualitative blade detection).

Starting from the results reported for the Compound B a detailed two-dimensional and three-dimensional analyses of the blade shape modification that occurs in the 1st and 15th thermal cycle is proposed. The comparison described as follows will highlight (i) the modification of the blade shape during consecutive activation cycles and (ii) the capability of different non-contact methods of detecting and recognizing the blade shape modifications.

As for the two-dimensional analysis, Fig. 4.24 reports the blade tip superimposition between the initial shape and maximum deflection for the 1st and 15th activation cycle. The values of the deviation between the initial blade shape and the maximum deflection, occurring at peak airflow temperature, were obtained by the marker points drawn on the tip. Superimposed black vectors join the same marker from the initial condition (black marker) to the activated condition (red marker). In this way, deviation intensity and direction are easily recognizable. The reported values represent the length of the vector in mm.

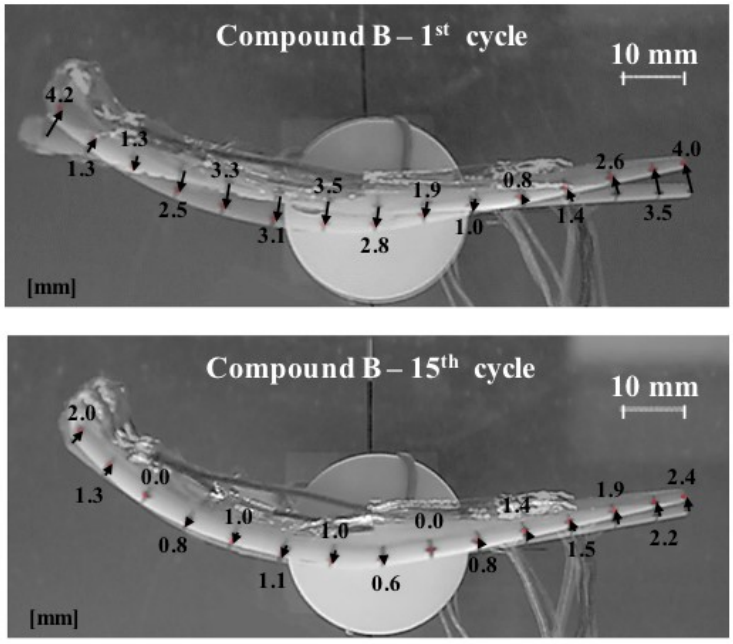

Figure 4.24 – Blade tip superimposition between the initial shape and the maximum deflection for the 1st and the 15th activation cycle (ref. 4 of Preface)

In more detail, the superimposition created for the 1st activation cycle shows that blade deformation occurs along the entire aerofoil chord, while for the 15th activation cycle, blade deformation is localized only on the ends of the aerofoil chord. The deformation imposed by the SMA strips during the 1st activation thermal cycle implies significant modification of the aerofoil meanline. The polymeric blade structure is not able to fully recover this meanline modification; in fact, in the blade tip capture realized for the 15th activation cycle, the SMA strip activation induces blade shape modification only in the leading edge and trailing edge regions. The ability of the SMA strips to induce blade deformation decreases as a function of the number of activation cycles and the modification is increasingly localized at the end of the aerofoil.

In addition to blade tip analysis, by using the digital images acquired by the suction side camera (camera C, see Fig. 4.18) the blade shape modification along the blade height can be studied. Given that any 3D curved surface could be represented through Cartesian coordinates, the blade shape modification was analysed in this way. To determine the coordinate variation with the shape evolution, a suction side video acquisition was considered since the welded tip thermocouples placed on the pressure side prevent the detection of the whole blade surface. Thanks to a regular pattern depicted on the suction side of the blade surface, the comparison between the shapes at (i) initial condition and (ii) deflection at peak temperature were taken into account.

In the same way as the blade tip analysis, Fig. 4.25 reports (i) superimposition between the initial shape and deflection at peak temperature for the 1st and 15th thermal cycle and (ii) the values of the deviation between the initial blade shape and the deflection that occurs at peak airflow temperature.

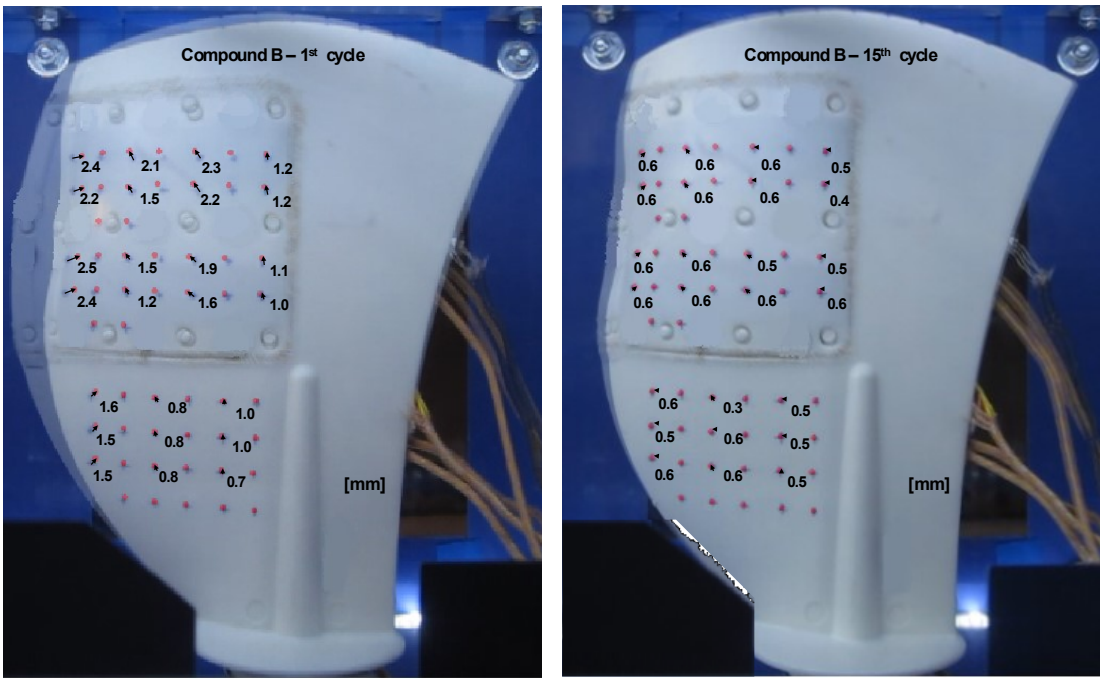

Figure 4.25 – Suction side superimposition between the initial shape and the maximum deflection for the 1st and the 15th activation cycle (ref. 4 of Preface)

With the same strategy adopted for the blade tip, superimposed black vectors join the same marker from the initial condition (black marker) to the activated condition (red marker). It is possible to observe that during the 1st activation cycle, the blade shape changes in the leading edge and trailing edge regions (Fig. 4.25). For the 1st cycle, significant deviation can be found in the trailing edge region

where the difference reached the value of 2,5 mm. Conversely, at the 15th cycle SMA strip activation can change only in the trailing edge region, and the deviation reaches only 0,6 mm. Unlike the view of the blade tip reported above (see Fig. 4.24), in the leading edge zone the deviation is not noticeable by using suction side image acquisition.

Thanks to the analyses reported above for both blade tip and suction side, it is possible to note that the blade shape changes according to the SMA strips and the actions of the polymeric structure. In particular, the blade shape is concave (moves towards the pressure side) both in the leading edge and trailing edge regions. This phenomenon, clearly depicted in Fig. 4.24, occurs with different intensity along the blade height. In fact, as reported in Fig. 4.25, the values of the deviation are different from the hub to the tip. In particular, the deviation is the lowest in the regions close to the root, while the deviation assumes the highest values in the SMA strip housing region.

From these results it is clear that, in order to recognize the actual blade shape during SMA strip activation, different methods have to be taken into account. The 2D image analysis techniques could represent suitable tools for measuring 2D deviation (and thus blade structure deformation) in a very accurate way. However, this method does not permit an overall evaluation of the blade shape. Because of the limitation of the 2D image analysis, 3D blade detection is proposed below.

The instantaneous 3D blade shape was acquired during the tests by using the Kinect sensor that allowed the digitalization of the blade shape. By using 3D detection, it is possible to (i) evaluate the blade shape changes during the activation tests and (ii) reconstruct the 3D blade shape by using a CAD modeler.

In the first step, the Kinect sensor through the SDK Software Development Kit toolkit was set depending on the measurement range, the required resolution, the specific levels of environmental light, and the surface appearance of the object. In this preliminary phase, the blade surface was prepared in order to avoid reflection by using a specific spray. The detection consists of blade shape digitalization by using the point cloud data provided by the SDK tool. The point cloud elaboration was performed by means of open source software (i.e. Blender, MeshLab) and the .stl file with the blade surface mesh was generated.

Point cloud data were then processed and converted into a polygonal representation of the scanned blade. The treatment of the point cloud is comprehensive of: (i) filtration in order to reduce the noise level, (ii) reduction of the mesh size through the elimination of the verbatim point, (iii) local modification of the mesh in order to fill the hole (if present) and make the surface as regular as possible and, finally, (iv) creation from the triangle mesh of the NURBS-based CAD model of the blade. In order to validate the ability of the Kinect sensor to acquire the 3D blade shape, a preliminary comparison between the blade reference CAD geometry and the acquired Kinect surface was conducted. In Fig. 4.26 the acquired surface of the blade at the initial condition (processed by open source software in order to obtain the polygonal representation) and the blade CAD geometry are superimposed. As shown, the Kinect sensor provided an accurate 3D blade shape since the two entities only differed at the boundary blade regions (especially at the blade tip), where the deviation was less than 1 mm. At the edges, the Kinect sensor also detects the blade thickness (as can be seen in Fig. 4.26) but this detection is less accurate and it is not taken into account during the blade reconstruction.

As stated above, the Kinect sensor was used to instantly detect the 3D blade shape during the activation test at the start of the thermal cycle and the end of the heating ramp at peak temperature. The detections reported in Fig. 4.27 refer to the 1st and 15th activation cycle. As can be seen, the maximum blade deflection located at the SMA strip housing zone (from 50 % to 87 % of the blade span, see Fig.

4.2 is clearly visible from the scanned surfaces. The deformations in the trailing edge area are highly noticeable even from the raw acquired surface.

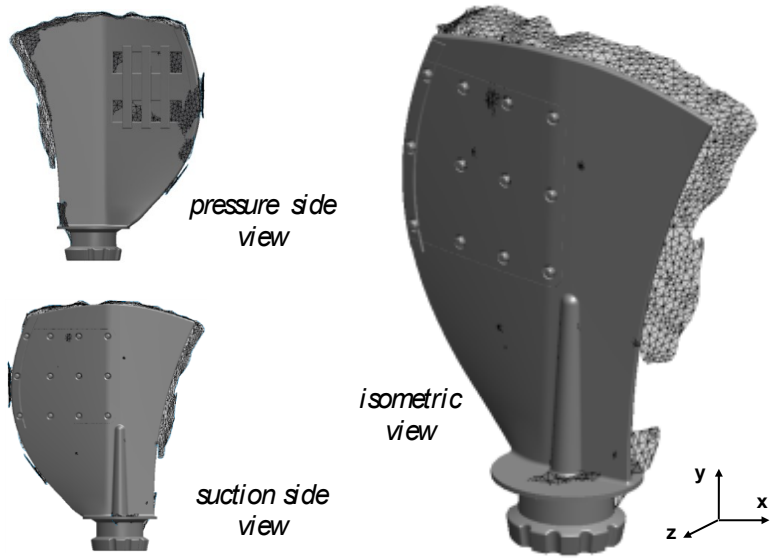

Figure 4.26 – Blade shape comparison: superimposition of the raw Kinect surface and CAD geometry for pressure side, suction side and isometric view (ref. 4 of Preface)

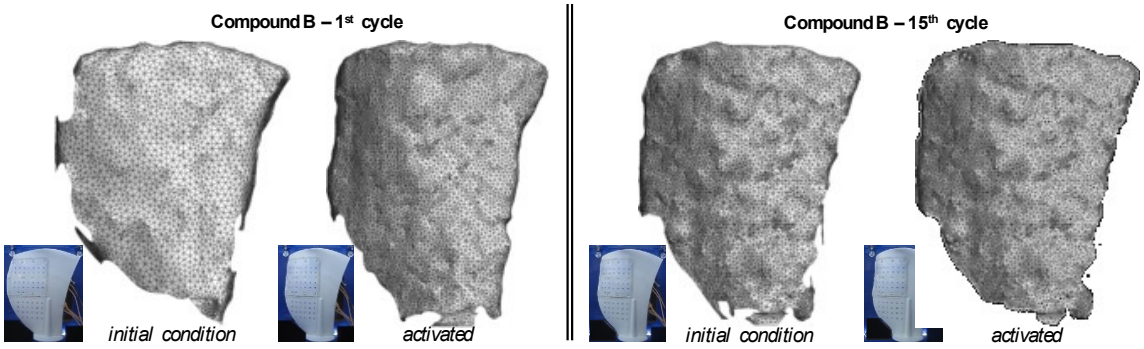

Figure 4.27 – Kinect surfaces for the 1st and 15th activation cycle in two conditions: initial and activated (ref. 4 of Preface)

Thanks to the 3D surface provided by the Kinect sensor during the activation tests, it was possible to analyse the different deformations that occurred in the blade shape along its span in a quantitative way. Figure 4.28 reports the scheme of the planes considered for the analysis: 20 %, 50 %, 70 % and 90% of the span for a blade height of 34,8 mm, 87,0 mm, 128,8 mm and 156,6 mm, respectively. Figure 4.29 shows the intersection between the suction side surface (Kinect surface) and the four different planes at increasing spans. They are depicted as circular and triangular single points for the initial condition and activated blade shape respectively, while the trend line improves the readability of the graph. The grey line refers to the initial condition while the black line is for the activated condition. Since the SMA strip housing zone is located above the midspan, the intersection at 20 % of the span showed no differences between the two suction side surfaces. By contrast, the other intersections showed remarkable deviations among the surfaces. In the leading edge area, the activated blade shows

the deviation with respect to the initial blade shape only in the 1st cycle. This deviation is about 13 mm, 15 mm and 20 mm for 50 %, 70 % and 90 %, respectively. During the 15th cycle, the deviation in the leading edge area is very limited and it is hidden by the surface approximation. Conversely, in the trailing edge area the activated blades show a greater amount of deviation in both of the cycles. The deviation between the activated blades is more evident for the 70 % and 90% intersections. As depicted in Fig. 4.29, blade shape changes (mean line deflection and trailing edge deformation) develop on each blade- to-blade plane (gray lines in Fig. 4.29) as a function of the blade span location.

It should be observed that progressive and continuous blade deformation, due to temperature-driven shape recovery, is directly related to the design of (i) the thermo-mechanical shape setting SMA strips, (ii) the position of the SMA strip housing zone and (iii) the polymeric matrix stiffness.

Thanks to these accurate Kinect surfaces the corresponding 3D blade shapes can be achieved. The 3D analysis carried out by a non-contact device allows blade shape analysis in all of the blade sections. The 3D blade detection is less accurate (point clouds data generated by the Kinect sensor were affected by blade surface finishing and the reflection and diffraction of the PMMA panels) than the 2D image captured by a digital camera, but is highly suitable for detecting the instantaneous overall 3D blade shape without disturbing the airflow.

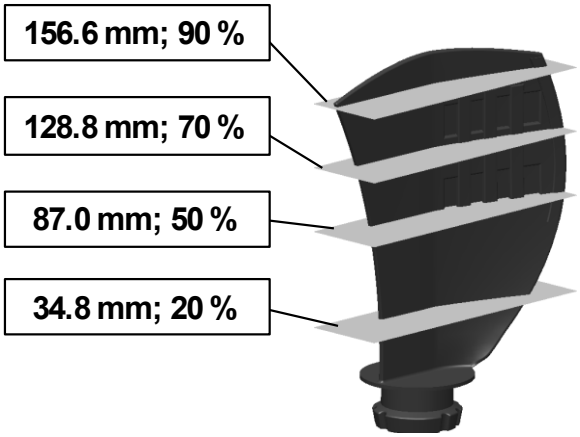

Figure 4.28 – Scheme of the planes considered for the analysis

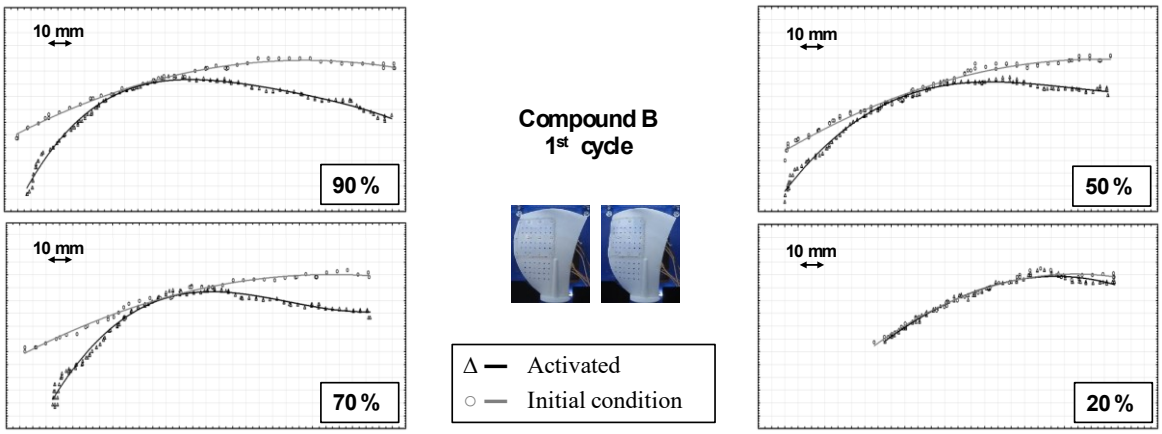

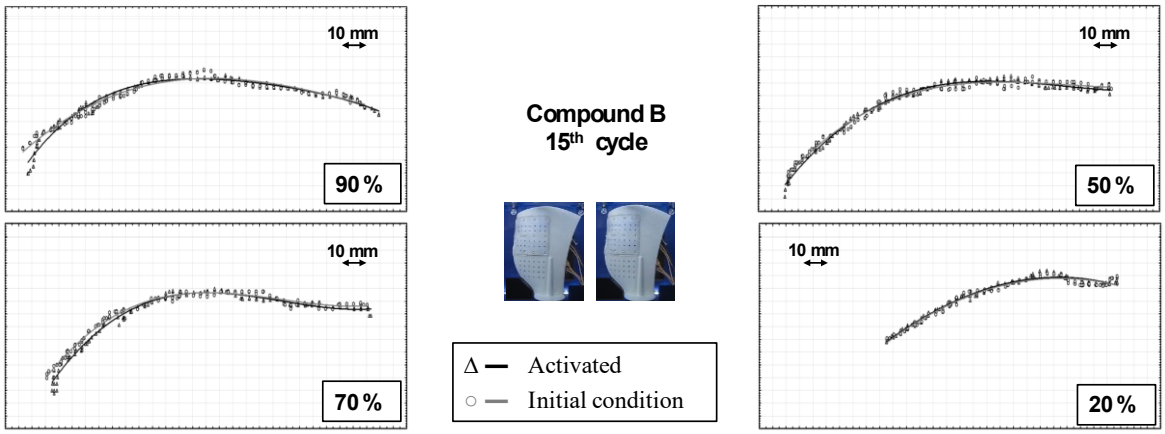

Figure 4.29 – Graphs of the suction side deviations at 20 %, 50 %, 70 % and 90 % of the blade span for the 1st and 15th activation cycle at the initial and activated condition

4.3 Time-lag comparison

In a traditional cooling system, the energy optimization could be achieved by controlling the engine temperature and reducing the cooling fan run time by using a fan clutch. The operation of the fan is controlled by means of some sensors placed in the cooling circuit for measuring the air temperature and thus tuning the rotational fan velocity. Nevertheless, the increasingly utilisation of a great number of sensor devices and the resulting raised complexity make, in some cases, the control system too bulky, expensive and not sufficiently robust for the intended application. During the actual fan cooling operation, the air temperature changes according to the engine load and/or the effect of the ram air and, at the same time, the fan rotational velocity could be changed due to the engine operation load requirement.

Conversely, by using a SMA-base morphing blade the performance modification during operation is completely obtained by the blade shape modification provided by the SMA elements without sensors and control systems.

To study the possibility of employing SMA strips as actuator elements, a comparison with common viscous clutches behaviour is proposed. In Fig. 4.30, the timewise evolution of air temperature, aerofoil camber at the blade tip and rotational fan velocity are depicted. To highlight the differences between the two actuating solutions, the comparison between the timewise camber variation and the timewise rotational velocity variation is performed with the same timewise temperature variation. The thermal variation trend starts from 0 s and ends at 440 s, and it is inline with the heating ramp reported above and similar to a common engine coolant temperature variation during the warm-up condition.

The comparison is related to (i) the evaluation of the time-lag that represents the actuator awaiting time after the thermal input (green lines in Fig. 4.30) and (ii) the evaluation of the time range transient actuator response (time ranges between green lines and red lines in Fig. 4.30. The considered viscous clutch is an on/off viscous fan clutch but similar results can be obtained to considering a modulated viscous fan clutch. As reported by Everett (1974), modulated viscous clutch allows the reduction of the power consumption but the time range transient actuators response is even so very limited (with a thermal input range of 60–71 °C the fan speeds moves from 1000 rpm to 2000 rpm).

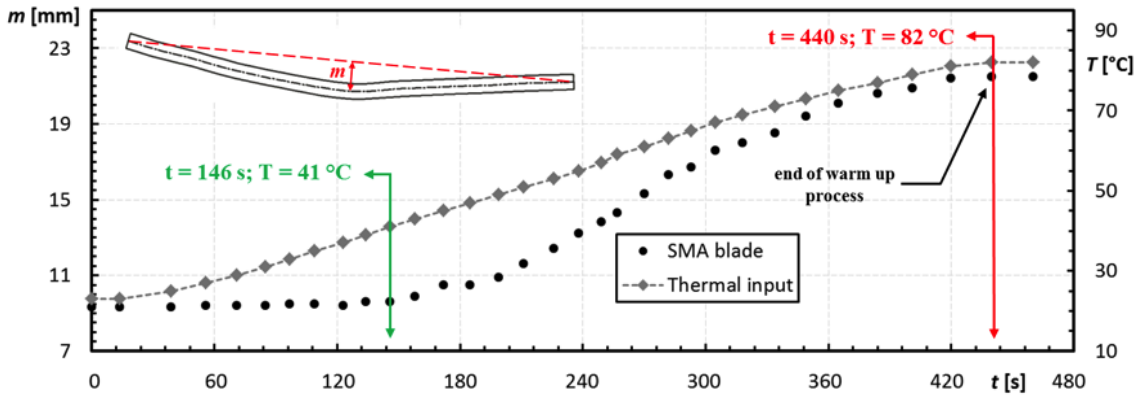

(a)

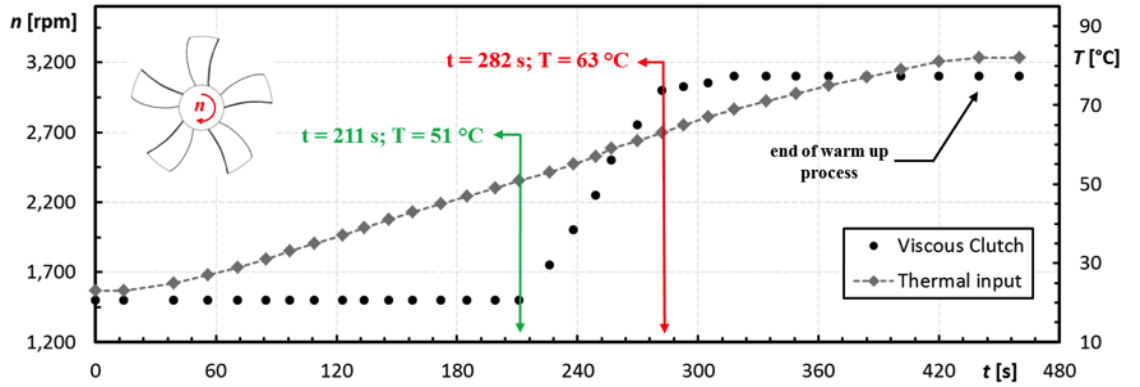

(b)

Figure 4.30 – (a) Timewise evolution of air temperature, aerofoil camber at the blade tip for the SMA-based morphing blade and (b) timewise evolution of air temperature and rotational fan velocity for viscous clutch (ref. 6 of Preface)

As can be seen from Fig. 4.30, the SMA time-lag is shorter than the viscous clutch, 146 s and 211 s, respectively. Then the SMA actuator requires a lower temperature to start the reaction that occurs 10 °C earlier than the viscous clutch. Regarding the time range transient actuator response, it is evident that the viscous clutch solution provided a fast change of the fan rotational velocity, as can be seen from the steep ramp in Fig. 4.30. This step change velocity variation does not follow the thermal input and the fan rotational velocity reaches the target velocity independently from the thermal input variation after 12 s. The fan rotational velocity reaches a value lower than the rotational velocity of the driver shaft. In this specific case, the rotational velocity of the driver shaft is equal to 3300 rpm compared to the target rotational velocity equal to 3000 rpm.

Conversely, the smooth change camber variation follows the thermal input thanks to thermal controlled SMA strips actuation. The transient SMA actuator response ends at 440 s which corresponds to the thermal input end. This experimental result confirms the capability of SMA materials to cover the lower power actuators in the automotive field. The time range actuator response indicates that the SMA strips provide a lower frequency control that fits well with engine thermal requirement. The SMA strips blade actuator could improve the match between the fan performance and engine cooling thermal request and thus enhance the engine thermal management.

Concluding remarks

The present work reports the results of an experimental approach focused on the application of SMA strips, based on commercially available NiTi alloys, as active elements in polymeric matrices. The study was intended for the development of a morphing blade potentially suitable automotive cooling axial fans, whose actuation, resulting from the SMA thermal activation, enables to optimise the cooling fan performance.

According to the main outcomes, the following conclusions can be drawn.

- The thermal characterisation of the SMA material, performed by means of different thermomechanical treatments, permits the assessment of the best shape setting treatment parameters for the intended application. The proper bent shape, obtained by a double thermomechanical treatment, performed at 450 °C for 25 min, enables a percentage of shape recovery at around 55 %.

- Thermal activation cycles, obtained by the experimental test bench realised on purpose for fluid flow activations, show the feasibility of this technique for the actuation of SMA strip, overcoming the issues related to the common electrical heating systems. The results, concerning the single strip composite structure, show a continuous and progressive deflection of the composite structure according to the thermal input, highlighting the opportunity to take advantage of thermally activated phase transformations as an effective control system.

- The proposed novel concept of morphing blade, made up of a polymeric matrix equipped with NiTi shape memory alloy strips as active elements, was experimentally tested by using a purpose-built wind tunnel, which reproduced actual thermal ramps of the heat exchanger. This setup enables the thermal actuation of the blade by the air stream flow demonstrating that favourable aerodynamic blade shape changes could be achieved by the SMA solid phase transformations. This challenging solution prevents the introduction of flow-disturbing elements and enables the development of an axial fan equipped with blades whose shape changes continuously as a function of the airflow temperature.

- Two-dimensional and three-dimensional technique analyses allow the instantaneous evaluation of the blade shape modification during the activation tests. The study of the morphing ability of the blade as a function of the polymeric compound show the influence

of the glass-fibre amount on the blade stiffness; in particular, the glass fibre reinforced Nylon PA66 containing 15 % of glass reinforcement and 5 % of elastomer coupled with the thermally treated SMA strips, shows the best compromise between the value of deflection at peak temperature and recovery capability.

- The comparison between the proposed SMA driven passive control system and common visco clutch actuation for blade geometry changes, proves the advantages of the SMA based solution in terms of (i) shorter actuator awaiting time after the thermal input resulting from the lower temperature to start the activation (10 °C earlier than the visco clutch), (ii) smooth change camber variation which enables a shorter time range transient actuator response and (iii) improved match between the fan performance and the engine cooling thermal request.

References

Baniasadi E., Aydin M., Dincer I., Naterer G. F. "Computational Aerodynamic Study of Automotive Cooling Fan in Blocked Conditions", *Engineering Applications of Computational Fluid Mechanics*, **7**(1), 66–73, (2013)

Barbarino S., Bilgen O., Ajaj R. M., Friswell M. I., Inman D. J. "A review of morphing aircraft", *Journal of Intelligent Material Systems and Structures*, **22**, 823–877, (2011)

Barbarino S., Pecora R., Lecce L., Concilio A., Ameduri S., Calvi E. "A novel SMA-based concept for airfoil structural morphing", *Journal of materials engineering and performance*, **18**(5-6), 696–705, (2009)

Baz A., Chen T., Ro J. "Shape control of NITINOL-reinforced composite beams", *Composite Part B*, **31**, 631–642, (2000)

Birman V. "Review of mechanics of shape memory alloy structures", *Applied Mechanics Reviews*, **50**(11), 629–645, (1997)

Blair E. C. "Comparison of Modulated (Viscous) Versus On-Off Fan Clutches", SAE Technical Paper No. 740596, (1974)

Buehler W. J., Gilfrich J. V., Wiley R.C. "Effect of low-temperature phase changes on the mechanical properties of alloys near composition TiNi", *Applied Physics*, **34**, 1475–1477, (1963)

Butera F. "Shape memory actuators", *Advanced Materials & Processes*, **3**, 37–40, (2008)

Butera F., Coda A., Vergani G. "Shape memory actuators for automotive applications", Proceedings of NanoMetrology workshop, Torino (Italy), 12–16, (2007)

Carbone V., Carocci M., Savio E., Sansoni G., De Chiffre L. "Combination of a vision system and a coordinate measuring machine for the reverse engineering of free-form surfaces", *International Journal of Advanced Manufacturing Technology*, **17**, 263–271, (2001)

Chalgren R. D. "Thermal Comfort and Engine Warm-Up Optimization of a Low-Flow Advanced Thermal Management System," SAE Technical Paper No. 2004-01-0047, (2004)

Chen L. C., Lin G. C. I. “An integrated reverse engineering approach to reconstructing free-form surfaces”, *Computer Integrated Manufacturing Systems*, **10**, 49–60, (1997)

Cismasiu C. *Shape Memory Alloys*. Sciyo, Rijeka, Croatia, (2010)

Elmer A., Parry S., Blandford G. “Direct Sensing-Modulating Fan Clutch for Heavy Duty Commercial Vehicles,” SAE Technical Paper No. 942254, (1994)

Everett G. B. “Comparison of Modulated (Viscous) Versus On-Off Fan Clutches,” SAE Technical Paper No. 740596, (1974)

Firstov G. S., Van Humbeeck J., Koval Y.N. “High temperature shape memory alloys problems and prospects”, *Journal of Intelligent Material Systems and Structures*, **17**, 1041–1047, (2006)

Giurgiutiu V., Rogers C. A., Zuidervaart J. “Design and preliminary tests of an sma active composite tab”, Proceedings of Spie, Smart Structures and Materials 1997: Smart Structures and Integrated Systems, 346, (1997)

Gonzalez-Jorge H., Riveiro B., Vazquez-Fernandez E., Martínez-Sánchez J., Arias P. “Metrological evaluation of Microsoft Kinect and Asus Xtion sensors”, *Measurement*, **46**, 1800–1806, (2013)

Hallqvist T. “The Cooling Airflow of Heavy Trucks-A Parametric Study”, SAE Technical Paper No. 2008-01-1171, (2008)

Hartl D. J., Lagoudas D. C. “Aerospace applications of shape memory alloys”, Proceedings of the Institution of Mechanical Engineers, *Part G: Journal of Aerospace Engineering*, **221**(4), 535–552, (2007)

Hartl D. J., Mooney J. T., Lagoudas D. C., Clakins F. T., Mabe J. H. “Use of a Ni60Ti shape memory alloy for active jet engine chevron application: I. Thermomechanical characterization”, *Smart Materials and Structures*, **19**, 015020 (14pp), (2010a)

Hartl D. J., Mooney J. T., Lagoudas D. C., Clakins F. T., Mabe J. H. “Use of a Ni60Ti shape memory alloy for active jet engine chevron application: II. Experimentally validated numerical analysis”, *Smart Materials and Structures*, **19**, 015021 (18pp), (2010b)

Hirose S., Ikuta K., Umetani Y. “Development of shape-memory alloy actuators. Performance assessment and introduction of a new composing approach”, *Advanced Robotics*, **3**(1), 3–16, (1989)

Hodgson D. E., Wu M. H., Biermann R. J. “Shape memory alloys”, In: *Properties and Selection: Nonferrous Alloys and Special-Purpose Materials*, ASM Handbook vol. 2, ASM International, 897–902, (1990)

Huang S., Leary M., Ataalla T., Probst K., Subic A. “Optimisation of Ni–Ti shape memory alloy response time by transient heat transfer analysis”, *Materials and Design*, **35**, 655–663, (2012)

Huang W. “On the selection of shape memory alloys for actuators”, *Materials & Design*, **23**, 11–19, (2002)

Hutapea P., Kim J., Guion A., Hanna C., Heulitt N. “Development of a smart wing”, *Aircraft Engineering and Aerospace Technology: An International Journal*, **80**(4), 439–444, (2008)

Icardi U. “Large bending actuator made with SMA contractile wires: theory, numerical simulation and experiments”, *Composite Part B*, **32**, 259–267, (2001)

Jani J. M., Leary M., Subic A., Gibson M. A. “A review of shape memory alloy research, applications and opportunities”, *Materials and Design*, **56**, 1078–1113, (2014)

Janocha H. *Adaptronics and smart structures - Basics, Materials, Design and Applications.* Springer-Verlag, New York, USA, (2007)

Khoshelham K., Elberink S.O. “Accuracy and resolution of Kinect depth data for indoor mapping applications”, *Sensor*, **12**, 1437–1454, (2012)

Kim K. B., Choi K. W., Lee K. H., Lee, K. S. “Active Coolant Control Strategies in Automotive Engines”, *International Journal of Automotive Technology*, **11**(6), 767–772, (2010)

Kohl M. *Shape Memory Microactuators.* Springer-Verlag, Berlin, German, (2004)

Kuder I.K., Arrieta A. F., Raither W. E., Ermanni P. “Variable stiffness material and structural concepts for morphing applications”, *Progress in aerospace sciences*, **63**, 33–55, (2013)

Kudva J N. “Overview of the DARPA Smart Wing Project”, *Journal of Intelligent Material Systems and Structures*, **15**(4), 4261–267, (2004)

Lagoudas D. C. *Shape memory alloys: modeling and engineering applications*. Springer-Verlag, New York, USA, (2008)

Lahoz R., Gracia-Villa L., Puértolas, J. A. “Training of the two-way shape memory effect by bending in NiTi alloys”, *Journal of Engineering Materials and Technology*, **124**, 397–401, (2002)

Lee K., Lee J., Koo B. “Development of a Continuously Variable Speed Viscous Fan Clutch for Engine Cooling System”, SAE Technical Paper No. 980838, (1998)

Lehner C., Parker G., Arici O., Johnson J. “Design and Development of a Model Based Feedback Controlled Cooling System for Heavy Duty Diesel Truck Applications Using a Vehicle Engine Cooling System Simulation”, SAE Technical Paper No. 2001-01-0336, (2006)

Lin W., Sunden B. “Vehicle Cooling Systems for Reducing Fuel, Consumption and Carbon Dioxide: Literature Survey”, SAE Technical Paper No. 2010-01-1509, (2010)

Liu Y., Liu Y., Van Humbeeck J. “Two-way shape memory effect developed by martensite deformation in NiTi”, *Acta Materialia*, **47**, 199–209, (1999)

Liu Y., McCormick P. G. “Factor influencing the development of two-way shape memory in NiTi”, *Acta Metallurgica et Materialia*, **38**, 1321–1326, (1990)

Luo H. Y., Abel E. W. “A comparison of methods for the training of NiTi two-way shape memory alloy”, *Smart Materials and Structures*, **16**, 2543–2549, (2007)

Mabe J. H., Calkins F., Butler G. “Boeing’s variable geometry chevron, morphing aerostructure for jet noise reduction”, In: 47th AIAA/ ASME / ASCE / AHS / ASC Structures, Structural Dynamics and Materials Conference, Newport, Rhode Island, 1–19, (2006)

McWilliams A. “Smart materials and their applications: technologies and global markets”, BCC Research Advanced Materials Report, 161, (2011)

Melton K. R. “General applications of shape memory alloys and smart materials”, In: Otsuka K., Wayman C. M. (Eds.), *Shape memory materials*, Chapter 10, 220–239, Cambridge, Cambridge University Press, (1999)

Microsoft Corporation, (2014), Technical Information

Nessim W., Zhang F., Changlu Z., Zhenxia Z. “A Simulation Study of an Advanced Thermal Management System for Heavy Duty Diesel Engines”, Proceedings of 2012 International Conference on Mechanical Engineering and Material Science (MEMS 2012), Yangzhou, China, December 28-30, 287–290, (2012)

Oehler S. D., Hartl D. J., Lopez R., Malak R. J., Lagoudas D. C. “Design optimization and uncertainty analysis of SMA morphing structures”, *Smart Materials and Structures*, **21**(9), 1–16, (2012)

Ölander A. “An electrochemical investigation of solid cadmium-gold alloys”, *American Chemical Society*, **54**, 3819–3833, (1932)

Otsuka K., Wayman M. C. *Shape Memory Materials*. Cambridge University Press, Cambridge, (1998)

Pecora R., Dimino I. “SMA for aeronautics”, In: Lecce L., Concilio A. (Eds.), *Shape Memory Alloy Engineering*, Chapter 10, 275–304, Butterworth-Heinmann, Oxford, UK, (2015)

Perkins J., Hodgson D. “The two way shape memory effect”, In: Duerig T. W., Melton K. N., Stöckel D. (Eds.), *Engineering aspect of shape memory alloys*, Butterworth-Heinmann, Oxford, UK, 195–206, (1990)

Perkins J., Sponholz R. O. "Stress-induced martensite transformation cycling and two-way shape memory training in Cu-Zn-Al alloys", *Metallurgical and Materials Transactions A*, **15A**, 313–321, (1984)
Ponta F. L., Otero A. D., Rajana A., Lagoa L. I. "The adaptive-blade concept in wind-power applications", *Energy for Sustainable Development*, **22**, 3–12, (2014)

Rao A., Srinivasa A. R., Reddy J. N. *Design of Shape Memory Alloy (SMA) Actuators*. Springer-Verlag, New York, USA, (2015)

Rizzoni R., Merlin M., Casari D. "Shape recovery behaviour of NiTi strips in bending: experiments and modelling", *Continuum Mechanics and Termodynamics*, **25**, 207–227, (2013)

Roh J. H., Kim K. S., Lee I. "Shape adaptive airfoil actuated by a shape memory alloy and its aerodynamic characteristics", *Mechanics of advanced materials and structures*, **16**, 260–274 (2009)

Roytburd A. L., Slutsker J., Wuttig M. "Smart Composites with Shape Memory Alloys", *Comprehensive Composite Materials*, **5**, 507–522, (2000)

Saint-Sulpice L., Arbab Chirani S., Calloch S. "A 3D super-elastic model for shape memory alloys taking into account progressive strain under cyclic loadings", *Mechanics of materials*, **41**, 12–26, (2009)

Sanders B., Crowe R., Garcia E. "Defense advanced research projects agency: Smart materials and structures demonstration program overview", *Journal of Intelligent Material Systems and Structures*, **15**(4), 227–233, (2004)

Sansoni G., Docchio F. "In-field performance of an optical digitizer for the reverse engineering of free-form surfaces", *International Journal of Advanced Manufacturing Technology*, **11/12**, 1353–1361, (2005)

Schetky L. M., Steinetz B. M. "Shape memory alloy adaptive control of gas turbine engine compressor blade tip clearance", Proceedings of Spie, Smart Structures and Materials 1998: Industrial and Commercial Applications of Smart Structures Technologies, 346, (1998)

Schick J. R., Darren J. H., Lagoudas D. C. "Incorporation of Shape Memory Alloy Actuators into Morphing Aerostructures", In: Valasek J. (Ed.), *Morphing Aerospace Vehicles and Structures*, Chapter 10, Wiley, New Jersey, (2012)

Schwenke H., Neuschaefer-Rube U., Pfeifer T., Kunzmann H. "Optical methods for dimensional metrology in production engineering", CIRP Annals-Manufacturing Technology, **51**(2), 685–699, (2002)

Sofla A. Y. N., Meguid S. A., Tan K. T., Yeo W. K. "Shape morphing of aircraft wing: Status and challenges", *Materials and Design*, **31**, 1284–1292, (2010)

Song G., Kelly B., Agrawal B. N. "Active position control of a shape memory alloy wire actuated composite beam", *Smart Materials and Structure,* **9**, 711–716, (2000)

Sreekumar M., Nagarajan T., Singaperumal M. "Application of trained NiTi SMA actuators in a spatial compliant mechanism: experimental investigations", *Materials & Design*, **30**, 3020–3029, (2009)

Stanewsky E. "Adaptive wing and flow control technology", *Progress in Aerospace Sciences,* **37**, 583–667, (2001)

Stanewsky E. "Aerodynamic benefits of adaptive wing technology", *Aerospace Science and Technology*, **4**(7), 439–452, (2000)

Stoeckel D., "Shape Memory Actuators for Automotive Applications", *Materials & Design*, **11**(6), 302–307, (1990)

Strelec J. K., Lagoudas D. C., Khan M. A., Yen J. "Design and implementation of a shape memory alloy actuated reconfigurable airfoil", *Journal of Intelligent Material Systems and Structures*, **14**, 257–273, (2003)

Sun L., Huang W. M., Ding Z., Zhao Y., Wang C. C, Purnawali H., Tang C. "Stimulus-responsive shape memory materials: A review", *Materials & Design*, **33**, 577–640, (2012)

Tsoi K. A., Schrooten J., Stalmans R., "Thermomechanical characteristics of shape memory alloys, Part I", *Materials Science and Engineering: A*, **368**, 286–298, (2004)

Wei Z. G., Sandstrom R., Miyazaki S. "Shape memory materials and hybrid composites for smart systems: Part II Shape-memory hybrid composites", *Journal of Materials Science*, **33**, 3763–3783, (1998)

Weisshaar T. A. "Morphing aircraft systems: historical perspectives and future challenges", *Journal of Aircraft*, **50**(2), 337–353, (2013)

Yue H., Chen W., Wu X., Liu J. "Fast 3D modeling in complex environments using a single Kinect sensor", *Optics and Lasers in Engineering*, **53**, 104–111, (2014)

Zhou G., Lloyd P. "Design, manufacture and evaluation of bending behavior of composite beams embedded with SMA wires", *Composite Science and Technology*, **69**(13), 2034–2041, (2009)

Acknowledgments

First of all, I would like to express my sincere gratitude to my supervisor Ing. Mattia Merlin who allowed me to do this three years' path. His continuous guidance, listening and support have been of invaluable importance for the present work but nonetheless for my growth, both personal and professional. Thanks for give me the freedom to explore and discover on my own without however fail to support me whenever I have needed. Moments of debate and exchange of experiences, advices, ideas and suggestions have enormously enriched me.

Beside my supervisor, I am also thankful to Professor Gian Luca Garagnani for giving me the opportunity of doing this experience. My gratitude is for guidance, assistance, caring and for providing me with a pleasant atmosphere for doing research.

I express my gratitude to Professor Raffaella Rizzoni for her help in the development of the numerical model and for always giving me stimulating, useful and interesting ideas for the improvement of the research activity.

A special thank goes to the person who has strongly believed in the possibility of creating a morphing blade with SMA strips but he has not had time to carry out his idea. Thank you Ing. Guido Rosati for giving me a chance to get here. What little I have known you, I have learned how important is to believe in what you do to get beyond the difficulties. I also gratefully acknowledge Fratelli Rosati Company of Leinì (Torino), respectively Rag. Pierfrancesco Rosati and Mr. Abbenante Salvatore and all the technical staff, for the financial and technical support of the research.

I would also like to thank all members of the Metallurgy and Corrosion Group of the University of Ferrara, for the technical support, assistance and guidance during these years.

I am also grateful to all my colleagues in the Engineering Department, former and current ones, who have contributed to create pleasant moments for dialogue and reciprocation. Thank are also due to the technical staff for the support and collaboration.

I would like to thank Chiara Soffritti, Vincenzo Gabrielli and Daniele Casari for have always willing to listen, help and give useful suggestions. A heartfelt thanks goes to my colleague of this PhD path Elettra Fabbri for her patience, support and care in particular during these last months of hard work. I could not forget all the happy and funny moments spent all together. Without your constant presence over the years this experience would not have been so special.

A great thank you goes to all the members of the Fluid Machinery Research Group led by Professor Michele Pinelli for their important contribution to the research. A special thank goes to Alessio Suman for all the technical support kindly provided to the activity.

Thanks are also due to my friends, near and far, for all the pleasant and funny moments which helped me to overcome difficulties. Thanks to those who have shown me their affection and support with a message, a call or a dinner together.

Most importantly, none of this would have been possible without the love, patience and support of my family during all these years. This few words to express to my parents, my brother and my aunt a heart-felt gratitude for care, affection, understanding and for having always supported and encouraged me with a constant presence.

A special thanks goes to the person who have always offered me his unconditional support, love, care, patience and time, to understand, listen and help me in every situation. These years have required to me hard work and dedication but it would not be enough without your tacit and active support, your love and your patience. Thank you for have chosen to be always at my side.